



Carl von Ossietzky Universität Oldenburg

Fakultät II – Informatik, Wirtschafts- und Rechtswissenschaften  
Department für Informatik

---

**Multimodal Sensing and Imaging Technology by  
Integrated Scanning Electron, Force, and Near-  
field Microwave Microscopy and its Application  
to Submicrometer Studies**

---

**DISSERTATION**

zur Erlangung des Grades eines

**Doktors der Ingenieurwissenschaften (Dr.-Ing.)**

vorgelegt von

**Olaf C. Hänßler**

geboren am 19. September 1967 in Hannover

22. Februar 2018



THÈSE DE DOCTORAT DE L'UNIVERSITÉ DE LILLE  
École Doctorale Sciences Pour l'Ingénieur (ED SPI)

Pour obtenir le grade de

DOCTEUR

Spécialité: Electronique, microélectronique, nanoélectronique et micro-ondes

Par

Olaf C. HAENSSLER

---

**Multimodal Sensing and Imaging Technology by  
Integrated Scanning Electron, Force, and Near-  
field Microwave Microscopy and its Application  
to Submicrometer Studies**

---

Soutenue le 22 fevrier 2018 devant la commission d'examen

Membres du jury:

Dr. habil. D. THÉRON	Directeur de thèse (IEMN CNRS UMR 8520, Villeneuve d'Ascq, F)
Prof. Dr. habil. S. FATIKOW	Co-directeur de thèse (Université de Oldenburg, D)
Dr. habil. F. MARCHI	Rapporteur (Joseph Fourier Université/NÉEL CNRS, Grenoble, F)
Prof. Dr. S. PEIK	Rapporteur (City University of Appl. Sciences Bremen, D)
Prof. Dr. W. NEBEL	Invités (Université de Oldenburg, D)
Dr. A. MIKSCHL	Invités (Université de Oldenburg, D)
Dr. habil. K. HADDADI	Invités (IEMN CNRS UMR 8520, Villeneuve d'Ascq, F)



# ABSTRACT

The disciplines of micro- and nanotechnology, materials science, life sciences and in particular the research of semiconductors requires combinatorial tools for the investigation, manipulation and transport of materials and objects in the submicrometer range. The coupling of multiple sensing and imaging techniques allows for obtaining complementary and often unique datasets of samples under test. By means of an integrated microscopy technique with different modalities, it is possible to gain multiple information about nanoscale samples by recording at the same time. The expansion with nanorobotics and an open-source software framework specifically engineered for the requirements in nanotechnology, leads to a technology approach for semiconductor research and material science.

This work contributes to this area of research and shows the potential of such a multimodal technology approach by focusing on a demonstrator setup. It operates under high-vacuum conditions inside the chamber of a Scanning Electron Microscope (SEM) and serves as a technology platform by fusing various microscopy modalities, techniques and processes. An Atomic Force Microscope (AFM) based on a compact, optical interferometer performs imaging of surface topography, and a Scanning Microwave Microscope (SMM) records electromagnetic properties in the microwave frequency domain, both operating inside an SEM. An open-source software framework, tailored for vision-based automation by nanorobotics, controls the instrument. The setup allows for observing the region-of-interest with SEM spatial resolution, while imaging and characterizing with interacting evanescent microwaves and intermolecular forces simultaneously.

In addition, a multimodal test standard is introduced which was designed for this technology and subsequently confirms the functionality of the demonstrator. Within this context, the work also includes an electrical analysis of micro-scale Metal Oxide Semiconductor (MOS) capacitors, including an approximation for use in the calibration of microwave microscopes.

# ZUSAMMENFASSUNG

Die Disziplinen der Mikro- und Nanotechnologie, der Materialwissenschaften, der Biowissenschaften und insbesondere der Halbleiterforschung erfordern kombinatorische Werkzeuge zur Untersuchung, Manipulation und zum Transport von Materialien und Objekten im Submikrometerbereich. Die Kombination aus mehreren Meß- und Bildgebungsverfahren ermöglicht es, komplementäre und oft einzigartige Datensätze von zu testenden Proben zu erhalten. Durch eine hybride Mikroskopietechnik, auf der Grundlage unterschiedlicher Modalitäten, ist es möglich, durch parallel gewonnene Aufzeichnung vielschichtige Informationen über nanoskalige Proben zu gewinnen. Die Erweiterung mit Nanorobotik und einem Open-source Software Framework, speziell ausgerichtet an die Anforderungen der Nanotechnologie, führt zu einem Technologieansatz für die Halbleiterforschung und Materialwissenschaft.

Diese Arbeit leistet zu dem oben genannten Forschungsgebiet seinen Beitrag und zeigt das Potential einer solch multimodalen Technologie, indem ein Demonstratoraufbau und dessen Validierung detailliert beschrieben wird. Dieser arbeitet unter Hochvakuumbedingungen in der Kammer eines Rasterelektronenmikroskops (REM) und dient als Technologie-Plattform indem sich verschiedene mikroskopische Modalitäten, Techniken und Prozesse verschmelzen. Ein Rasterkraftmikroskop (AFM), basierend auf einem kompakten, optischen Interferometer, ermöglicht die Abbildung der Oberflächentopographie und ein Rastermikrowellenmikroskop zeichnet elektromagnetische Eigenschaften im Mikrowellenfrequenzbereich auf, beide in einem REM operierend. Ein Open-Source Software-Framework, optimiert für bildbasierte Nanorobotik, steuert das Gerät. Dieser Technologiedemonstrator erlaubt es, die sogenannte „Region of Interest“ mit elektronenmikroskopisch und somit mit der Ortsauflösung eines REM live zu beobachten, während gleichzeitig eine Charakterisierung der Probenoberfläche mit wechselwirkenden evaneszenten Nahfeld-Mikrowellen und intermolekularen Kräften erfolgt.

Des weiteren kommt es zur Vorstellung eines multimodalen Teststandards, der für diese Technologie entwickelt wurde und bestätigt nachfolgend die Funktionsweise des Demonstrators. Innerhalb dieses Kontextes umfaßt die Arbeit auch eine elektrische Analyse von mikroskaligen Metall-Oxid-Halbleiter (MOS)-Kondensatoren, einschließlich einer Approximation für den Gebrauch in der Kalibration von Mikrowellenmikroskopen.

# RÉSUMÉ

L'étude, la manipulation et le transport d'objets et de matériaux de tailles de l'ordre du micromètre ou nanomètre sont indispensables dans les domaines des micro et nanotechnologies, des sciences des matériaux ou du vivant et particulièrement dans la recherche sur les semi-conducteurs. La combinaison de plusieurs procédés d'imagerie et de mesure permet d'obtenir des ensembles de données complémentaires et parfois uniques. A l'aide d'une technique hybride de microscopie présentant des modalités de mesure différentes et des enregistrements synchrones, on peut recueillir des informations complémentaires sur des échantillons à l'échelle nanométrique. De plus, l'intégration de procédés nanorobotiques et un framework logiciel open-source, spécifiquement adapté aux exigences des nanotechnologies, permet une approche technologique pour la recherche sur les semi-conducteurs et les sciences des matériaux.

Ce travail démontre le potentiel d'une telle technologie multimodale en se focalisant sur un instrument démonstrateur et sur sa validation. Ce démonstrateur fonctionne sous vide poussé dans la chambre d'un microscope électronique à balayage (MEB) et sert de plateforme technologique dans laquelle sont intégrés différentes modalités, technologies et procédés. Un microscope à force atomique (MFA) basé sur un interféromètre optique compact permet l'imagerie de la topographie de surface tandis qu'un microscope à micro-ondes à balayage (MMB) enregistre les caractéristiques électromagnétiques dans la gamme de fréquence des micro-ondes, le tout opérant dans le même MEB.

L'engin est contrôlé par un ensemble de logiciels « open source » qui est optimisé pour la nanorobotique basée sur l'imagerie. Ce démonstrateur technologique permet d'observer en direct la région d'intérêt à l'aide du microscope électronique et par conséquent avec une résolution latérale propre au MEB tandis qu'est effectuée en champ proche la caractérisation de la surface de l'échantillon par intermédiaire des micro-ondes évanescentes et des forces intermoléculaires.

Ensuite, est présenté un standard multimodal de test qui a été conçu pour cette technologie et qui valide la fonctionnalité de l'instrument démonstrateur. Le présent travail est complété par une analyse électrique de capacités métal oxyde semi-conducteur (MOS) ainsi que leur approximation destinée au calibrage de microscopes à micro-ondes.

This page left intentionally blank.

# CONTENTS

<b>1</b>	<b>Introduction</b> .....	1
1.1	Objectives .....	8
1.2	Outline / Author's Contribution .....	10
<b>2</b>	<b>Integrated AFM-in-SEM and SMM</b> .....	13
2.1	Probe-Sample Interface.....	16
2.2	Combined Scanning Force and Electron Microscopy .....	24
2.2.1	Design of a Laser Interferometer-based AFM-in-SEM .....	25
2.2.2	Validation of a Laser Interferometer-based AFM-in-SEM .....	30
2.3	Scanning Microwave Microscopy .....	33
2.3.1	Areas of SMM Applications .....	37
2.3.2	Near-field probes .....	39
2.4	Summary .....	51
<b>3</b>	<b>High-frequency Impedances at the Nanoscale</b> .....	53
3.1	Fundamentals .....	53
3.2	Interferometry in Microwave Microscopy.....	58
3.3	High-Impedance Microwave Interferometer .....	62
3.4	Summary .....	67
<b>4</b>	<b>Multimodal Scanning Electron, Force, and Near-field Microwave Microscopy</b> .....	69
4.1	System Architecture .....	73
4.2	System Control.....	77

4.3	System Test .....	82
4.4	Multimodal Calibration and Test .....	85
4.4.1	Multimodal Test Standard .....	89
4.4.2	Robotic Calibration Procedure.....	95
4.5	System Validation .....	98
4.5.1	Multimodal Test Standard.....	98
4.5.2	Memristor.....	104
4.5.3	Non-raster Trajectory Scanning .....	107
4.6	Summary .....	109
<b>5</b>	<b>Conclusion and Future Directions.....</b>	<b>111</b>
<b>6</b>	<b>Publication bibliography .....</b>	<b>115</b>
	<b>Acronyms and Abbreviations.....</b>	<b>139</b>
	<b>Acknowledgements .....</b>	<b>141</b>
	<b>Declaration of Original Work.....</b>	<b>142</b>

# LIST OF FIGURES

Figure 1-1 Development cycle of micro-/nanoscale functional objects .....	4
Figure 1-2 Graphene flakes measurements.....	7
Figure 2-1 Lateral resolution of microscopes .....	14
Figure 2-2 Radiation field regions with respect to the electromagnetic wavelength $\lambda$ .....	17
Figure 2-3 Lumped circuit elements of the probe-sample interface .....	18
Figure 2-4 Conductive tip probing a SiO <sub>2</sub> substrate .....	20
Figure 2-5 Tip-sample wave interaction in various heights above a silicon dioxide surface. .	20
Figure 2-6 Influence of three materials to the wave propagation at 10 GHz.....	21
Figure 2-7 Laser interferometer based AFM-in-SEM. a) Schematic block diagram and b) Optic path.....	26
Figure 2-8 Laser interferometer based AFM-in-SEM: Photographs .....	27
Figure 2-9 Block diagram of the IF-Head-Adjust Control Commander.....	28
Figure 2-10 AFM test grating TGZ2.....	30
Figure 2-11 Resolution testing by using AFM test grating TGZ2 .....	31
Figure 2-12 Thermomechanical noise displacement measurement .....	32
Figure 2-13 Frequency spectrum of Scanning Probe Microscopy (SPM).....	33
Figure 2-14 Principle schematic of a Scanning Microwave Microscope .....	34
Figure 2-15 Scattering Parameter of a two-port Device Under Test (DUT).....	35
Figure 2-16 Basic parts of a Scanning Microwave Microscope .....	37
Figure 2-17 Near-field microwave probe.....	42

Figure 2-18 Simulation results of the Near-field microwave probe .....	42
Figure 2-19 FEM RF 3D simulation of SEM <sup>2</sup> microwave probe .....	43
Figure 2-20 Signal attenuation over cable distance in SEM <sup>2</sup> . .....	44
Figure 2-21 Simulation results of the Near-field millimeter-wave probe.....	46
Figure 2-22 Near-field millimeter-wave probe .....	47
Figure 2-23 Testing of the near-field millimeter wave probe PCB.....	48
Figure 2-24 Measurement of the near-field millimeter wave probe in air.....	50
Figure 3-1 Equivalent circuit diagram for a SWNT over a ground plane.....	54
Figure 3-2 Impedance plot for a 100μm-long Single Wall Nanotube over a ground plane.....	55
Figure 3-3 Reflection coefficient for a one-port network .....	56
Figure 3-4 Sensitivity enhancement of a commercial SMM at high impedances .....	58
Figure 3-5 Schematic of a Mach-Zehnder interferometer for measuring high impedances ....	60
Figure 3-6 Schematic representation of a 3-port circulator .....	62
Figure 3-7 Signal flow graph of circulator version of high-impedance microwave interferometer .....	64
Figure 3-8 Schematic of High-impedance microwave interferometer .....	65
Figure 3-9 Comparison of three types of microwave interferometer .....	66
Figure 4-1 Schematic of the Scanning Electron, Force and Microwave Microscope. ....	74
Figure 4-2 Integration into the vacuum chamber of the Zeiss LEO 1450 SEM.....	75
Figure 4-3 Photograph of the probing head, AFM-scanner and sample stage.....	76
Figure 4-4 Software control architecture of SEM <sup>2</sup> by Offis Automation Framework.....	78
Figure 4-5 AFM/SMM-Controller .....	79

Figure 4-6 AFM-DAC-Highend frontend.....	81
Figure 4-7 Simulation hardware to emulate varying $S_{11}$ -Parameter .....	82
Figure 4-8 Hardware-in-the-loop emulation of microwave properties.....	83
Figure 4-9 Layout of the multimodal test standard.....	89
Figure 4-10 Detailed zoomed images of the multimodal test standard. ....	90
Figure 4-11 Electron micrographs of the finding structures .....	91
Figure 4-12 Cross-sectional view of the investigated microcapacitor.....	92
Figure 4-13 Comparison: Capacitance vs diameter of metal dots .....	94
Figure 4-14 Flowchart of a vision-based robotic SMM calibration routine of micro-scale capacitors.....	97
Figure 4-15 Microphotograph of fabricated Multimodal Test Standard.....	98
Figure 4-16 SEM micrograph of cantilever with the SMM test features .....	99
Figure 4-17 Spatial distribution of topography.....	100
Figure 4-18 Topography line scan of two different microcapacitors with SEM <sup>2</sup> and JPK Nano-Wizard.....	101
Figure 4-19 3D color and top projection contour map of magnitude and phase of reflection coefficient $S_{11}$ measured by SEM <sup>2</sup> .....	102
Figure 4-20 Microwave sectional profile measured by SEM <sup>2</sup> of one microcapacitor.....	103
Figure 4-21 CAD Sketch of a Memristor sample .....	104
Figure 4-22 2D maps of topography, magnitude and phase of reflection coefficient $S_{11}$ of memristor devices measured by SEM <sup>2</sup> .....	106
Figure 4-23 3D view of a topography scan of two micro-scaled capacitors based on non-raster scan option of the AFM/SMM-Controller .....	107

Figure 5-1 Photographs of prototypes: a) Self-sensing near-field probe and b) Miniature Microwave Materials Analyzer..... 113

# LIST OF TABLES

Table 1-1 Three subdivisions of nanoelectronic technology direction “Beyond CMOS” .....	3
Table 2-1 Near-field probes .....	22
Table 2-2 Datasheet AFM-Scanner and Servo-Controller .....	28
Table 2-3 Reported targeting applications of SMM.....	38
Table 4-1 Datasheet AFM/SMM-Controller .....	80
Table 4-2 Multimodal microscopy test standards .....	86
Table 4-3 Datasheet Multimodal test standard.....	94

This page left intentionally blank.

# 1 INTRODUCTION

Research institutes and industry active in the area of micro-/nanotechnology and semiconductors identified future challenges in materials characterization and measurement methodology to meet the requirements of the next generation devices and circuits in micro- and nanoelectronics.

Further increase of feature densities of integrated switching and memory devices and circuits while reducing the power consumption, and heterogeneous integration of multiple technologies are promised by exploring into the directions “More Moore” and “Beyond CMOS”. While “More Moore” describes development on new complex material stacks, 3D heterogeneous system integration and electrical interfaces to extend CMOS technology (IRDS 2016c), “Beyond CMOS” deals with emerging materials and the resulting devices itself (IRDS 2016a). In processes driven by “More Moore”, the transistor gate length, a measure of the downscaling trend, has reached 10 nm in year 2017 at production level. This extension of CMOS techniques is done by stacking transistors in 3D space with, so called FinFETs, by rotating the Source-Gate-Drain area by 90 degrees. Other types of transistors falling into this direction are Carbon Nano Wire FETs and very low threshold tunneling FETs. These FETs operating with controllable thickness of the tunneling barrier by changing electric fields. Semiconductor research is also working on “high- $\kappa$ ” gate and capacitor dielectric thin films. “High- $\kappa$ ” translates to high static dielectric constant  $\kappa$  and by using such materials in integrated circuits the overall device volume shrinks. Under investigation as replacement materials for silicon dioxide ( $\text{SiO}_2$ ) are following dielectrics

- Amorphous metal oxides, like aluminum oxide ( $\text{Al}_2\text{O}_3$ ) ( $\kappa=9$ ) and tantalum pentoxide ( $\text{Ta}_2\text{O}_5$ ) ( $\kappa=26$ ),

- Transition metal oxides, such as hafnium dioxide ( $\text{HfO}_2$ ) and zirconium oxide  $\text{ZrO}_2$ , both with a dielectric constant of 25,
- Mixed oxides, like hafnium silicate ( $\text{HfSiO}_4$ ) ( $k = 13$ ) and zirconium silicate ( $\text{ZrSiO}_4$ ) ( $\kappa = 9$ ) and
- Ferro- and piezoelectric materials such as barium strontium titanate ( $\text{Ba}_x\text{Sr}_y\text{TiO}_z$ ) and lead zirconate titanate (PZT).

Another issue in “More Moore”, is the enhancement of charge carrier mobility for stacked configurations. This can be realized by using so called “strained silicon”, silicon-on-insulators (SOI), III-V-semiconductors, such as gallium nitride or indium nitride and other substrates. Additionally, caused by the permanent increase of digital clock frequencies in integrated circuits, interconnects between stacks are in focus. This concern backend and 3D chip integration.

The second technology trend - “Beyond CMOS” - targets to non-conventional materials and devices concepts beyond the limits of present CMOS technology to encode information. This orientation of future nanoelectronic direction divides into three types, describing new transport and gating mechanisms and introducing new state variables (see Table 1-1). The term “state variable” relates to the physical quantity, how internal state, input/output signals and switching of nanodevices are encoded (EU FP7 ICT NANO-TEC 2013).

The third direction, called “More-than-Moore” allows for migration of non-digital functionalities, such as RF communication, power control, sensors, actuators or passive components, onto the chip or into the package.

Table 1-1 Three subdivisions of nanoelectronic technology direction “Beyond CMOS”

<i>Type of mechanism</i>	<i>Concept/Devices</i>
Charge-based state variable	Logic devices made of Graphene / Nanowires,  Molecular level control of device properties (“Molecular electronics”).
Non charge-based state variable	Logic state change by its <ul style="list-style-type: none"> <li>• mechanical position (“Nano Electro Mechanical Systems (NEMS)”)</li> <li>• magnetic dipole/spin (“Spintronics”),</li> <li>• electric dipole (“Ferroelectrics”) and</li> <li>• orbital state in e.g. quantum wells (“Orbitronic”).</li> </ul>
New computing paradigms	Unconventional, “non-Turing” methods in processing the information, such as <ul style="list-style-type: none"> <li>• “Neuromorphic computing” and</li> <li>• “Quantum computing”.</li> </ul>

Looking at the development stages and the life cycle of micro- and nanoscale functional objects, the following can be discerned. In order to be integrated into the final application or a system, these micro-/nanoobjects undergo through different phases. Figure 1-1 illustrates the different phases of “life” with their respective sub-processes. A solution approach, that combines some of these processes with a multimodal microscopy technology and its expandability by the use of nanorobotics, is located in the center of the diagram.

In an initial step, the **theoretical** functional mechanisms are worked out leading to a model describing the functionality of the component. Through approximation, computer simulation and corresponding fine-tuning, a first model is established and prototypes can be manufactured.

There are different approaches of micro-/nano-**fabrication**. In the “Bottom-up” approach, parts are assembled into functional components on an atomic or molecular level, through coordinated chemical and physical processes, by means of self-assembly and subsequent self-organization.

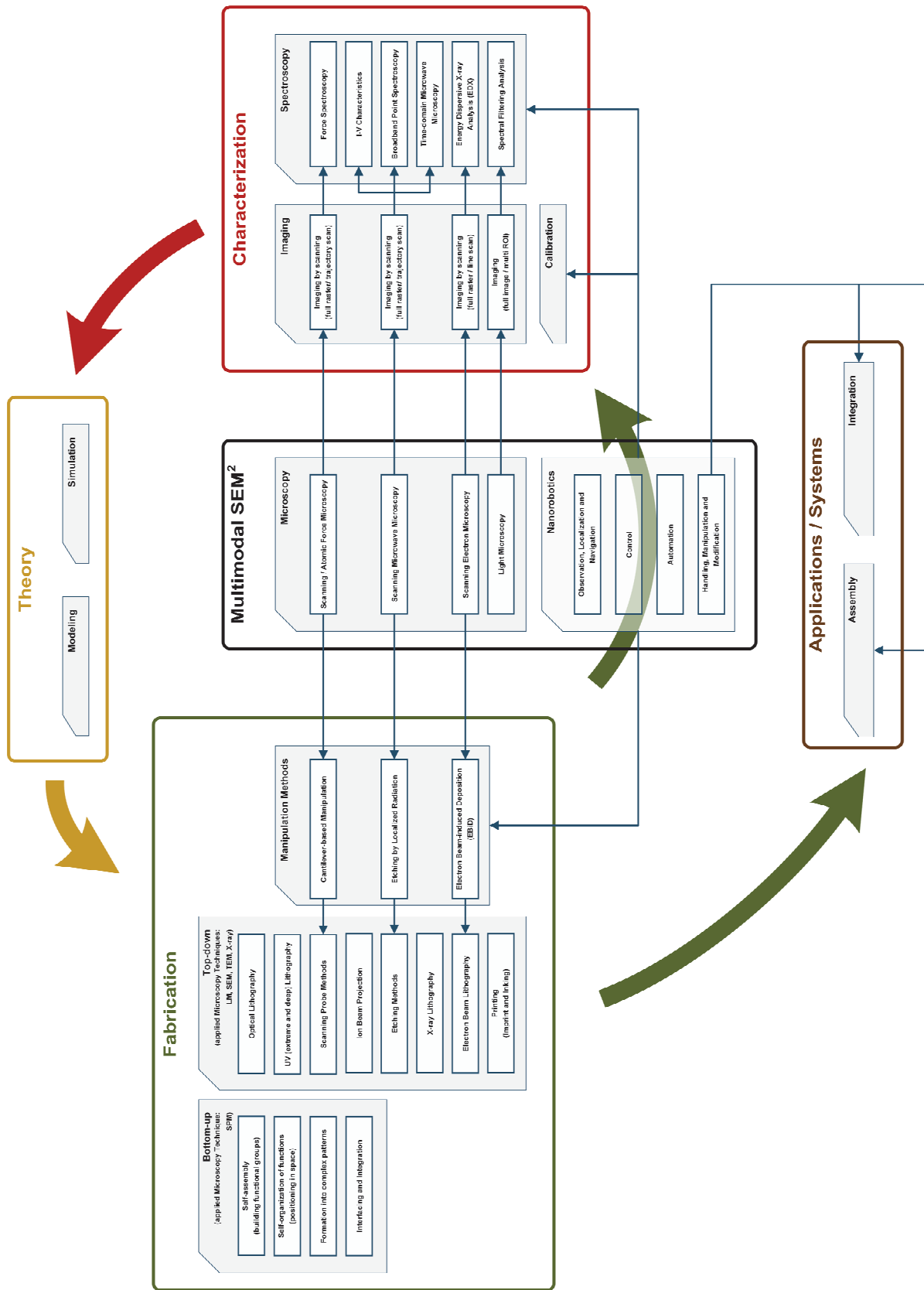


Figure 1-1 Development cycle of micro-/nanoscale functional objects that lead from Theory via Fabrication and Characterization to Applications or Systems. A multimodal microscope and robotic technology (SEM<sup>2</sup>) combines a few processes of characterization, fabrication and system-level integration.

In a further step, formation processes are performed to integrate the components into more complex functional groups. While in the “Top-down” approach, the manufacturing process chain is worked down from large bulk materials to the smallest possible structures, such as Micro-Electromechanical Systems (MEMS).

Relevant process techniques, like lithography and etching or nanoimprinting, are tabulated in the fabrication block of Figure 1-1. Depending on the approach deployed, different microscopy techniques are used to visualize the produced objects in the production process. Both approaches have their respective advantages and disadvantages in terms of reproducibility, production speed or cost.

The prototypical function blocks are tested in various in- or offline measuring and **characterization** steps to verify its functionality. In this area, a wide variety of measurement processes have been established, from pure imaging procedures to multidimensional, calibrated spectroscopic methods. Merging multiple modes of scanning microscopy methods to extract various and often unique information about physical properties of samples-under-test, addresses most of the above mentioned challenges in semiconductor and materials research. The gained characterization results, flow into an improved theoretical understanding and thus into more accurate models optimizing production processes.

In the last step, assembly and integration over different dimensional scales into the respective target **application** or **system** takes place by support of robotic approaches.

As shown a steadily diversifying landscape of new devices and systems in the field of material sciences and semiconductor research with its new fabrication methodologies and processes, demands to enhanced and novel characterization and manipulation solutions. Analyses of nanoscale features and defects with highest resolution by applying dedicated techniques are required. Reports prepared by groups of experts from the semiconductor sector, such as the

“International Technology Roadmap for Semiconductors” (Sematech 2015) and the IEEE International Roadmap for Devices and Systems (IRDS 2016b) specified a number of potential solutions:

- **Multi Heads/Columns and Modes for Scanning Instruments**

allow for extracting different types of information, such as dimensional and material data,

- **Hybrid Metrology**

combine multiple instruments, achieves higher resolution and measurement speed and reduces uncertainty at characterization of different aspects of a feature,

- **Broadband RF Measurements**

give information about the properties of components and systems over a wide frequency spectrum and

- **Non-raster Capabilities for Scanning Instruments**

enable the extraction of data from non-orthogonal axes to speed up the imaging process through spiral, cycloid or Lissajous trajectories.

The potential of extracting and visualizing different properties from the same region of interest (ROI) of one of the new promising materials, illustrates Figure 1-2. The sample shown is composed of flakes of graphene deposited onto a silicon substrate. Graphene, a microscopic large two-dimensional network of carbon atoms, is an integral of the “Beyond CMOS” direction. The scanning microscope raster in contact mode the surface and is able to image two physical properties: The topography of the sample surface and its ability of modifying evanescent incident electromagnetic waves. In the geographic area of the deposited flakes, encircled by the red dotted line, the left image shows no visible large flat objects, but on the

right side the flakes are observable, as pink colored parts on top of the surface. Therefore, it is promising to apply such technology in a multimodal approach.

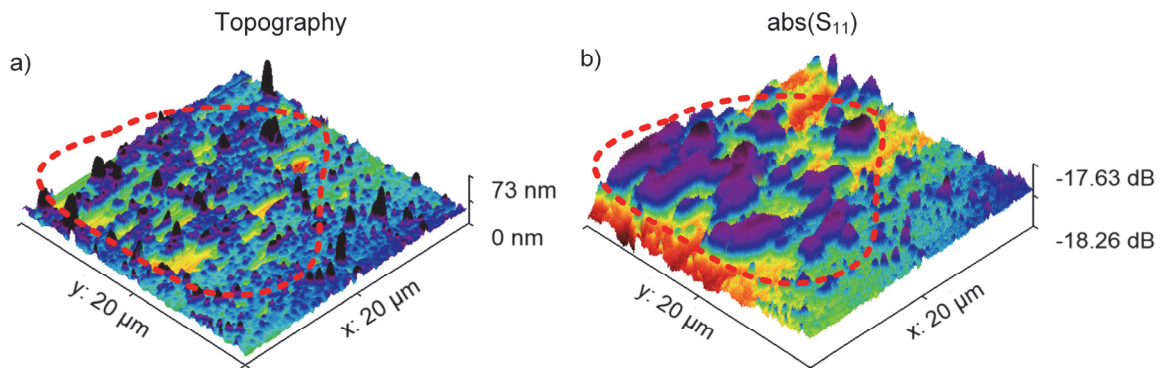


*Figure 1-2 Graphene flakes measurements –the region inside the red dotted line- conducted with an interferometric Scanning Microwave Microscope (iSMM) at IEMN. a) 3D Topography scan image indicates no existence of a 1D thin layer conductive material. b) 3D Scan of  $abs(S_{11})$  displays areas of different conductivity, which might be a reaction originating from on top placed flakes of graphene.*

A further closer look at the ITRS and IRDS roadmaps, reveals the following application fields of electrical characterization targeting the above mentioned challenges: “Characterization of dielectrics (high- and low- $\kappa$ )”, “Metrology of RF interconnects”, “Measurement of dopant profiles and positions” and “Mapping of buried defects”. In order to meet the requirements of these actual and future areas of application in material and semiconductor science, new multidimensional and -modal characterization and manipulation tools must obviously be created. Due to the diversity of the proprietary characterization systems used, the demand for open software and hardware architectures is growing. This in turn permits the integration of further image-assisted robotics, which then enables automation of measurement, calibration, assembly and processing techniques.

## 1.1 Objectives

This work has the ambition to provide a technology for the treatment of the above mentioned challenges and issues in the fields of imaging, characterization and manipulation at micro- and nanoscales. To this end, the following methodology approaches needs to be developed and validated:

- A vacuum-compatible near-field microwave microscope for usage in custom scanning electron microscopes, operating up to 20 GHz in the frequency domain, as an instrumental setup to its application to measure high-impedance nanoelectronic devices. In order to be able to operate in different SEM's, the size of the vacuum unit shall be smaller than other known devices.
- The fusion of three scanning microscope modalities, scanning electron (SEM), atomic force (AFM), and microwave microscopy (SMM), plus light microscopy (LM), shall evolve into a new hybrid microscope technology. It shall allow for the acquisition of additional dimensional information to be used in such a manner that a reduction in characterization uncertainty can be achieved. Inspecting the scanning probe quality with an SEM, without removing it out of the vacuum workspace is an advancement in SMM research. A specially designed multimodal test standard shall bridge the modalities.
- The integration of the technology approach into an open hard- and software control technique, introducing robotic methodologies and arbitrary scan paths, provides a new sensor and imaging technology in nanorobotic and microwave microscopy research.
- The technology and its performance in an operational environment should demonstrate, that it is a beneficial technology to semiconductor and material science.

---

The domain of microwave microscopy research is running like a common thread through these objectives. It attracts more and more research groups and is even recently beginning to evolve into commercial instruments. But it's more than only a new type of microscope. Due to the fact, that the physics and instrumental methods behind the images are still under heavy investigations and the applications of this technique are growing in numbers and diversity, the author see the imperative of joint activities by complementary research fields. In this thesis, the overall goal is to create a new technology by merging the knowledge originating from the fields of electromagnetics, semiconductor physics, material science, engineering (optical, electronic and mechanical) and computer science.

## 1.2 Outline / Author's Contribution

The author contributes to the advancement of dedicated multimodal scanning microscopy at the submicrometer scale in five chapters following this introduction.

**Chapter 2** introduces the technology of a Scanning Microwave Microscope (SMM) integrated into a Scanning Electron Microscope (SEM). Aspects of the near-field interaction between probe and sample are explained. Furthermore, a size-reduced laser interferometer-based scanning force microscope for the operation inside SEM's is described in detail. Its performance is verified by measuring a commercial AFM test standard. After introducing into the basic systematics of microwave microscopy and its applications, the chapter concludes with two variants of high-frequency near-field probes including analyses and optimization of their microwave properties.

**Chapter 3** concerns with issues arising when measuring in the nanometer range using conventional RF measurement technology. Principles and current approaches are discussed, followed by details of a more sensitive version of a microwave interferometer plus a comparative study.

**Chapter 4** depicts a multimodal sensing and imaging technology approach by combining the microscopy modalities of light, electron, atomic force, and near-field microwave with robotics. A technology demonstrator and its control architecture is described in detail. By using a hardware-in-the-loop emulation environment, this system approach is evaluated in general.

In order to calibrate the different modalities of this technology, a multimodal test standard is required. Such a test sample is described in the last part of this chapter, with an approximation formula for micro-scale capacitors. Thereafter, there are descriptions of studies to verify the usability of this standard and the technology approach itself.

**Chapter 5** summarizes the results of the overall work and discusses the main aspects that have been addressed. Future expansions together with an outlook of the presented work round off and complete it.

This page left intentionally blank.

## 2 INTEGRATED AFM-IN-SEM AND SMM

**Scanning Electron Microscopy (SEM)** is an important method for surface structure analysis of samples, which is widely used in research and development in areas such as semiconductor physics, nanotechnology and biology. With this microscopy method, a focused electron beam scans across the sample-under-test (SUT) line by line in a vacuum environment. The interaction products, like back-scattered electrons, secondary electrons, X-rays, amongst others, generated by the primary electrons interacting with the DUT, are captured and displayed as an image. The SEM can be used to examine structures with a resolution of only a few nanometers with a high depth in focus and a depth of field that is 1000 times greater than that of the light microscope. Not every sample, e. g. of organic origin or optical devices, can be observed with an SEM. The necessary sample preparation is not unproblematic and may change the characterization results. Furthermore, the exposure to electrons also leads to unwanted deposition processes, which in turn can change the properties of the object to be observed.

**Scanning Force Microscopy (SFM) or Atomic Force Microscopy (AFM)** is a widely used method of mapping and measuring the topography with atomic spatial resolution for any material. An ideally atomically sharp probe tip is guided across the surface of the sample-under-test in a raster-like scan, steered by piezo-actuators. The tip is mounted on a “soft” cantilever spring. The forces interacting between with tip and the sample changes under the influence of the sample topography. The significant forces are van-der-Waals and Coulomb or electrostatic forces. The most widely used technique of sensing these forces is the laser-reflection-photodiode principle. By reflecting a laser beam from the cantilever into a position-sensitive photodiode, the deflection of the cantilever and thus the effective forces can be

registered (see right side in Figure 2-16). In the case of controlling by a constant force, the tip follows the surface structure and the control parameters are converted into a 3D image.

While the lateral resolution is quite similar in both microscopy techniques, the SEM offers a large field of view in the range of tens of square millimeters comparing to typically  $100\ \mu\text{m} * 100\ \mu\text{m}$  in AFM. A graphical comparison of the lateral resolution of microscopy methods depicts Figure 2-1. STM denotes to Scanning Tunnel Microscopy and STED to Stimulated Emission Depletion Microscopy, which is a type of Fluorescence Laser scanning microscope working in the far field mainly used in bio applications.

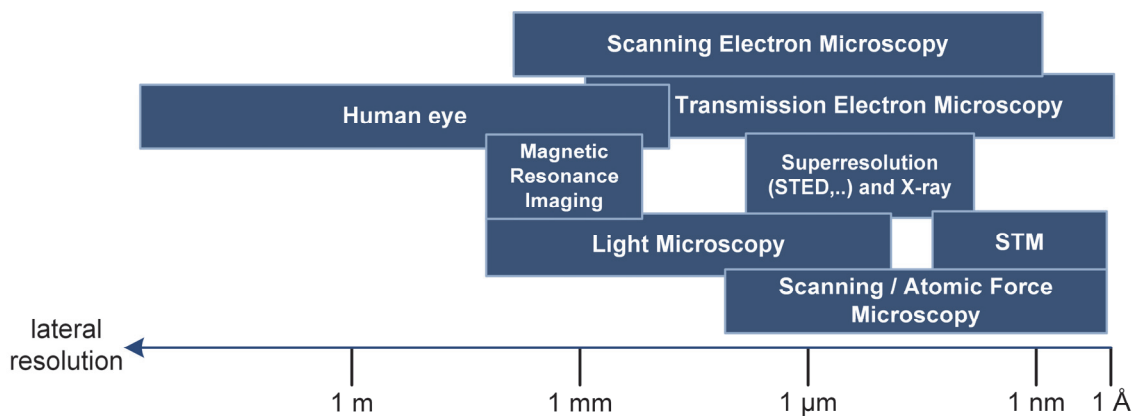


Figure 2-1 Lateral resolution of microscopes.

Another advantage of SEM is the fast image acquisition speed. Typical frame rates in a single beam SEM, not of a high-class SEM with up to 91 parallel beams (Zeiss Corp. 2015), are 20 Hz to 1 Hz for navigation, with a low signal-to-noise ratio, and up to 0.01 Hz and more to obtain a high-quality image. A typical AFM, not a high-speed video-rate one, needs at comparable pixel resolution a factor of 1000 more time. On the other hand, an SFM or AFM features atomic resolution in the vertical scale like an STM. In addition, the AFM is a very precise instrument for measuring mechanical properties such as elasticity and hardness and last but not least, the utilization as a patterning instrument in Scanning Probe Lithography (Carpick, Salmeron 1997; Schumacher et al. 1999; Zimmermann 2017).

**Scanning Microwave Microscopy (SMM)** is bringing quantitative broadband measurements at high and microwave frequencies to the molecular and atomic scale to investigate their electrodynamics. The ongoing miniaturization requires measurement tools, such as SMM (Imtiaz et al. 2014a), to characterize and optimize complex conductivity of hetero structure materials, electron-charge- and electron-spin-based devices, bioinspired objects, magneto-resistive functionalized items, and superconductor-based devices. They are candidates for the research on “More Moore” and “Beyond CMOS”. Other areas of operation are the investigation of materials such as 2D materials, carbon nanotubes (CNTs), ferromagnetic and -electric materials and life-science materials. Although local measuring and controlling of sheet resistance, doping profiles and electro migration in conducting wires in the process chain of semiconductor integrated circuits are examples of studies with SMM. The properties of all these devices can be investigated at the operating frequency of their particular application.

Chapter 4 is devoted exclusively to the integration of the microscopy techniques described in this chapter.

## 2.1 Probe-Sample Interface

Before looking to the RF electromagnetic interaction between the probe tip and the sample-under test, a short excursion to the influencing forces at this interface follows.

The interacting forces among the probe tip and sample surface can be differentiated into long and short range forces. If the tip approaches the sample, the interaction forces must be taken into account. These are essentially Coulomb and van der Waals forces, which can be described by the electrical potential energy  $U_E$  (Ibach, Lüth 2003)

$$U_E = \frac{1}{4 * \pi * \epsilon_0} * \frac{q_1 * q_2}{r} - \frac{c}{r^6} ,$$

(Eq. 2-1)

with distance  $r$ , the charges  $q_1$  and  $q_2$  on the sample-under test (SUT) respectively the probe tip, the vacuum permittivity  $\epsilon_0$  and a material specific constant  $c$ . The first term denotes for the Coulomb and the second term for the van der Waals effect. If both the tip and the sample are electrically neutral, the coulomb term is zero and the tip underlies an attractive force due to the interaction of the induced dipole moments. With further approaching, the electron orbitals of the atoms of the probe tip begin to overlap with atoms of the sample. Due to the Pauli principle, the tip experiences a strongly repelling force, if  $d < 2\text{\AA}$ . If this force and the van der Waals interaction are taken into account, the so called Lennard-Jones 12:6 potential  $U_{LJ}$ , an approximate function, is obtained (Whalley, Schneider 1952)

$$U_{LJ} = 4 * \epsilon \left[ \left( \frac{\sigma}{r} \right)^{12} - \left( \frac{\sigma}{r} \right)^6 \right] ,$$

(Eq. 2-2)

while  $\epsilon$  represents the magnitude of the minimum potential well-depth in Joule caused by the two interactions and  $\sigma$  denotes to a combination of atom specific distance constants.

When measuring in air, the sample surface is covered with a water film. The resulting capillary forces increase the total attraction force. Such adhesive forces can be avoided by measurements in vacuum or under liquids.

In case of probing a sample with high frequency waves, one must consider other effects. Abbe's resolution limit of optics limits the highest spatial resolution obtained is in the order of wavelength  $\lambda/2$ . To reach nanometer-scale spatial resolution it needs a look to the physics of the fields and radiation generated by a local oscillating source with size  $D$ , the microwave microscope's probe. When studying compared to the wavelength  $\lambda$  small antennas or radiating structures, three spatial regions of the electro-magnetic field exist (Figure 2-2):

- the far-field or Fraunhofer region (radiation): relevant distance  $r \geq 2 * \lambda$  and  $r \gg D$  Abbe's resolution limit applies here. The electric and magnetic fields are in-phase.
- the intermediate zone (induction):  $D \ll r \sim \lambda$ ,
- the near-field (quasistatic):  $D \leq r \ll \lambda$ ; the operating range of SMM.

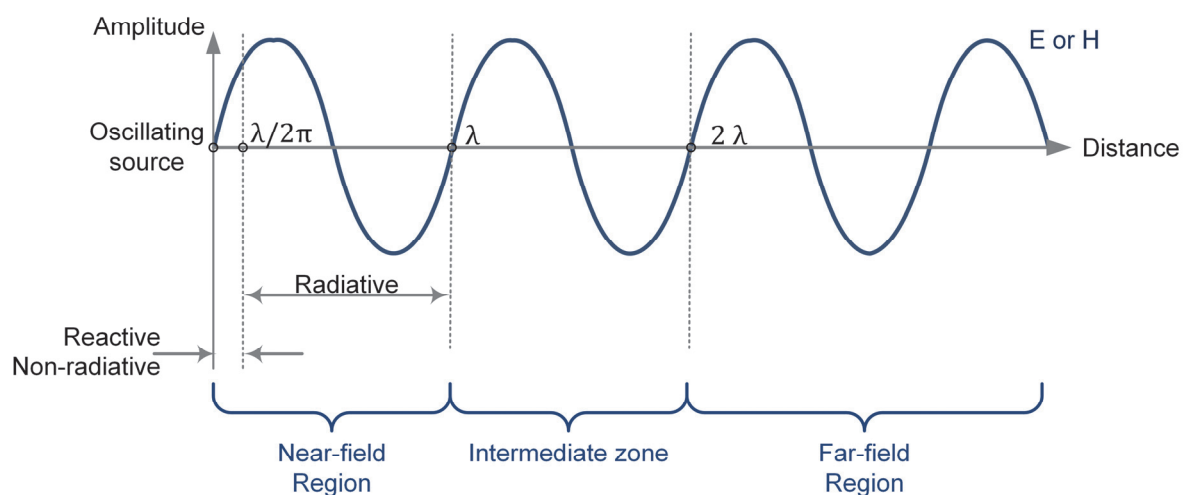
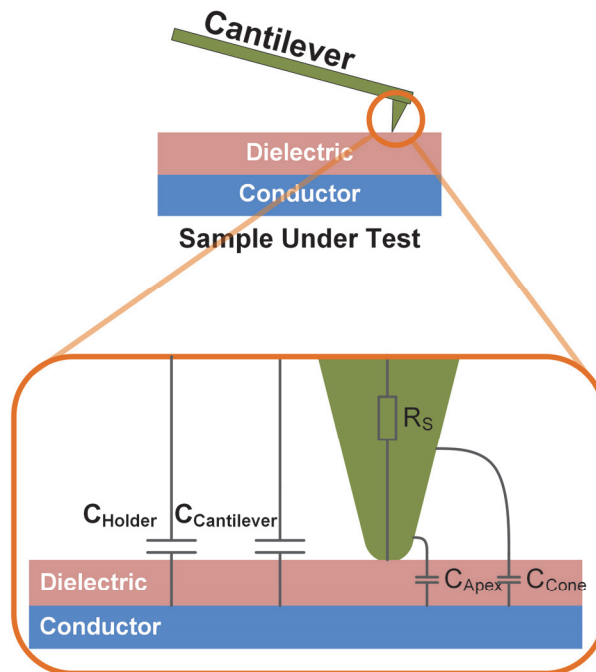


Figure 2-2 Radiation field regions with respect to the electromagnetic wavelength  $\lambda$ .

The complex electric and magnetic fields in the near field region around the probe acts quasi-static and are evanescent. Which means that they behave static, in terms of spatial extension, but oscillating harmonically in time. The evanescent wave coming out of the tip, radiates into the surrounding area and store reactive electromagnetic energy. The wave is not propagating, meaning carrying energy away and exponentially attenuated with distance. The shaping of these fields is a result of the probe geometry and the electromagnetic properties of the probed sample-under-test. The probing system is considered as a distributed resistive-capacitive (RC) network. Figure 2-3 shows the tip-sample region and its simplified different capacitances and resistor as lumped circuit element representations of a cantilever probe tip and the SUT with a layer of dielectrics on top of a conducting layer.



*Figure 2-3 Lumped circuit elements of the probe-sample interface with a sharp tip as microwave probe. Below a zoomed image with probe tip and sample. The cantilever and its tip is in green.*

Four capacitive parasitics are storing the electric field energy. The chip holder of the cantilever itself and the cantilever representing the largest capacitors  $C_{Holder}$  and  $C_{Cantilever}$  respectively.

The coupling between probe-tip and sample is taken place through the tip resistance  $R_s$  and the capacitance of the Cone  $C_{Cone}$  and the tip apex  $C_{Apex}$  to the SUT at the end. The geometry of the entire probing device should be minimized, in terms of parasitic capacitances and resistance. Karbassi et.al. simulated and measured the interaction of the total probe-tip-capacitance with different sample thicknesses and radii with this lumped element model (Karbassi et al. 2008). The SUT was conductive silicon with a  $SiO_2$  dielectric film on top. Three different radii of the apex, were simulated by Finite Element Methods (FEM) and compared to measurements. In this configuration, the total parasitic capacitance of  $C_{Holder}$ ,  $C_{Cantilever}$  and  $C_{Cone}$  was found to be 57 fF at 44 nm thickness, while  $C_{Apex}$  was measured to be 2 fF. An understanding of these dependences and including it into calibration routines and protocols, is one major issue in Scanning Microwave Microscopy and still under research.

The obtainable resolution with incident electromagnetic microwaves in the near field is ruled, instead of the wavelength  $\lambda$ , by the probe-sample-distance  $r$  and size  $D$  of the probe. In order to meet the condition of near-field operation during probing, this means that the *Size of the radiating source*  $D \leq \text{Tip-Sample Distance } r \ll \text{Wavelength } \lambda$ .

If the tip-sample distance is within this range, electro-magnetic microwave simulation can be performed to show the influence of a varying distance between a tip and a silicon substrate on the electric field concentration. Figure 2-4 shows a conductive platinum tip with a diameter of one micrometer above a substrate, which served as a model in a simulation with HFSS (Ansys Corp.) at 10 GHz. The influence of varying the tip-sample-distance to the e-field concentration displays Figure 2-5.

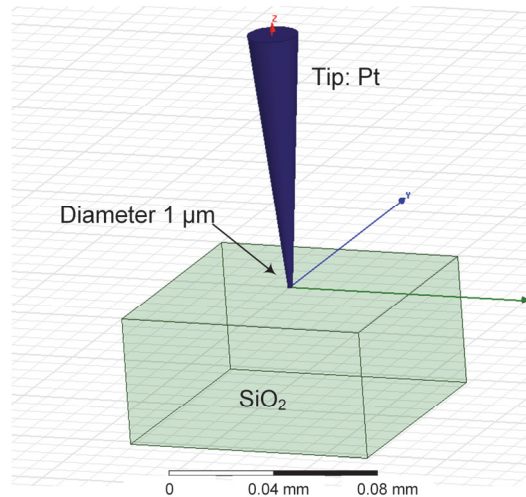


Figure 2-4 Conductive tip probing a  $\text{SiO}_2$  substrate. The diameter at the end of the tip is  $1 \mu\text{m}$ . Dielectric constant of silicon dioxide 3.9.

The electric field increases quadratic inverse to the distance, the field lines confine due to the permittivity step from air to  $\text{SiO}_2$  at the probe-sample-interface and penetrates the material.

The evanescent wave reflects back and a shift in the reflection coefficient is measured.

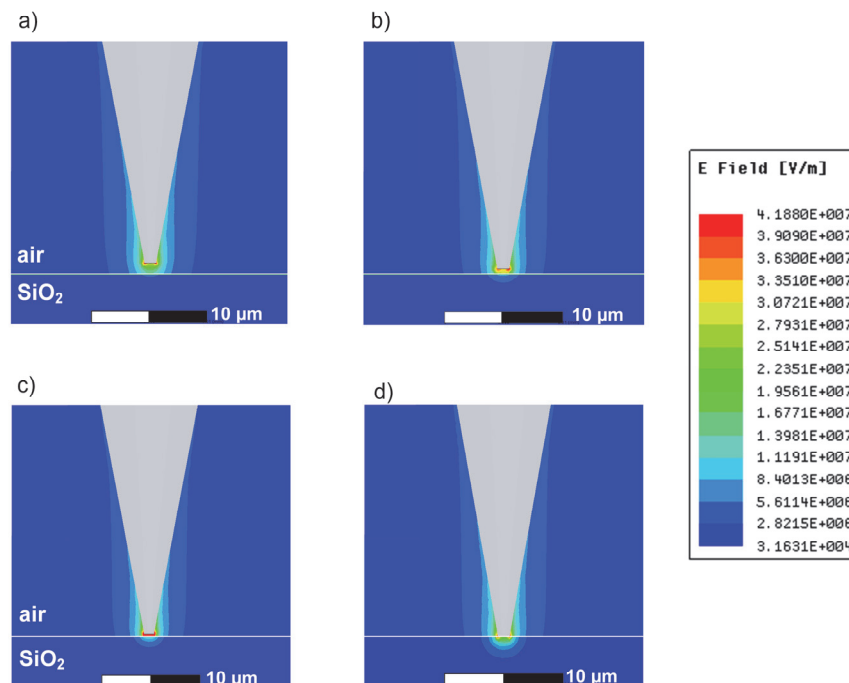


Figure 2-5 Tip-sample wave interaction in various heights above a silicon dioxide surface. E-Field simulation contour plots at 10 GHz with the tip in air moving towards the sample. Scale bar  $10 \mu\text{m}$ . Tip-Sample-Distance: a)  $1 \mu\text{m}$ , b)  $500 \text{ nm}$ , c)  $250 \text{ nm}$  and d) in contact.

The field confinement effect shows the next FEM e-field contour plots Figure 2-6. Three different types of samples consisting of Polytetrafluorethylen (PTFE), Silicon dioxide, and a substrate used in microwave circuits, RO3010 (Rogers Corp.) with varying permittivity have been chosen. The squeezing field effect is strong observable with the high- $\kappa$  materials, such as RO3010 (Figure 2-6 c ).

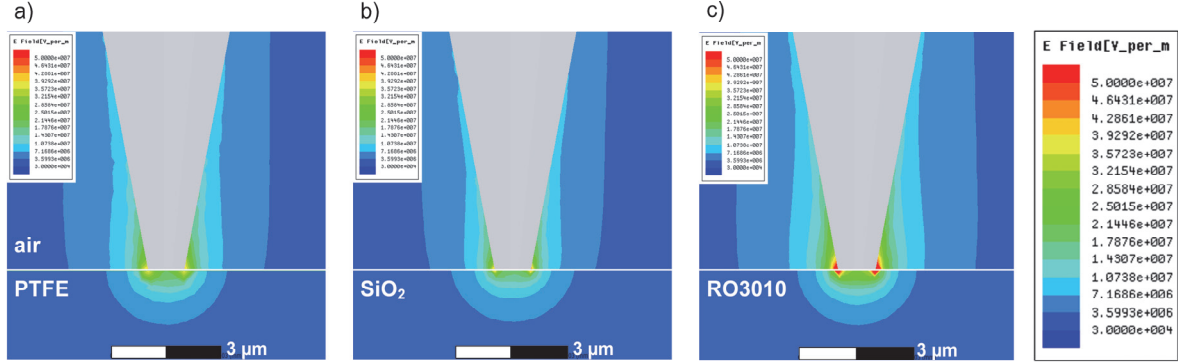


Figure 2-6 Influence of three materials to the wave propagation at 10 GHz. E-Field simulation contour plots in contact with surrounding air in the upper part. Scale bar 3  $\mu\text{m}$ . a) PTFE ( $\epsilon_r = 2.1$ ). b) Silicon dioxide ( $\epsilon_r = 3.9$ ) and c) High-frequency laminate Rogers RO3010 ( $\epsilon_r = 10.2$ ).

Due to the frequency-dependent penetration depth of electromagnetic waves, the skin effect, the waves can penetrate deeper into the bulk material at lower frequencies. The thickness of the skin  $\delta$  expresses as follows

$$\delta = \frac{1}{\sqrt{\pi * \mu_0 * \mu_r * \sigma * f}},$$

(Eq. 2-3)

where  $\mu_0$  is the magnetic permeability of vacuum ( $4\pi * 10^{-7} \frac{\text{Vs}}{\text{Am}}$ ),  $\mu_r$  the relative permeability and  $\sigma$  the electric conductivity in [S/m] of the sample. By using this effect, Plassard et al. investigated with an SMM buried calibrated metal defects down to 125 nm as a tomographic technique (Plassard et al. 2011).

With appropriate small tip or aperture geometries, connoting to the size of the oscillating source, it is possible to localize the electromagnetic fields to induce microwave currents into the sample. Different probes, sensitive to electric or magnetic fields, are in use in SMM and can be divided into probes with an aperture and without, as shown in Table 2-1.

Table 2-1 Near-field probes (metal in green, dielectric in grey, SUT in blue).

<i>With aperture</i> <i>Sensitive to electric field</i>	Waveguide with aperture (Golosovsky et al. 1996)	Open-end of coaxial waveguide (Cho et al. 1996)
	Open-end of parallel stripline (Talanov et al. 2006)	
<i>Sensitive to magnetic field</i>	Loop wire (Lee et al. 2000)	Superconducting Quantum Interference Device (Black et al. 1995)
<i>Without aperture</i> <i>Sensitive to electric field</i>	Coaxial waveguide with sharp tip (Gao et al. 1997)	AFM cantilever tip (Tabib-Azar, Wang 2004)

---

Probes with an aperture offers only micrometer spatial resolution and are often used in quantifying dielectric properties of liquids, soft and hard materials. Apertureless near field probes, such as AFM tips, features nanometer resolution, but the parasitic coupling in the probe-sample interface makes it difficult to design and the analytical data interpretation in quantified measurements complex.

## 2.2 Combined Scanning Force and Electron Microscopy

Different approaches to integrate Atomic Force Microscopes into Scanning Electron Microscopes are known for over 20 years. In the first report, the electron beam of the SEM was focused onto the edge of the sensing cantilever and a change of number of scattered electrons, caused by the force-induced deflection, were detected (Ermakov, Garfunkel 1994). This modality disables the SEM operation, because the analysis of the cantilever deflection blocks the secondary electron detector for imaging. To investigate nanoelectronic transport processes and cathode-luminescence a combined AFM/SEM based on the laser deflection principle was introduced (Troyon et al. 1997; Fukushima et al. 2000; Joachimsthaler et al. 2003). A vacuum compatible commercial “Thermo-Microscopes Explorer” AFM inside an SEM has been used to pick and fix a carbon nanotube (CNT) between electrodes for further characterization (Williams et al. 2002). Commercial products of laser beam-deflection AFM for the integration into an SEM are available (Hang et al. 2009; Bolorizadeh et al. 2013). Another approach is by sensing the atomic forces with tuning forks (Lewis et al. 2014) or piezo resistive cantilevers (Stahl et al. 1994; Kreith et al. 2017; Angelov et al. 2016). Besides these cantilever readout techniques, optical interferometry was introduced as an AFM technique under ambient environment since the beginning of the invention (Erlandsson 1988), and also in an ultrahigh vacuum version (Kracke, Damaschke 1996). The force sensitivity reaches the atto-newton range with soft cantilevers (Stowe et al. 1997). The optical path and hence the parts of a Michelson interferometer requires less space than the typical beam deflector solution. The interferometer version therefore is favorable if only little room is available, as inside the vacuum chamber of an SEM, and furthermore to establish nano-automation techniques. The author is only aware of a commercial device from Attocube Corp., Germany (Attocube Corp.). The ease of adjustment and the opportunity to eliminate electro-magnetic disturbances by locating the electronics outside the region of measurement are other advantages, especially

when probing with high frequency electromagnetic fields. All these methods enable conventional AFM-based surface analysis inside an SEM, which means one cantilever, one application and no possibility to use microwave evanescent waves as a sensing modality in vacuum.

### **2.2.1 Design of a Laser Interferometer-based AFM-in-SEM**

To obtain information about the surface topography a vacuum compatible Scanning or Atomic Force Microscope based on an optical Michelson interferometer (PicoScale® / SmarAct Corp.) was designed (Figure 2-7 and Figure 2-8) and incorporated into the SEM vacuum chamber of a Zeiss LEO 1450. Reducing electronic parts integrated into the vacuum chamber, decrease the influence of external electromagnetic interferences, which induces into the S-Parameter measurement, and therefore, is essential.

The infrared laser is working at a wavelength of 1532 nm (NIST-traceable), sinusoidal modulated with a frequency of 30 MHz. This is then used as phase modulated interference signal. By subsequent demodulation, it is possible to extract a quadrature signal, which varies depending on the mirror position. More details are given in the user manual (SmarAct GmbH 2016). The light energy is coupled via optical fiber into an integrated optics head of 6.4 mm diameter [IF-Head; light red in Figure 2-7 a)]. The focused laser light shines onto the reflective side of the platinum cantilever. Figure 2-7 b) depicts the path of the laser beam with the designed collimator after the beamsplitter to get a spot size of 50  $\mu\text{m}$  on the cantilever. While scanning the measured deflection, the measured information of the cantilever feeds the AFM/SMM-Controller to move the AFM-Scanner (PicoCube® / Physik Instrumente Corp.) via the Servo-Controller (E-712K063 / Physik Instrumente Corp.) following the topography of the Sample-under-Test (SUT). Table 2-2 specifies some relevant data. The AFM acts as a



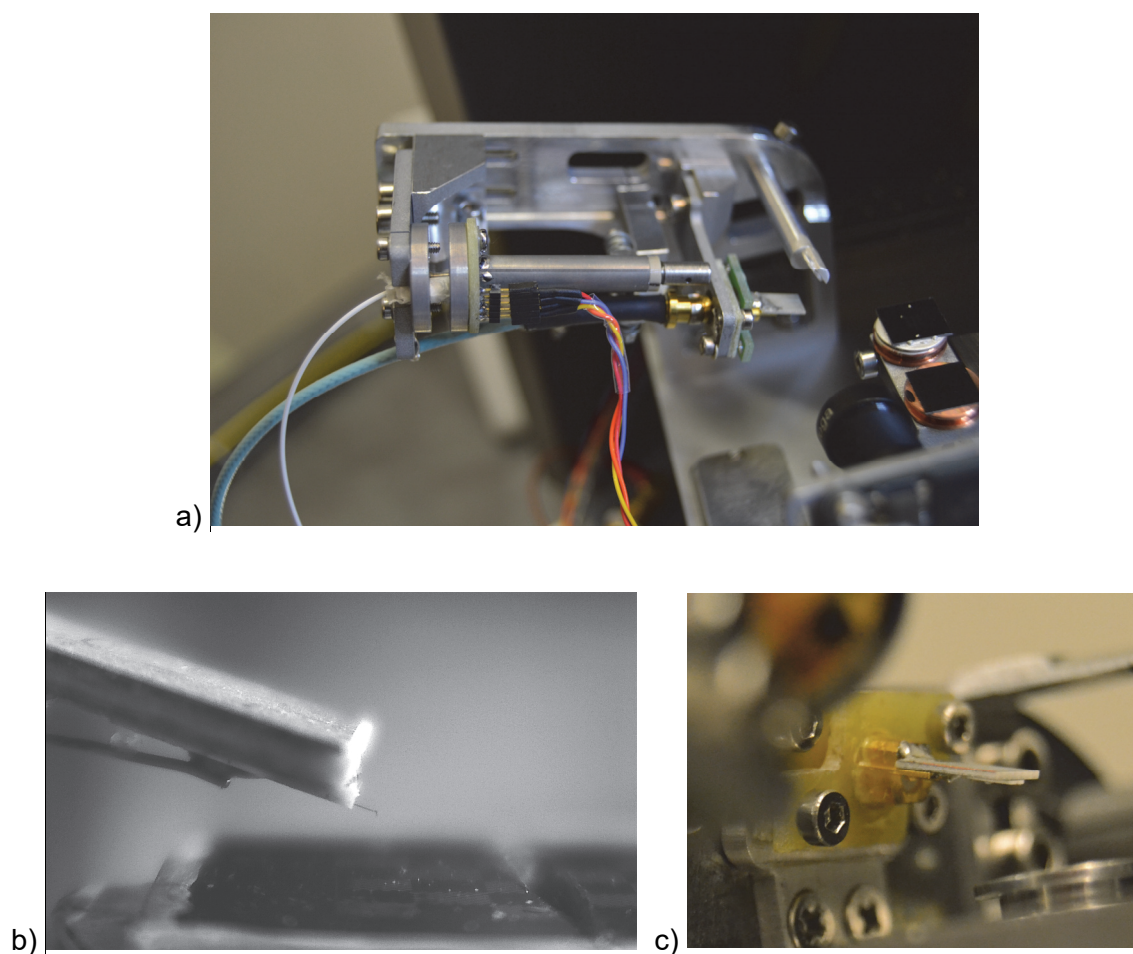


*Figure 2-8 Laser interferometer based AFM-in-SEM: Photographs. a) Details of non-moving Interferometer-Head, b) Camera side view: Near-field microwave probe (left) over a Chessy Calibration Specimen (Agar Scientific Corp.) and c) Photograph: Near-field microwave probe installed in SEM<sup>2</sup>.*

The IF-Head allows electronic steering of the laser beam by piezo ceramics inside the SEM chamber [inset in Figure 2-7 a)]. A piezo actuator tube (PT230.14 / PI Corp.) has four segmented electrodes with maximum 14  $\mu\text{m}$  end tip travel. To move the PZT tube in x and y, two high-voltages are applied. These voltages generates by a self-built IF-Head-Adjust Commander with low noise and manual respectively remote control (Matlab® / Python®) capabilities (Figure 2-9). A microcontroller (ATMega® 328 / Atmel Corp.) controls two 16 Bit-Digital-to-Analog Converters (AD5570 / Analog Devices Corp.) as their output voltages in turn are converted up to maximum  $\pm 150$  V by high voltage amplifiers (MA01 / Apex Corp.).

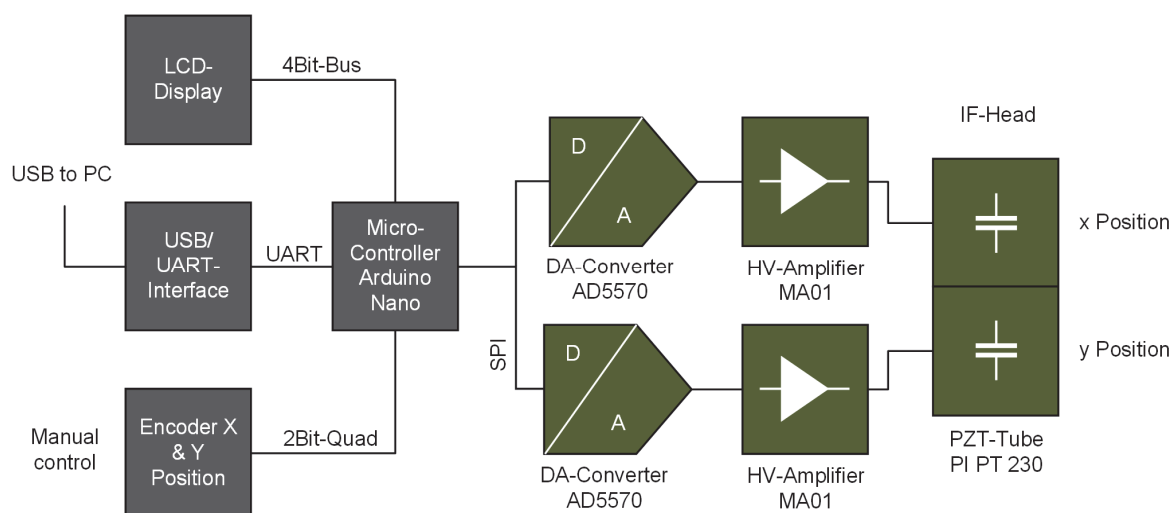


Figure 2-9 Block diagram of the IF-Head-Adjust Control Commander. Two analog voltages for  $x$  and  $y$  position movement are generated by a microcontroller and amplified to high voltages. The four segmented PZT-tube houses and moves the IF-head optics respectively the laser beam to align it to the reflective surface of the cantilever.

Drift and noise of the generated high-voltages results to an additional error in movement of 3 nm at the tube end after 4 h, confirmed by interferometric measurements (Double-Beam Plane-Mirror Interferometer SP2000D / SIOS Corp.) on an active anti-vibration table (micro 40® / Halcyonics Corp.).

Table 2-2 Datasheet AFM-Scanner and Servo-Controller

AFM-Scanner	PI PicoCube® P-363K028
Closed-loop controlled	Capacitive sensors
Scan range	5 $\mu\text{m}$ x 5 $\mu\text{m}$ x 5 $\mu\text{m}$ in closed-loop
Resolution	50 pm
Repeatability	1 nm
Resonant frequency X and Y	3.1 kHz (unloaded), 1.5 kHz (20 g load)
Resonant frequency Z	9.8 kHz (unloaded)
Operating environment	Vacuum

---

<i>Servo-Controller</i>	<i>PI E-712K063</i>
Sampling rate, servo control	50 kHz
Sampling rate, sensor	50 kHz
Sensor resolution	18 Bit (interpolated 20 Bit)
DAC resolution	20 Bit

---

---

The presented combined Scanning Force Microscope inside an SEM represents the basis for a SMM-in-SEM. Its functionality and designed components can be found in the chapter 4, after a few basics.

## 2.2.2 Validation of a Laser Interferometer-based AFM-in-SEM

A standard procedure for calibrating the z-axis is the use of a grating, like the TGZ2 from NT-MDT Corp. Every 3  $\mu\text{m}$  it has repeating height increments of 110 nm. Figure 2-10 shows it as a not true to scale drawing. In the SEM micrograph on the right, imperfect edges are visible. Furthermore, the height step is slightly wider (1.6  $\mu\text{m}$ ) than the trench (1.4  $\mu\text{m}$ ). Therefore it is evident that even calibration standards need to be checked by another microscope modality, if they are not traceable certified by a standardization institute.

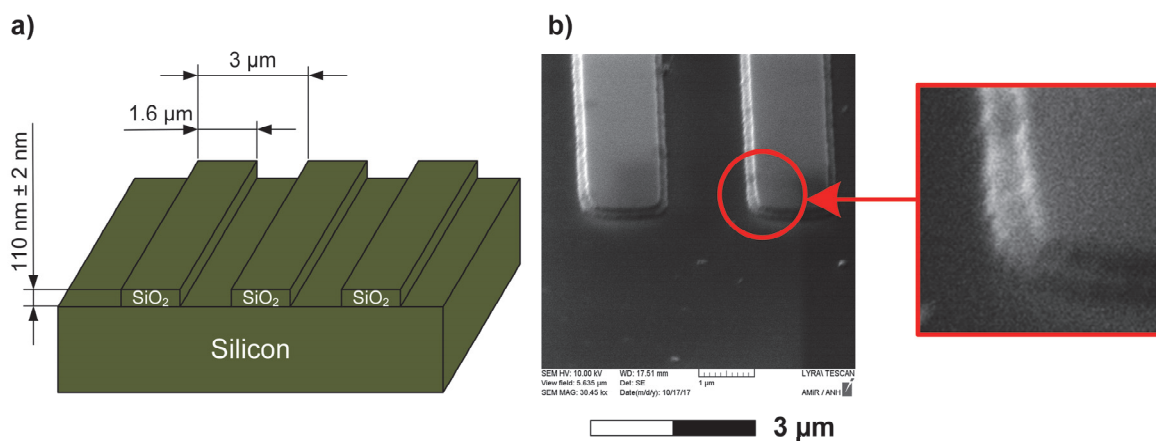


Figure 2-10 AFM test grating TGZ2 (NT-MDT Corp.) 110 nm  $\pm$  2 nm steps made of SiO<sub>2</sub>. a) Drawing and b) SEM micrograph with a zoomed detail. While the pitch is correct, the edges are not 90 deg as stated by the manufacturer.

For the calibration, in this case, the height of 110 nm taken from the data sheet is assumed. Due to the high depth of focus of SEM, it is not possible to precisely determine this parameter with nanometer resolution, with such an instrument, as is common in light microscopy. The AFM operated in contact mode under high vacuum conditions ( $7 \cdot 10^{-6}$  mbar). Figure 2-11 shows the measurement result of a scan, spread over 256 pixel \* 256 pixel, with the near-field microwave probe over a range of 5  $\mu\text{m}$  \* 5  $\mu\text{m}$ , using exclusively the atomic force and not the microwave mode. The data was manipulated by SPM software Gwyddion (developed by Czech Metrology Institute) as follows: Median of differences and plane correction.

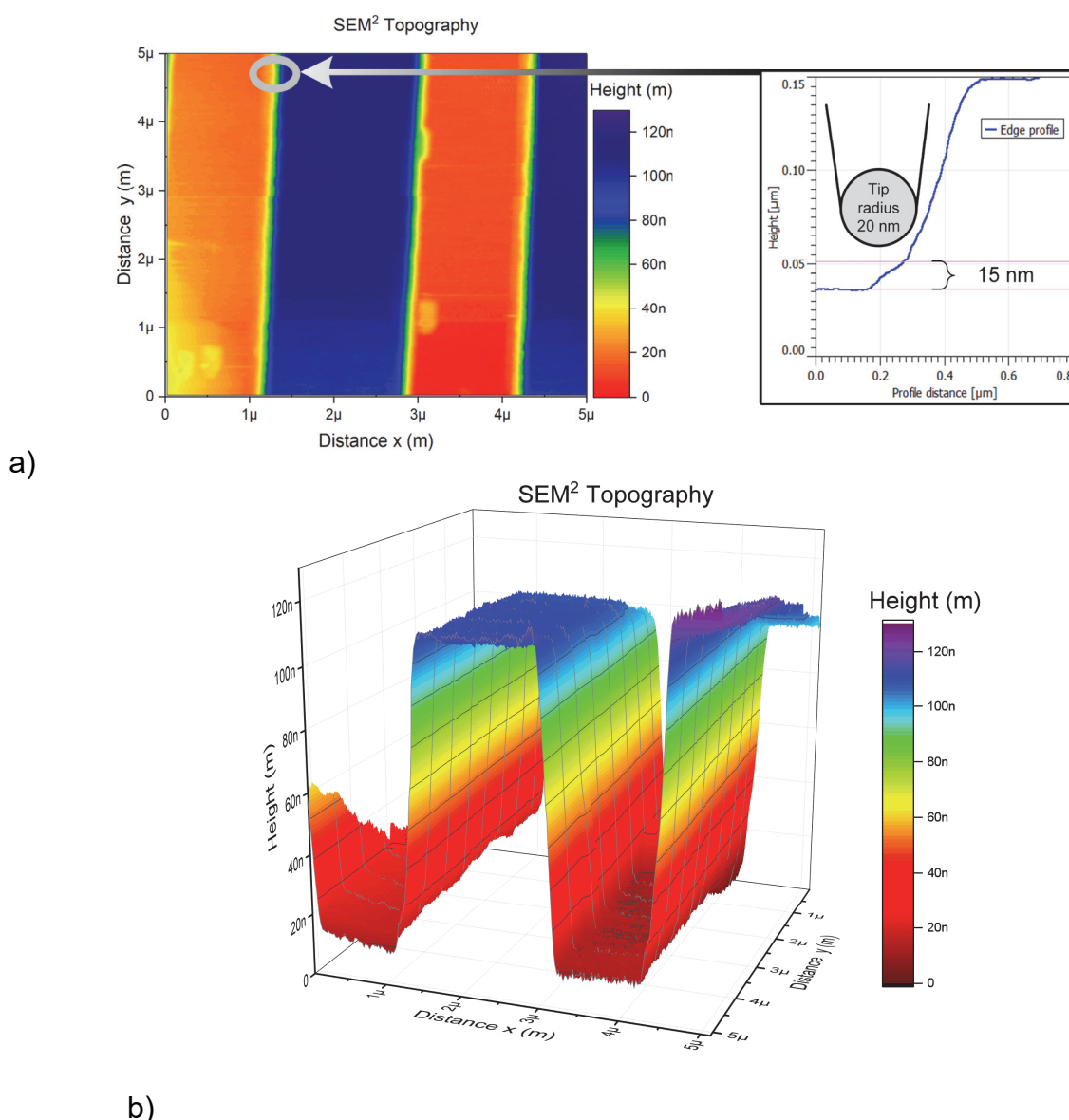


Figure 2-11 Resolution testing by using AFM test grating TGZ2 (NT-MDT Corp.) SiO<sub>2</sub> 110 nm ± 2 nm steps on a silicon substrate. a) Topography. Right: Height profile of an edge and b) 3D topography view recorded with SEM<sup>2</sup>. Data manipulation: Median of differences and plane correction.

While the 110 nm steps are well resolved, the transition from silicon to silicon dioxide, measured to be 15 nm, is not as sharp as the SEM image in Figure 2-10 indicates. This is probably due to the quality of the probe tip, which may have been slightly deformed. The tip radius is specified by the manufacturer with 20 nm and is schematically drawn to scale in the right upper image. The thermomechanical noise detection of one cantilever beam resonance

frequency in vacuum of a RMN 25Pt300A was measured to be 16.074 kHz with an amplitude of 195 pm (RMS) and at air 27 pm (RMS).

Moreover, the quality factor  $Q$  of a RMN 25Pt400B cantilever, with a resonance frequency according to the manufacturer's data sheet of  $10 \text{ kHz} \pm 30\%$ , was determined in air and under vacuum conditions ( $2 \cdot 10^{-4} \text{ mBar}$ ) (Figure 2-12). The resonance frequency was determined to

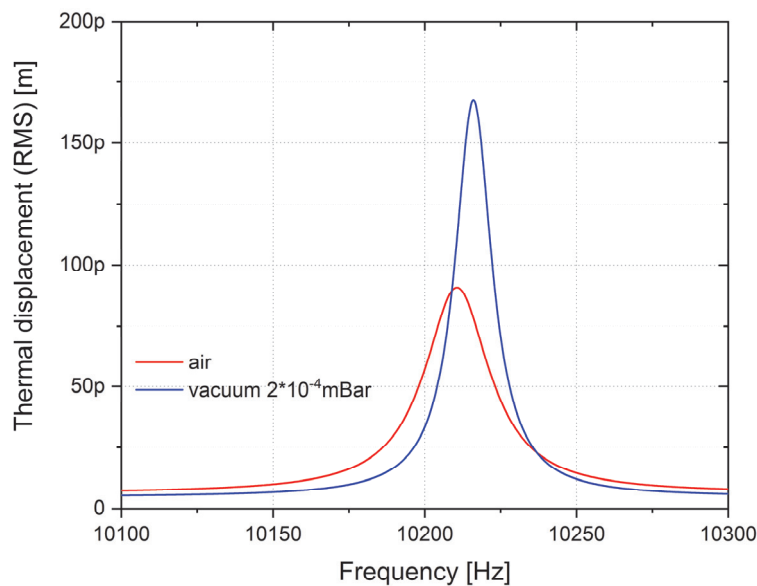


Figure 2-12 Thermomechanical noise displacement measurement of a RMN 25Pt400A cantilever in vacuum at  $2 \cdot 10^{-4} \text{ mBar}$  in SEM<sup>2</sup> (blue) and at air (red) which leads to a higher damping of the thermal noise oscillation. The curves shows Lorentz fitted results.

be  $f_{res \text{ Air}} = 10210 \text{ kHz}$  and  $f_{res \text{ Vacuum}} = 10216 \text{ kHz}$ , respectively. The calculation of  $Q$  is based on Lorentz fits after the peak amplitudes has been squared (Théron). The quality factor results, at an amplitude of 91 pm RMS in air, to  $Q_{Air} = 1009$ , while in vacuum, at an amplitude of 166 pm RMS, it calculates to  $Q_{Vacuum} = 1607$ . With the knowledge of these values and the material properties of the cantilever beam, it is possible to carry out quantitative spectroscopic force-distance measurements.

## 2.3 Scanning Microwave Microscopy

The Scanning Microwave Microscope, a relatively young member of the Scanning Probe Microscopy family, is introduced in the following subchapter and it features two versions of probe heads for this type of microscopy.

By the combination of a Scanning Tunnel Microscope (STM) with a microwave resonator (Michel et al. 1992), Scanning Microwave Microscopy has been evolved to commercially available technique, after the initial idea published by E.H. Synge (Synge 1928) and after Ash & Nicholls developed the first scanning near-field microwave microscope (Ash, Nicholls 1972). Such microscopy mode at air is more and more settling in the field of characterizing complex electric properties of different nanomaterials (Imtiaz et al. 2014b; Anlage et al. 2001). This exclusive type of SPM is able to image and quantify local dielectric and conductivity measurements in the range of 1 to 60 GHz (Chusseau et al. 2016) and even MEMS fabricated SMM systems are reported (Azizi et al. 2013).

SMM bridges the spectral frequency gap between SPM measuring with DC or low frequency currents on one side and terahertz STM (Cocker et al. 2013) respectively Near-field Scanning Optical Microscopes (NSOM) (Kalinin, Gruverman 2007; Anlage et al. 2001) on the other side (see Figure 2-13).



Figure 2-13 Frequency spectrum of Scanning Probe Microscopy (SPM). Scanning Microwave Microscopy fills the gap between Scanning Capacitance (SCM) and THz-Scanning Tunnel microscopy (THz-STM)..

An SMM consists of two units: An Atomic Force Microscope (AFM) (Karbassi et al. 2008) or Scanning Tunnel Microscope (STM) (Imtiaz, Anlage 2003; Farina et al. 2011b) and a microwave source with a gain-phase detection unit, often a Vector Network Analyzer (VNA). The conductive probe is electrical connected to one port of such a VNA. The basic schematic of a scanning microwave microscope shows Figure 2-14. A Vector Network Analyzer is generally be used as both the microwave (RF) source and the receiving detector with an internal wave splitting device, the directional coupler. The power generated in the RF source (“transmitted EM wave”, red arrow) transmits via the probe (in green) to the sample (in blue) as an incident evanescent reference wave  $a_1$ . Most of the energy reflects back (“reflected EM wave”, blue arrow) to the RF detector as reflected wave  $b_1$ , because the magnitude of the complex reflection coefficient is close to unity. The electromagnetic interaction of the scanning probe with the sample is recorded by measuring the complex reflection coefficient, while a scanning positioning stage is moving (“XYZ Scanner”, grey). A feedback control loop regulates the height during the scan movement. Two types of sensorial information for the feedback height control are common in SMM, atomic forces or tunnel currents.

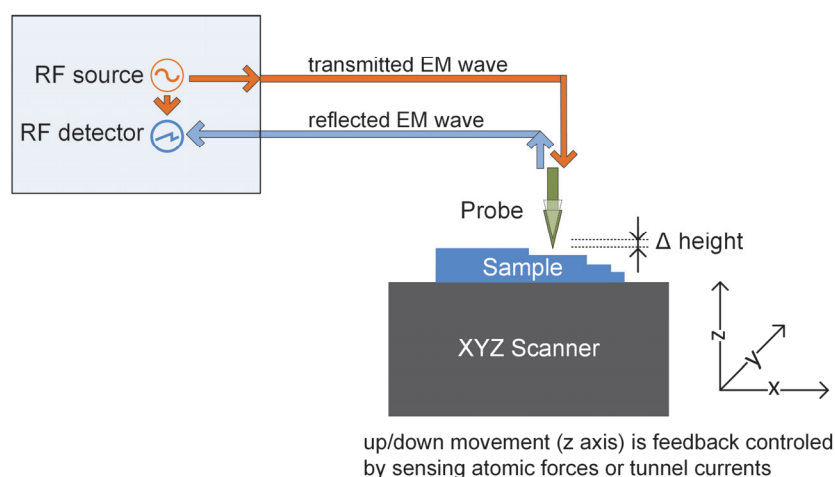


*Figure 2-14 Principle schematic of a Scanning Microwave Microscope. A feedback control process regulates the height  $z$ , while moving the sample in  $x$  and  $y$  by a scanner. An RF detector records the difference in magnitude and in phase caused by the probe-sample interaction in relation to the reference source.*

Due to the probes impedance it is very difficult to obtain accurate data for complex voltages and currents at high frequencies. That is why scattering parameters were developed. This microwave method based on well-characterized electromagnetic waves  $a_1$ , in terms of fixed frequency, power, voltage  $V_0$  and input impedance  $Z_0$  at the source of port 1. This energy is incident (orange in Figure 2-15) on a Device- or Sample-Under-Test (inset Figure 2-15) connected between port 1 and 2. The interaction of the incident waves on port 1 with the DUT, result in transmitted (green at port 2) and reflected (blue at port 1) waves. The differences in amplitude and phase are detected to investigate the electromagnetic properties of the sample.

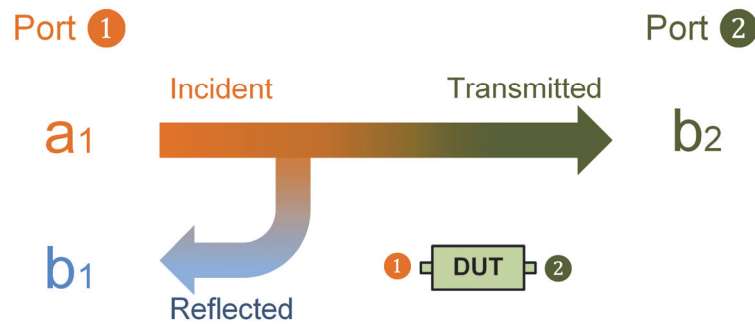


Figure 2-15 Scattering Parameter of a two-port Device Under Test (DUT) with a precisely matched load on port 2.

The reflected signal labeled  $S_{11}$  is also called Forward Reflection Coefficient, while the transmitted signal  $S_{21}$  is called Forward Transmission Coefficient or Forward Gain. Under the premises that the DUT is connected to a perfect matched real load  $Z_{Load\ Port\ 2}$  at port 2, the following applies:

$$S_{11} = \frac{\text{reflected power wave}}{\text{incident power wave}} = \left. \frac{b_1}{a_1} \right|_{a_2=0}$$

(Eq. 2-4)

$$S_{21} = \frac{\text{transmitted power wave}}{\text{incident power wave}} = \frac{b_2}{a_1} \Big|_{a_2=0}$$

(Eq. 2-5)

$$\text{with incident power wave } a_i = \frac{V_{\text{incident Port } i} + I_{\text{incident Port } i} * Z_{\text{Load Port } i}}{2 * \sqrt{\text{Re}\{Z_{\text{Load Port } i}\}}} \quad (i = 1, 2, \dots n)$$

(Eq. 2-6)

$$\text{and reflected power wave } b_i = \frac{V_{\text{incident Port } i} - I_{\text{incident Port } i} * Z_{\text{Load Port } i}^*}{2 * \sqrt{\text{Re}\{Z_{\text{Load Port } i}\}}} \quad (i = 1, 2, \dots n)$$

(Eq. 2-7)

where  $Z_{\text{Load Port } i}^*$  is the complex conjugate of  $Z_{\text{Load Port } i}$  (Marks, Williams 1992).

In SMM, one- and two-port S-Parameters are measured depending on the type of signal treatment, such as mixing processes or microwave interferometry.

The topography of the sample is measured simultaneously by employing distance-following mechanisms. In case of an AFM, the cantilever deflection, caused by atomic-scaled force interaction at the tip-sample junction, or in case of an STM, the tunneling current, is recorded synchronously to the electromagnetic information obtained by a VNA. In AFM, the cantilever height is adjusted by AFM feedback control, which for instance consists of a laser and a photodiode (light red blocks in Figure 2-16) that controls this mechanism by laser beam-bouncing. The distance control follows the sample topography, while either being in soft contact involving very light force in the order of a few nanonewtons or at constant height a few nanometers above the sample. In this way, the sample is studied non-destructively, while maintaining a spatial resolution in the order of few nanometers.

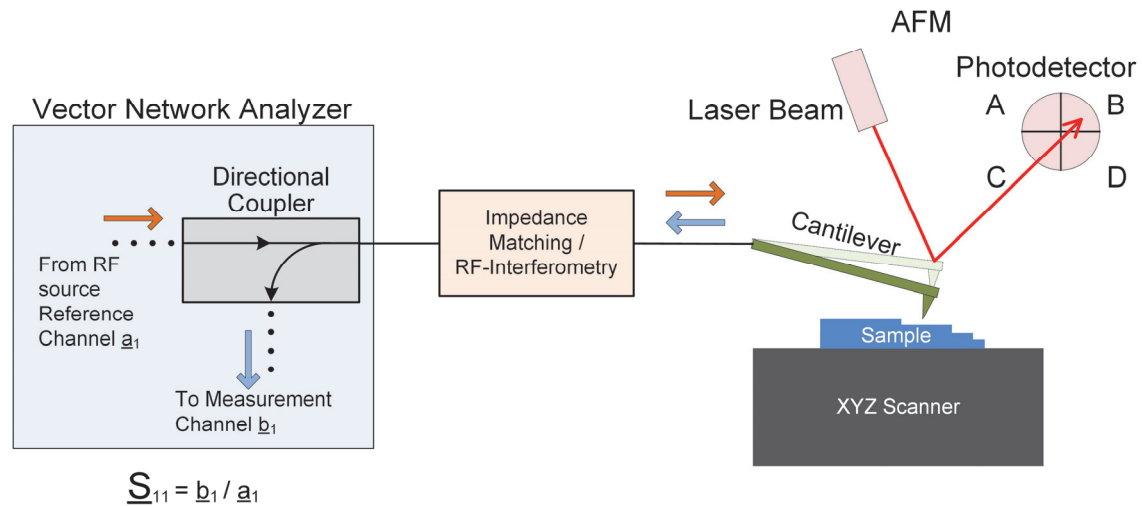


Figure 2-16 Basic parts of a Scanning Microwave Microscope, here based on a laser deflection AFM (light red) probing a sample via a conductive cantilever (green). Figure modified from reference (Haenssler 2014).

Between the VNA and the probe tip, a distributed resonating circuitry is often established. It can enhance the sensitivity at a single frequency by reducing the mismatch of the system impedance to the SUT impedance. Radio frequency or microwave interferometry is another approach to measure over a wide broad frequency range and is explained later on in chapter 3.

In the next chapter a literature overview about fields in which SMM techniques have been applied to both qualitative and quantitative studies can be found.

### 2.3.1 Areas of SMM Applications

The main research targets of SMM are the characterization of hetero-structured devices here mostly in semiconductor research and growingly in cell biology. An overview of reported applications, divided into imaging and quantitative studies alongside topography imaging, follows.

*Table 2-3 Reported targeting applications of SMM*


---



---

*Thin film imaging*

---

1-layer to 3-layer Graphene (Tselev et al. 2012; Fabiani et al. 2011), 1-layer hexagonal boron nitride (“white graphene”) (Anderson 2013)

Chromium on glass substrate (Kim et al. 2003; Steinhauer, D. E. et al. 1997)

Boron-doped silicon (Imtiaz et al. 2007; Imtiaz, Anlage 2003)

Vanadium dioxide (VO<sub>2</sub>) and chemical-vapor-deposition graphene (Tselev et al. 2013)

Phosphorus ions implanted into p-type silicon substrate (Lai et al. 2008)

Multilayer ferrite on glass substrate (Xing et al. 2012)

Transition metal dichalcogenide monolayers (TMD) (Berweger et al. 2015)

Organic self-assembled monolayers of alkane-thiols (Wu, Yu 2010)

Yttrium iron garnet (YIG) magnetic films (Joseph et al. 2016)

---

*Nanowire imaging*

---

In<sub>2</sub>Se<sub>3</sub> nanoribbons (Lai et al. 2009)

GaN nanowires (Berweger et al. 2016)

---

*Biological cell imaging*

---

Human monocytic leukemia cells (THP1) on gold and glass substrates (Oh et al. 2011)

Epidermal cells of *Yucca filamentosa* (Park et al. 2005)

C2C12-Myoblast cells (muscle cells) interacting with multi-wall carbon nanotubes (Farina et al. 2012)

Escherichia coli cells (Biagi et al. 2016)

Yeast cells behind a membrane (Tselev et al. 2016)

---

*3D-Material imaging*

---

Buried metal structures (Plassard et al. 2011), Metal-insulator-semiconductor systems (Lai et al. 2009; Smoliner et al. 2010) and single phosphorous layer (Gramse et al. 2017)

Coal (Tselev et al. 2014)

---

---

*Quantitative Measurements*

---

Nanoscaled capacitances (Dargent et al. 2013; Gramse et al. 2014) and interconnects (Talanov, Schwartz 2009) in the sub-fF range

Dopant concentrations in n-type Si (Torigoe et al. 2012), p-type Si (Imtiaz et al. 2012) and Si p-n junctions (Brinciotti et al. 2016)

Permittivity of dielectric materials (C. Gao and X.-D. Xiang 1998; Karbassi et al. 2008) and polar liquids (Gregory et al. 2016)

Conductivity of superconductors  $\text{YBa}_2\text{Cu}_3\text{O}_{7-d}$  (Kleismit et al. 2006), Niobium-based thin films (Tai et al. 2013) and hematite and calcite minerals (Monti et al. 2016)

---

This compilation presents works conducted by SMM in standard non-vacuum laboratory environment. The mentioned work on superconductors (Kleismit et al. 2006) used an STM-assisted SMM in a cryogenic environment.

### **2.3.2 Near-field probes**

With conductive cantilevers it is possible to induce localized broadband electromagnetic waves into the probe-sample-interface. At the same time, force feedback methods are utilized to scan the sample very closely to the surface to increase the near-field resolution. The probe itself must be adapted in such a way that the fringing fields concentrating as narrow as possible at the tip end and thus confines the interaction area. The reflected wave must then reach the receiver as loss-free as possible.

A very interesting approach is the use of coaxially shielded probe tips to reduce parasitic capacitive influences (van der Weide, D. W. 1997; Yang et al. 2012). A variant with integrated piezoresistive force feedback was published (Yang et al. 2012). The problems here, these cantilever probes are either only produced at research institutes or by one company (Primenano Corp.). The highest cut-off frequency with such probes are found to be 10 GHz (Wu et al. 2017).

In this thesis the goal is to optimize commercial free available probes on the basis of available techniques in order to use them in a technology demonstrator.

By using 3D electromagnetic finite element analysis software, the near-field distributions and the transmission line connecting the probe can be analyzed and optimized. A first usage in the area of microwave microscopy, is a 3D analysis of a near-field probe consisting of a narrow slot into a thin endwall of a metallic waveguide of resonant length (Golosovsky et al. 2002). A full-wave FEM Analysis of a platinum AFM cantilever-tip-sample system is introduced by Oladipo et al (Oladipo et al. 2013). They found out that with this kind of analysis, it was possible to quantify the stray capacitances and to separate them originating from the cantilever or the cone tip.

However, the entire system, from at least the connector to the tip, influences the electromagnetic measuring system, too. In the following, the development steps for the construction of two near-field probes are described. One finds use in SEM<sup>2</sup>, while the other finds use in a second setup with a different AFM configuration and emphasizing higher frequencies. The basis for both designs is 3D FEM analysis of the entire path, from plug via the cantilever ceramic substrate to the tip. Advantageous against the water meniscus, which reduces the resolution of the near-field due to its high permittivity, is the use in the vacuum chamber of the SEM. Both probes are incorporating a commercial cantilever probe from Rocky Mountain Nanotechnology Corp. (RMN).

## Near-field microwave probe

The conductive probing AFM tip (25Pt300 / RMN Corp.) acts as a microstrip transmission line and at its end as an electrically small antenna, radiating non-propagating evanescent fields. This cantilever is the same as used in a commercial SMM from Keysight Corp. and features a spring constant of nominal 18 N/m. The characteristic impedance, under the assumption that the bottom of the ceramic substrate has ground layer, calculates to 74  $\Omega$ . In interaction with the sample, the field distribution changes, under the assumption that the tip-sample distance and the tip radii are much smaller than the wavelength  $\lambda$  of the incident microwave. The interface between the cantilever substrate and the wiring to the VNA is a critical wave path, also in terms of transmission losses. To match the impedance of 74  $\Omega$  of the grounded cantilever substrate, acting as a microstrip transmission line, a coplanar waveguide structure was designed (RO4003C® / Rogers Corp.) for this waveguide transition (see Figure 2-17). Electromagnetic simulations (HFSS® / Ansoft Corp.) optimized the transmission and return losses in the frequency range 1 to 10 GHz of the near-field microwave probe from the entrance of the low insertion force RF-connector (SMP) to the end of the conductive line on top of the ceramics of the 25Pt300 probe. The free-standing 300  $\mu\text{m}$  long end and the tip itself wasn't included in the simulations.

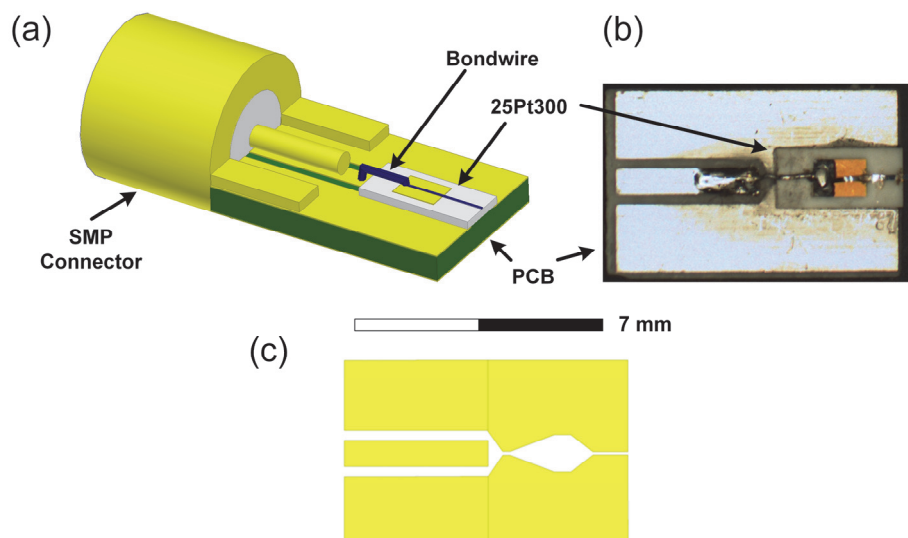


Figure 2-17 Near-field microwave probe: (a) CAD isometric view, (b) Photograph, (c) CAD view of the PCB top layer layout optimized for RMN 25Pt300 probe.

Figure 2-18 depicts that the maximum operating frequency with the commercial 25Pt300 probe turned out to be 7 GHz. Here the transmission  $S_{21}$  and return losses  $S_{11}$  becomes to maximum -0.5 dB and -12.5 dB respectively, in a 50  $\Omega$  back-to-back simulation with wave ports.

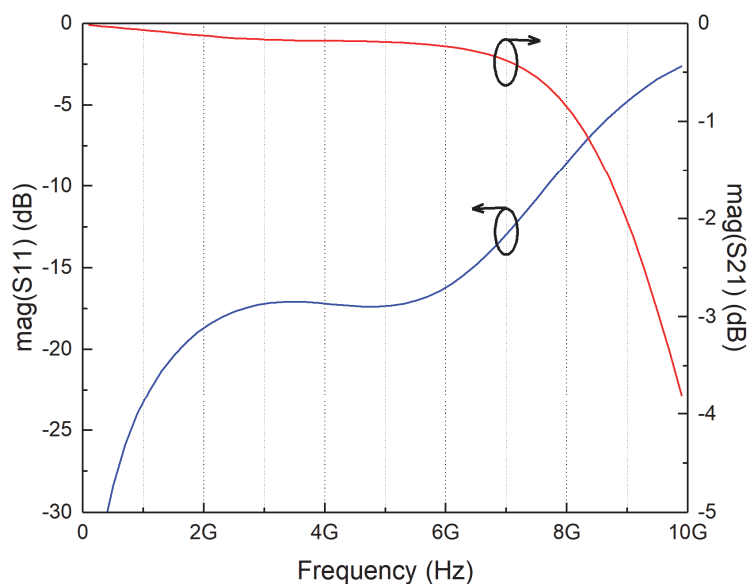


Figure 2-18 Simulation results of the Near-field microwave probe: Transmission loss  $\text{mag}(S_{21})$  (red) and Return loss  $\text{mag}(S_{11})$  (blue).

The FEM simulation with HFSS® has not only been used to optimize the wave mode transitions. Figure 2-19 shows the tip-sample region in a contact measurement of micro gold capacitors on a SiO<sub>2</sub> dielectric. Here the influence of the adjacent metallic pads on the distribution of the electric field can be seen.

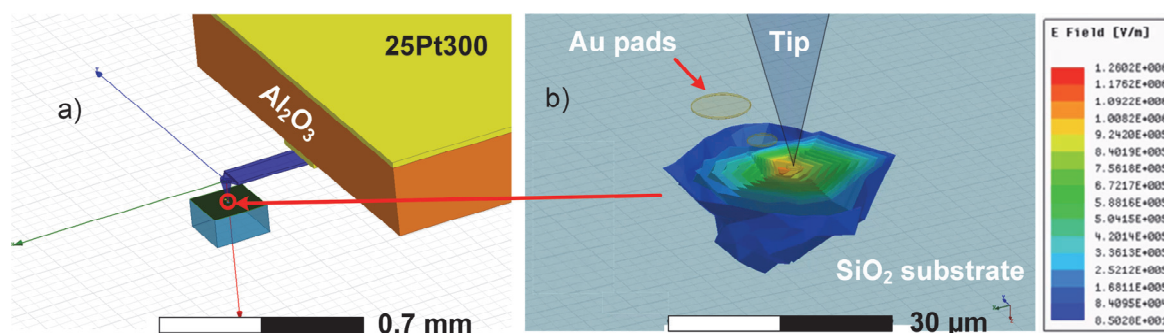


Figure 2-19 FEM RF 3D simulation of SEM<sup>2</sup> microwave probe. a) Sketch of the cantilever substrate 25Pt300 with the cantilever, the tip and a silicon dioxide sample with gold pads on top. b) Zoomed detail of the tip-sample region with electric near-field distribution inside the dielectric. Figure on the left from reference (Haenssler et al. 2017).

Another design recommendation was the ease of exchange of the near-field microwave probe in case of a broken tip. A coaxial connector and screws allows for fast replacement and locks against rotation of the probe [shown in photograph Figure 2-8 e)].

Not only the conversion of propagation modes, from coaxial to coplanar to microstrip to the radiating tip produces unwanted losses. The signal coming out of the source (VNA port), traveling over the coaxial cable and all the connections to the probe and then reflected back with the wanted information “on board” is additionally attenuated. All these insertion losses summarizes the following graph over the full length of 1.6 m based on datasheet information.

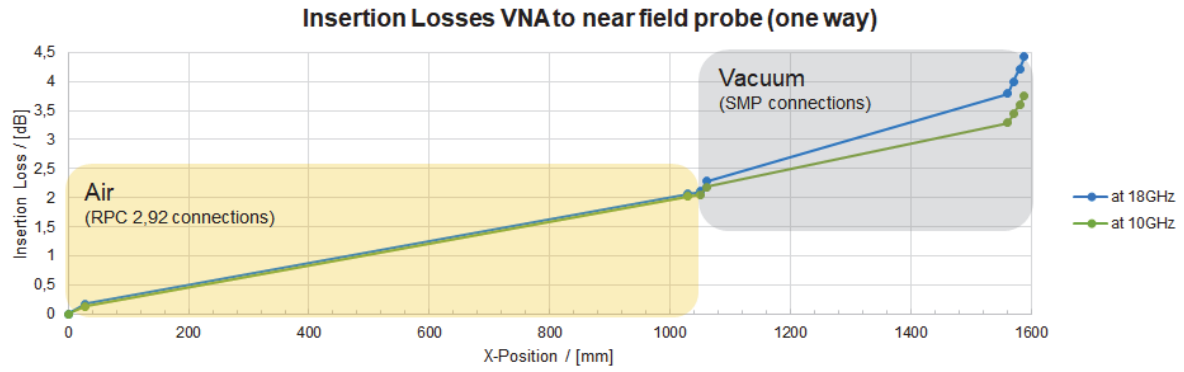


Figure 2-20 Signal attenuation over cable distance (in-line attenuation and insertion losses) for one way at two frequencies (10 GHz and 18 GHz) in SEM<sup>2</sup>.

A two-way attenuation of minimum 7 dB in the operating frequency range of the SEM<sup>2</sup> is expected. With a Short-Open-Load calibration of the VNA, which can be executed by using the integrated calibration kit mounted in the chamber door, maximum 5 dB can be canceled.

## Near-field millimeter-wave probe

In the framework of French national project EQPX ExCELSiOR, a second instrumental setup of an SMM in vacuum is currently under construction. The topography measurement is also controlled through an AFM modality, but based on the laser-deflection principle with a four quadrant photodiode (Haddadi et al. 2017). Due to the constantly increasing demand for higher bandwidth, a probe is to be developed here as well, which ought to reach 50 GHz or higher as one design goal. The mm-wave probe shall have the following characteristics in addition to the higher bandwidth of the previous probe: Rocky Mountain Nanotechnology cantilever as probe tip, transmission losses better 3 dB and easily replaceable for tip exchange. The use of a special type of PCB mount connector, which is connected to the PCB board by a clamping mechanism, ensures frequent replacement without soldering. The used connector (08K80A-40ML5 / Rosenberger Corp.) is specified for up to 40 GHz with return loss better than 19 dB according to data sheet. The optimization process of the millimeter-wave mode conversion PCB (RT3010® laminate / Rogers Corp.), was done by means of simulation, such in a way as described in the chapter before. In this part of the work a modified version of the 25Pt300 cantilever came in use. The ceramic substrate is covered with a ground plane made of gold and the platinum cantilever strip, is attached on a 220  $\mu\text{m}$  wide Au layer. Through this modification the impedance of the cantilever substrate is optimized to 50  $\Omega$ . Best practices methods have been applied, to ensure the placement of the vias in 125  $\mu\text{m}$  distance, if frequencies greater than 100 GHz are used (Zhou, Melde 2008). The FEM optimization process (Figure 2-21) yielded transmission losses  $\text{mag}(S_{21})$  of 1 dB up to 50 GHz, which have to be doubled, as these are reflection measurements and the wave returns back. The return losses  $\text{mag}(S_{11})$  shall be acceptable, but are best below 40 GHz.

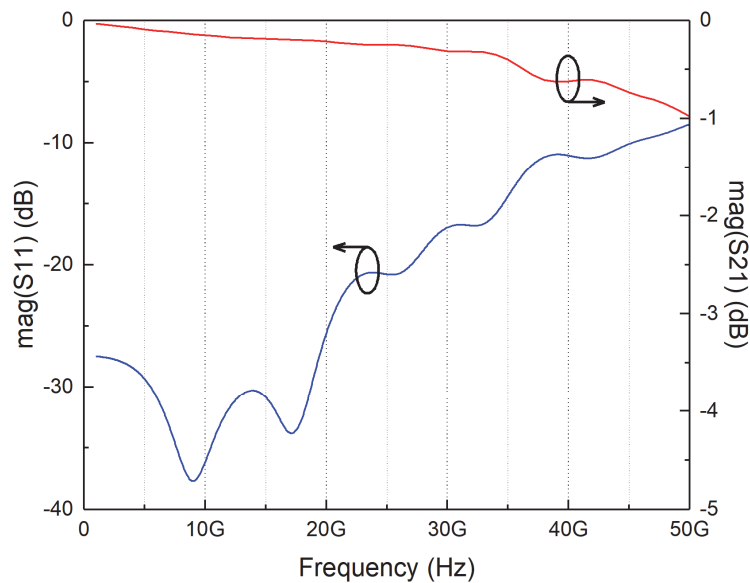


Figure 2-21 Simulation results of the Near-field millimeter-wave probe: Transmission loss  $\text{mag}(S_{21})$  (red) and Return loss  $\text{mag}(S_{11})$  (blue).

Looking to the influence of bondwires in coplanar waveguide structures, it is known that flat ribbons enhances the propagation significantly (Sutono et al. 2001; Lim et al. 2005). Hence, it was used in the manufacturing process of the mm-wave probe, by fixating gold ribbon wire with conductive glue (Type 205 / Epotek Corp.). The following Figure 2-22 shows the near-field millimeter-wave probe. Figure 2-22 a) depicts an isometric drawing of the probe, which consists of the connector, the PCB with the immersed cantilever substrate (in orange). Due to diversity issues in the SEM (Mira® / Tescan Corp.) at IEMN, several types of mode transition PCB's were manufactured and two designs are shown in the photograph: A grounded coplanar waveguide (CPWG, Design C long) over the whole length until the cantilever substrate and a CPWG converting to microstrip mode (Design B long) shown in Figure 2-22 b). Measurements were done with an Agilent PNA E8364B with an IF-Bandwidth of 100 Hz and 801 numbers of points over the range 10 MHz to 50 GHz in a back-to-back configuration, seen in the photograph inset in Figure 2-23 c).

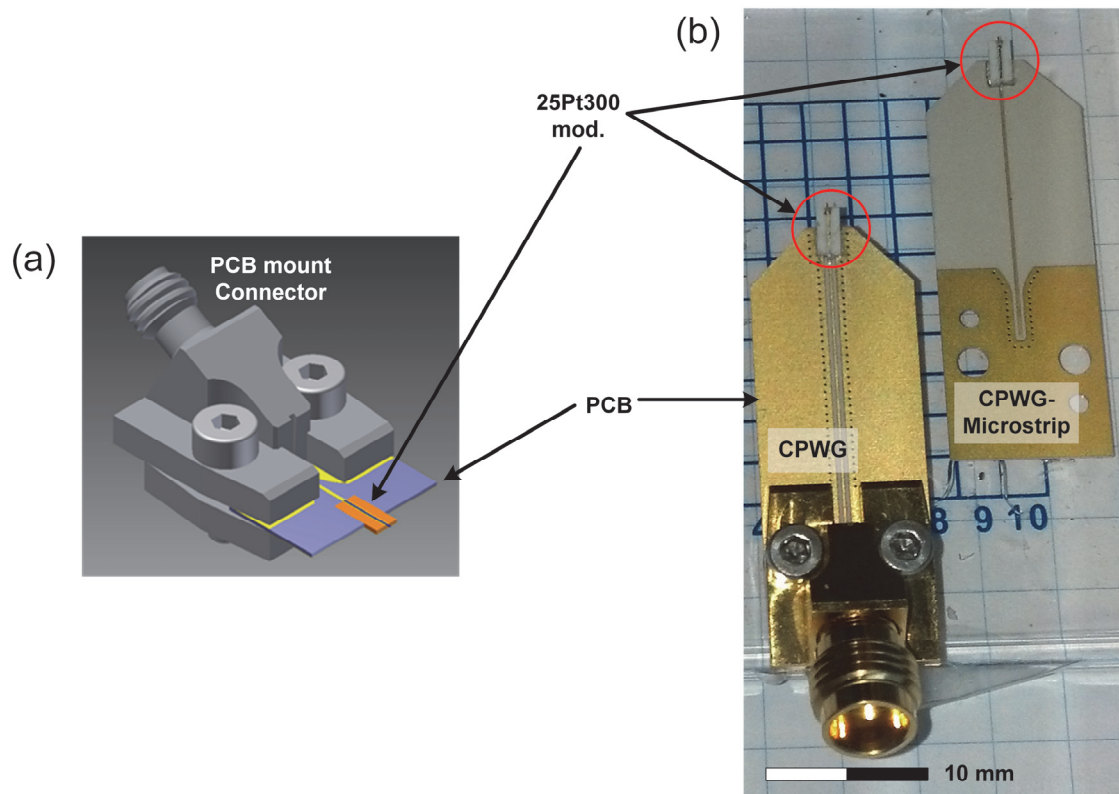
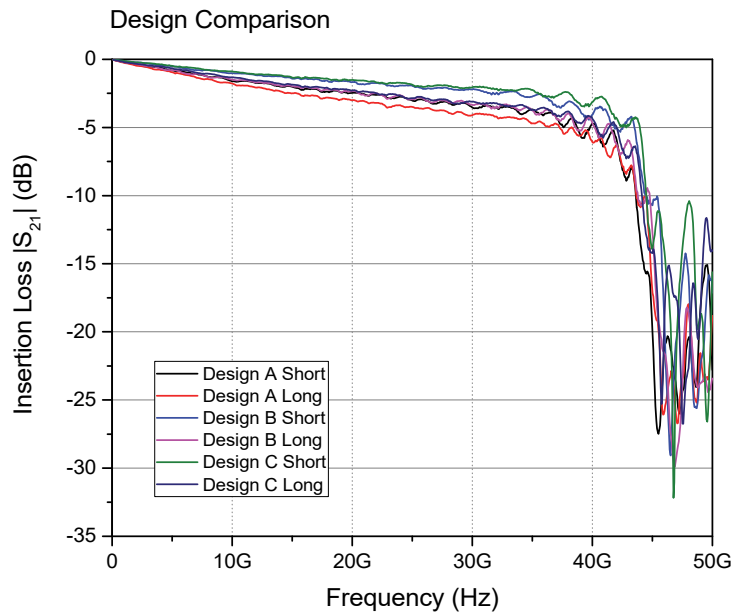
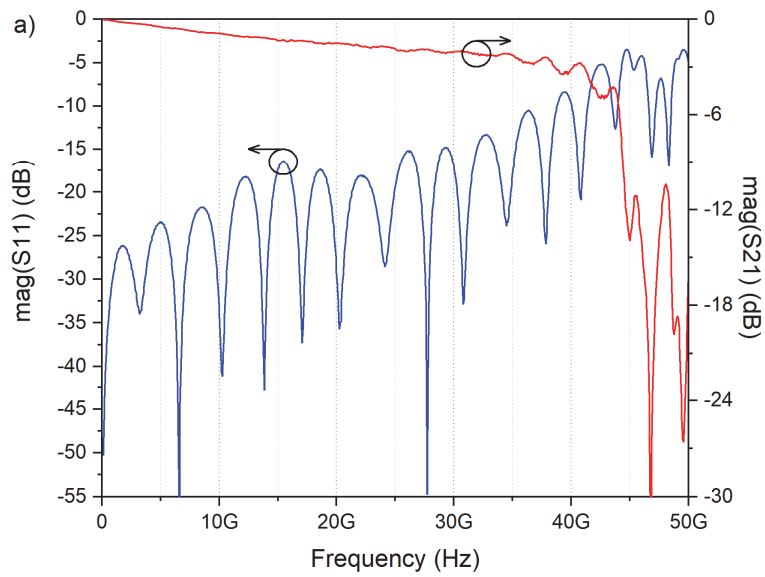
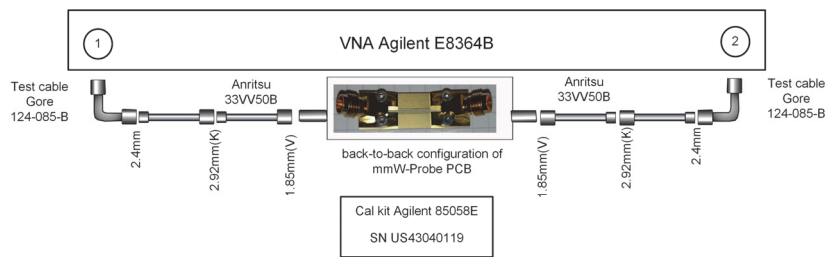


Figure 2-22 Near-field millimeter-wave probe: a) CAD sketch and b) Photo. Left: A grounded coplanar wave guide (CPWG) transition until the cantilever substrate. Right: A CPWG-to-microstrip mode conversion up to the RMN 25Pt300 probe. Image left from reference (Haddadi et al. 2017).

The tipholder PCB with a CPWG structure over the whole length (“Design C” in Figure 2-23 b)) shows the best performance. Up to 40 GHz, the transmission losses  $\text{mag}(S_{21})$  are minimal 3 dB in this measurement configuration [Figure 2-23 c)]. Reciprocity tests with design C short resulted in maximum 0.2 dB up to 40 GHz.



b)



c)

Figure 2-23 Testing of the near-field millimeter wave probe PCB in a mirrored configuration. a) Return losses  $\text{mag}(S_{11})$  (blue) and insertion losses  $\text{mag}(S_{21})$  (red) of the CPWG version (Design C). b) Comparison of transmission losses of six designs. c) Measurement setup showing all connections adapting to the probe PCB.

The following special features in difference to the simulated data stand out: The deep notch at around 47 GHz in the transmission coefficient. At the coupling point of the PCB mount connector and the PCB, the transition is not designed smoothly. Resulting in a staircase transition which in turn causes a wave discontinuity. This has been verified by another FEM high frequency analysis. The second feature seen in the comparison are the repeating ripples in the reflection coefficient. Since the two wave transitions aren't perfect the PCB acts as a resonator. In a second test configuration, the millimeter-wave probe was fitted and bonded with the cantilever substrate and the reflection coefficient  $\text{mag}(S_{11})$  was measured in air. As it can be seen in the Figure 2-24 a) below, three resonance dips are visible at 7.7 GHz, 23.1 GHz and 37.8 GHz. While the cantilever beam itself is resonating on 23.1 GHz, the 37.8 GHz resonance might originate from the impedance mismatch introduced by the “unsmooth” transition at the junction mount connector to PCB and/or by the transition PCB-cantilever ceramics. The third resonance at 7.7 GHz is caused by PCB itself. By transforming the measurements into the time domain (Figure 2-24 b) ), the peaks caused by this resonator can be made more easily visible as they repeating every  $t = 0.44$  ns. The length of the PCB resonator  $l_{res}$  is determined by

$$l_{Res} = \frac{v * t}{2} = \frac{c_0 * t}{2 * \sqrt{\epsilon_{r \text{ effective}}}} = \frac{3 * 10^8 \frac{m}{s} * 0.44 * 10^{-9} s}{2 * \sqrt{6.04}} = 26.9 \text{ mm}$$

(Eq. 2-8)

where  $c_0$  refers to the speed of light,  $\epsilon_{r \text{ effective}}$  to the effective permittivity of the CPWG structure fabricated out of RO3010® substrate with  $\epsilon_r = 10.2$ ,  $v$  to the reduced speed of the waves inside the media and  $t$  to the time of the oscillating signal.

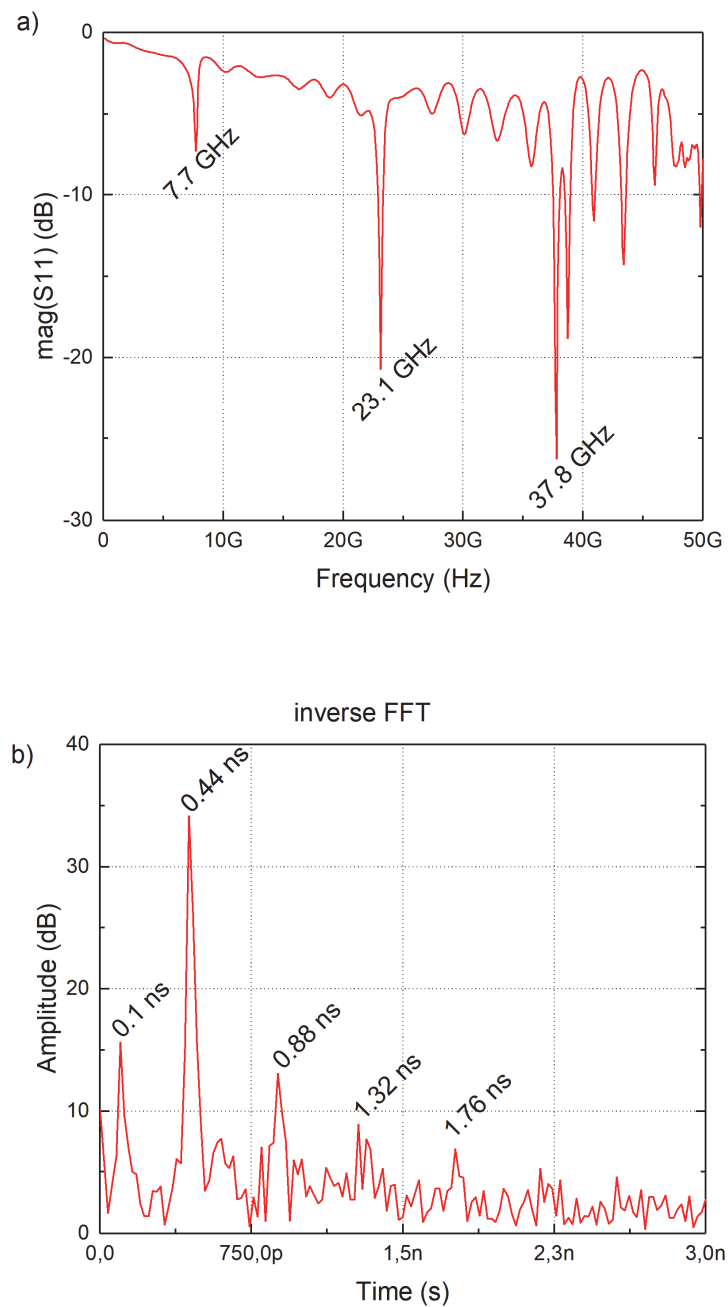


Figure 2-24 Measurement of the near-field millimeter wave probe in air. a) Return loss  $\text{mag}(S_{11})$  in frequency domain b) Return loss  $\text{mag}(S_{11})$  in time domain with harmonic peaks every 0.44 ns originating from the length of the PCB.

The first peak at 0.1 ns originates in the connecting point from the Rosenberger mount connector and the probe PCB.

## 2.4 Summary

The possibilities that arise from a combination of scanning force and electron microscopy are manifold and a new compact variant based on laser interferometry has been described. It is therefore reasonable to use such advantages for research in microwave microscopy as well. These advantages not only facilitate the sample and probe navigation to the desired regions. Furthermore, a reduction of the water meniscus is to be expected due to the integration of a microwave near-field probe head into the vacuum chamber, which in turns reduces the near-field and spatial resolution. From the increasing number of studies that have emerged in the field of microwave microscopy in recent years, it can be noted that this technology is promising. However, some questions remain unanswered when it comes to quantitative interpretations of the measurand data.

The design results of two near-field probes for SMM can be summarized as follows. While the very compact probe for use at the University of Oldenburg (Germany) is limited to a maximum of 7 GHz, the second, large version for IEMN (Villeneuve d'Ascq, France) can be operated in a higher GHz regime. In regards to the mmW-near-field probe, it can be stated that, with the limitations resulting from the resonances, it can be used up to about 37 GHz. For higher frequencies an improved probe has to be created. The mm-wave PCB shall be developed on the basis of a thinner substrate, e.g. 127  $\mu\text{m}$  thick Rogers Substrate, with an enhanced wave interface.

This page left intentionally blank.

### 3 HIGH-FREQUENCY IMPEDANCES AT THE NANOSCALE

For the types of nanoelectronic samples or objects studied with an SMM, the complex S-Parameters contains information about the complex quantities of conductivity, permittivity, and permeability. Extracting this information out of the magnitude and phase information of  $S_{11}$  and  $S_{21}$  at the nanoscale is one challenge. An understanding of both the interaction of the incident electromagnetic wave and the physics of the sample is needed to obtain the quantitative data from the measurements. The impedances here are in the order of the quantum resistance  $R_{Quantum} = 25.8 \text{ k}\Omega$  (Liang et al. 2001; Kong et al. 2001).

#### 3.1 Fundamentals

Considering a nanoscaled wire, meaning the quantum wire is so small that Heisenberg's uncertainty principle of  $\Delta E * \Delta t \sim h$  apply to it, where  $\Delta E$  is change in energy,  $\Delta t$  is change in time and  $h$  is the Plank constant. The Ohm's law  $= \frac{\Delta V}{I}$ , where  $V$  is voltage and  $I$  is current, can be written for such nanowire as  $\frac{\Delta V}{e/\Delta t}$ , where  $e$  is the electronic charge. This can be rewritten as

$$R_{Quantum} = e \Delta V * \frac{\Delta t}{e^2} = \Delta E * \frac{\Delta t}{e^2} = \frac{h}{e^2} \approx 25,8k\Omega .$$

(Eq. 3-1)

Taking, for instance, a frequently used nanoobject, the so called Single Wall Carbon Nanotube (SWNT), as a high frequency transmission line over a highly conducting ground plane. The equivalent circuit diagram in Figure 3-1 displays the distributed elements in the RF region of such tube.

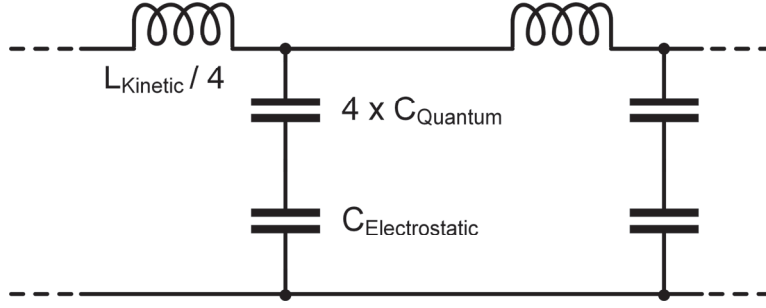


Figure 3-1 Equivalent circuit diagram for a SWNT over a ground plane with its distributed elements.  $L_{Kinetic}$  denotes the kinetic inductance,  $C_{Quantum}$  indicates the quantum capacitance, and  $C_{Electrostatic}$  is the electrostatic capacitance in this RF model. Taking spin degree of freedom for the SWNT into account, leading to four channels, a factor of 4 for  $L_{Kinetic}$  and  $C_{Quantum}$  must be introduced. Figure based on reference (Rutherglen, Burke 2009).

In the Irvine approximate approach (Burke 2002), it is stated that four parallel independent channels in a SWNT, enables the conduction. The SWNT characteristic impedance at very high frequencies becomes to

$$Z_{SWNT} = \sqrt{\frac{L_{Kinetic}}{C_{Quantum}}} \approx \frac{h}{2e^2} = 12.9 \text{ k}\Omega ,$$

(Eq. 3-2)

$$\text{with } L_{Kinetic}/\mu\text{m} = \frac{h}{2e^2 v_F} \approx 16 \text{ nH}/\mu\text{m} ,$$

(Eq. 3-3)

$$C_{Electrostatic}/\mu\text{m} \approx \frac{2\pi\epsilon}{\ln(\text{Distance to GND plane}/\text{tube diameter})} \approx 50 \text{ aF}/\mu\text{m}$$

(Eq. 3-4)

$$\text{and } C_{Quantum}/\mu\text{m} = \frac{2e^2}{h * v_F} = 100 \text{ aF}/\mu\text{m} ,$$

(Eq. 3-5)

where  $v_F = 8 * 10^5$  m/s is to the Fermi velocity of the carbon nanotube. These quantum capacitances and inductances per unit length are approximation out of the mentioned literature

and based on the four-channel-in-parallel statement. This is to indicate in which measuring ranges the targeted nanoobjects are located. A predictive plot, taken from (Burke 2002), of a real part of modeled impedance of a 100  $\mu\text{m}$  long SWNT over frequency shows Figure 3-2, assuming a DC resistance of 1  $\text{k}\Omega/\mu\text{m}$ . The height between the SWNT and the ground plane is not exactly mentioned, but given to be between 10 nm and 1  $\mu\text{m}$ . The theory on “Nanoelectromagnetism” is still under development and not part of this work, but an interesting review is found in (Rutherglen, Burke 2009).

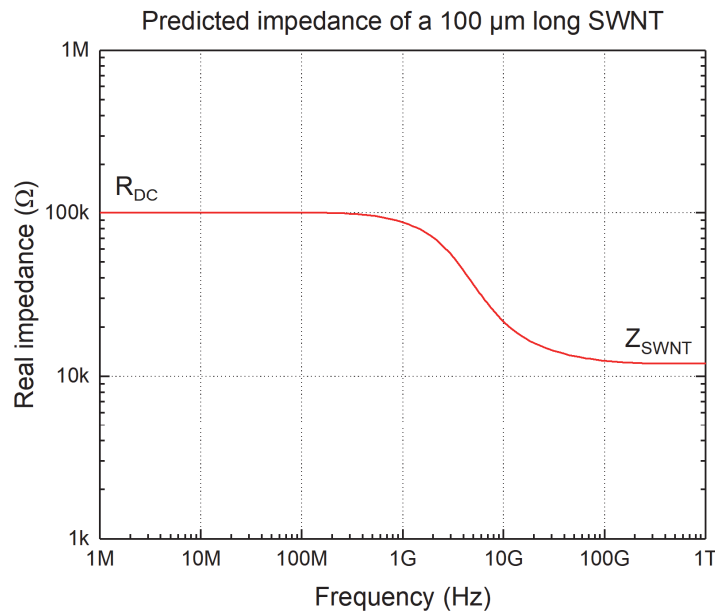


Figure 3-2 Impedance plot for a 100 $\mu\text{m}$ -long Single Wall Nanotube over a ground plane. The transition from DC to RF takes place at around 1 GHz, when the SWNT impedance is behaving more and more capacitive. Graph taken from reference (Burke 2002).

With the characteristic impedance of microwave systems and test equipment of mainly 50  $\Omega$  this brings us to another challenge on the measurement side as it can be seen in Figure 3-3 below. The reflection coefficient, normalized to 50  $\Omega$ , for the mentioned SWNT results in

$$\Gamma_{SWNT} = S_{11} = \frac{Z_X - Z_0}{Z_X + Z_0} = \frac{Z_{SWNT} - 50\Omega}{Z_{SWNT} + 50\Omega} = 0.992,$$

(Eq. 3-6)

under the assumption that  $Z_x$  is real only. This result of the high impedance of  $12.9 \text{ k}\Omega$  in regards to the reference impedance means, that less than 1% of the original incident signal must be detected precisely by the VNA. The Figure 3-3 b) indicates, that reflection coefficient measurements at one port for impedances of  $Z_x > 20 * Z_0$  are getting more and more insensitive,

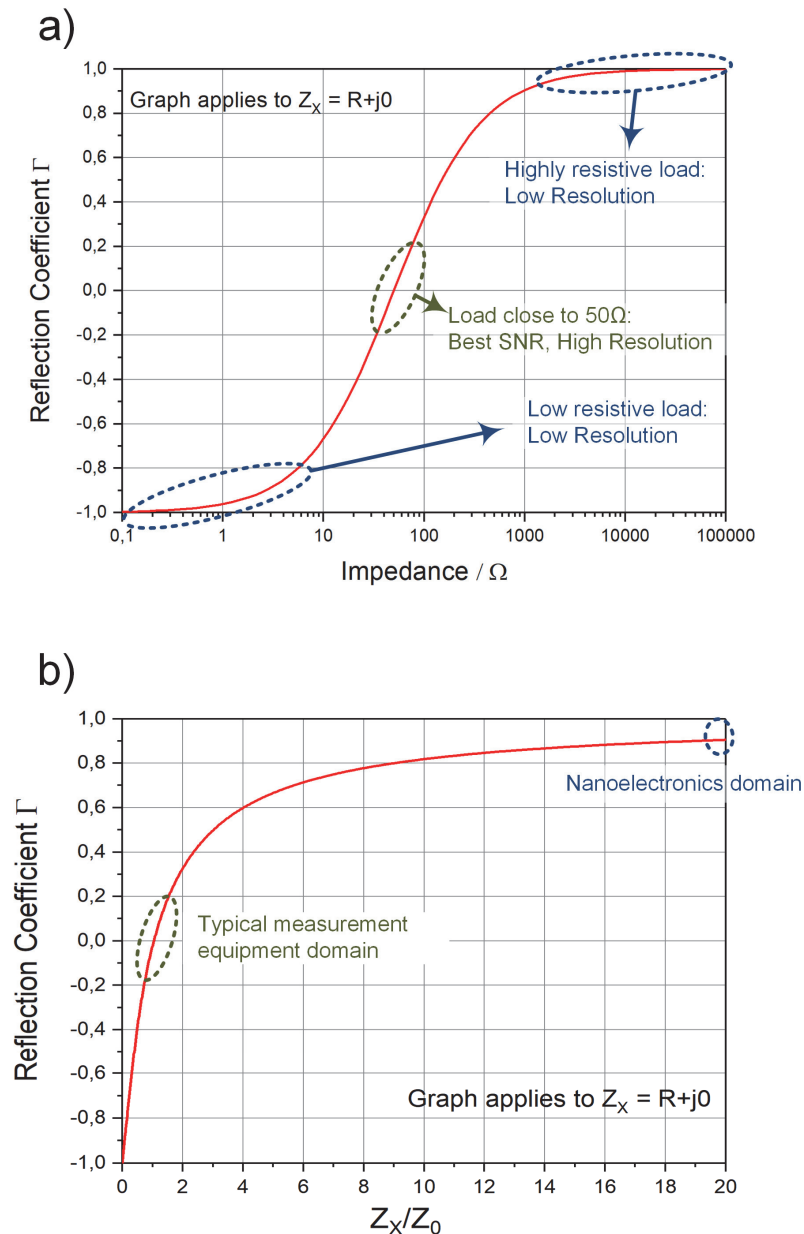


Figure 3-3 Reflection coefficient  $\Gamma = \frac{Z_x - Z_0}{Z_x + Z_0}$  for a one-port network, as a function of a) the load impedance  $Z_x$  and b) the normalized load impedance  $Z_x/Z_0$ . Under the assumption of the load impedance  $Z_x$  to be only real. The green dotted circles in both graphs marks the typical area of measurement equipment and the blue area marks the insensitive area of VNA's and the targeted nanoelectronics respectively. Image a) is inspired by reference (Happy et al. 2014).

even at substantial changes. Measurements with a Vector Network Analyzer in that range may possess worst case uncertainties of higher than 100 % (Datasheet VNA 8753ES H16 with 85033D Calibration Kit / Keysight Corp.) (Happy et al. 2014). Measuring scattering parameter of nanoelectronics and -materials with a VNA, which is a major part of a SMM, has such limited capabilities. The performance of measurements are determined by the instrument signal-to-noise ratio (SNR) and system linearity. Both sides, the microwave signal source and the receiver are limited and the equipment manufacturer defines the system dynamic range in their datasheets. The system resolution isn't high enough, measuring such high impedances at the nanoscale by the direct attempt to measure the reflection coefficient close to one. Efforts to minimizing the mismatch of the high impedance of nanodevices to the system impedance of the measurement equipment are inevitable (Happy et al. 2014). State-of-the-art methods to enhance the signal-to-noise ratio are basing on resonant or electrical interferometric techniques and from a Smith chart perspective, the measurand moves from the nearly open circuit condition at the edge closer to the middle, the characteristic impedance  $Z_0$ .

### 3.2 Interferometry in Microwave Microscopy

Matching the impedance of the sample-under-test to the measurement system at a single frequency with a resonator is the conventional implementation in microwave studies. In scanning microwave microscopy such resonating circuit connects closely to the probe tip and is the most common type (Imtiaz, Anlage 2003; Tselev et al. 2012; Gramse et al. 2014). The probe is part of the resonator. This method, is leading to enhanced sensitivity and simpler quantitative measurements, but only at the resonator frequency and multiples of it.

The circuit diagram in Figure 3-4 depicts such shunted resonator, which consists of a “resonating cable” and the probe itself. A directional coupler splits the incident wave from the reflected wave. The reflected wave is amplified by AMP1 and the receiver of the VNA detects the shift in resonance introduced by the DUT. The amplifier and the directional coupler are integral parts of the VNA, but drawn here outside for explaining reasons.

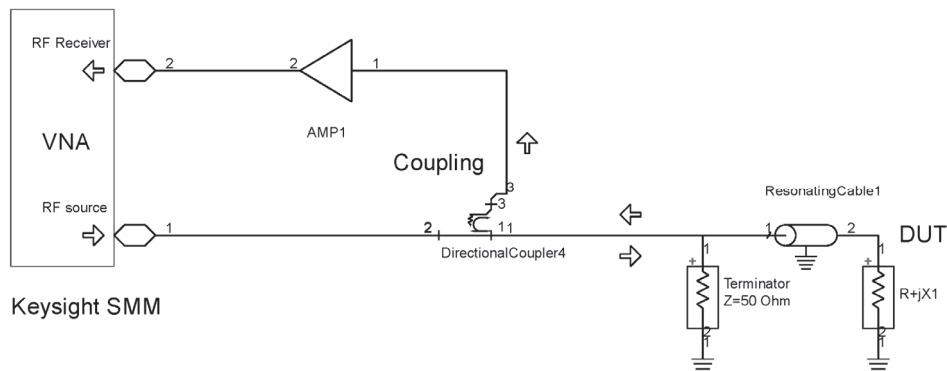


Figure 3-4 Sensitivity enhancement of a commercial SMM at high impedances (Keysight Corp. 2014). A resonating cable with a shunt/terminating resistor is integrated in the AFM head. The arrows depicts the flow of the waves. The coupler and the amplifier are integral parts of the VNA.

This microwave multistate reflectometer configuration to measure complex impedances by Keysight Corp. is influenced by the work from Oldfield et al (Oldfield et al. 1985).

A resonating setup can also benefit in terms of its simplicity, since a VNA isn't mandatory. A phase-lock-loop circuit in the receiving branch is able to detect the shift in frequency in regards to the reference (Lai et al. 2007). With such resonance frequency technique, studies relying on the knowledge of complex data originating out of a wide frequency range and high resolution needs, can certainly not be undertaken in SMM, such as pico-second time resolved solutions (van der Weide, D. W. 1997) or time-domain techniques allowing for partial disentangling signals for de-noising (Farina et al. 2011a).

An interferometric approach is another effective method enhancing the system sensitivity significantly to enable high impedance measurements in the microwave regime. Early microwave interferometric measurements in the field of precision measurement were carried out to enhance the sensitivity in oscillator phase noise measurements (Whitwell, Williams 1959), after Lengyel published a study with a Michelson-Interferometer in 1949 (Lengyel 1949). Furthermore, klystron amplifier noise measurements were conducted, by usage of such a "nulling" technique, through algebraic cancelling of two microwave signals with a hybrid multiport coupler (Sann 1968). This hybrid coupler method was introduced into microwave microscopy using two ports of a VNA (Randus, Hoffmann 2008). Also resistive power splitter and hybrids, acting in one-port reflectometer configurations, finds its way into characterization systems in RF Nanoelectronics and beyond (Lewandowski et al. 2008; Haddadi, Lasri 2012). In the field of biomedical applications, RF interferometric technology to enhance the resolution in impedance measurements in a transmission line sensor configuration is also established (Ferrier et al. 2009; Raicu, Feldman 2015). Now this technology is even

integrated in Integrated Circuits and allows contactless permittivity measurements working at 120 GHz with integrated VCO, amplifiers and detectors (Wessel et al. 2017).

A Mach-Zehnder configuration was realized in an “interferometric SMM” at IEMN (Villeneuve d’Ascq, France) (Dargent et al. 2013). In this work, a 3 dB power splitter is used to divide (“Splitting”) and a directional coupler (“Coupling”) is used to recombine both arms or waves, resulting in the interference (see Figure 3-5). The RF source signal of VNA port 1 is equally split into two branches. One path connects to a directional coupler (“Directional coupler 2”), a phase shifting cable with its connected conductive probe tip injects the source signal into the probe-sample interface. The reflected wave is recombined with the reference signal into the probe-sample interface. The reflected wave is recombined with the reference signal in “Directional coupler 1”. The reference signal is previously adjusted in amplitude via the variable attenuator, resulting in a deep “nulling” or notching after recombination with the reflected signal from the DUT. The destructive interfered signal is amplified and fed to the VNA receiver port for analyses.

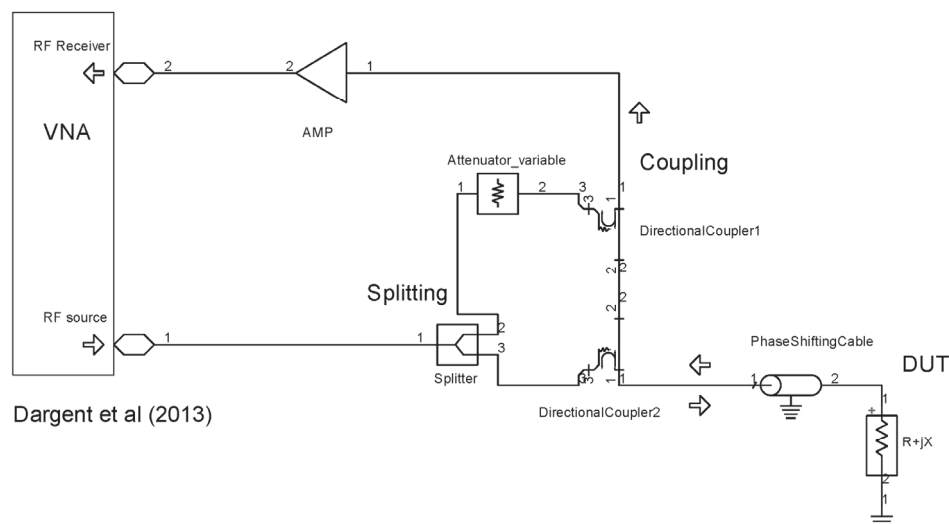


Figure 3-5 Schematic of a Mach-Zehnder interferometer for measuring high impedances. Schematic inspired by (Dargent et al. 2013).

---

In such configuration a new calibration protocol was established, in which a set of microscaled capacitors serve as reference standards, to calibrate the interferometric SMM. With these method, the quantitative study of Wang et al illustrates, under some ideal assumptions and that the change in impedance is only capacitive, that a change in capacitance correlates in linear scale to a change of the reflection coefficient (Wang et al. 2014). Calibration by dopant profiling was also presented recently (Michalas et al. 2015).

### 3.3 High-Impedance Microwave Interferometer

As mentioned, electric microwave interferometry provides high sensitivity, whilst measuring high impedance components. A further Mach-Zehnder variant of such an interferometer for use in SMM is presented and compared with two known setups.

A key component of the proposed design is a circulator. This nonreciprocal, mostly three-port, microwave element is able to couple two neighboring ports and to isolate the third, depending on the direction of circulation power flow. The scattering matrix for an ideal 3-port circulator with 120 degrees symmetry and clockwise circulation is defined as

$$[S_{Circulator}] = \begin{bmatrix} 0 & 0 & 1 \\ 1 & 0 & 0 \\ 0 & 1 & 0 \end{bmatrix}.$$

(Eq. 3-7)

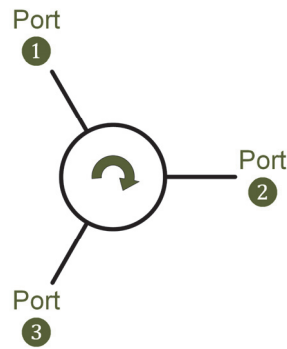


Figure 3-6 Schematic representation of a 3-port circulator with clockwise circulation.

Such a circulator is a passive microwave device and mostly based on a dielectric resonator, composed of a ferrite disc and a bias magnet. A magnetic-free variant was recently published (Estep et al. 2014). The dielectric resonator, with the magnetically biased ferrite, breaks the incoming wave into two modes with slightly different frequencies as the result of the ferrite, caused different propagation velocities. The two resonant modes adds at the output port and cancel at the isolated port by superposition leading to the nonreciprocity (Pozar 2012).

The Signal Flow or Mason Graph (Mason 1956; Hunton 1960) of the high-impedance microwave interferometer depicts Figure 3-7 in a conceptual drawing. All components are

supposed to be ideal and this apply to connectors and electric feed-through, too. In practice, splitters, cables, connectors, circulator, coupler, attenuator, amplifier and more, show amplitude and phase imbalances, return and transmission losses.

The microwave source of the VNA sends the wave  $a_2$  through port 1 and coaxial cable #1 to a power splitter. It divides the incoming signal symmetrically into a reference (upper) and a sensing (lower) path. The split signal passes a microwave circulator and via a phase shifting cable #2 the wave  $a_{DUT}$  hits the DUT. Since the impedance of the DUT, described by the reflection coefficient  $\Gamma_{DUT}$ , is not the system impedance of  $50 \Omega$ , the incoming wave (orange arrow in Figure 3-7) reflects. The reflected wave  $b_{DUT}$  (green arrow) flows through cable #2 to port 2 of the nonreciprocal circulator. Here, the incident and reflected waves are isolated. The sensing signal connects to one port of a signal combiner. The adjusted reference signal, attenuated in amplitude and shifted in phase, connects to the second port of the combiner, the interference occurs and is detected in the VNA.

In terms of node voltages in the signal flow graph, the linear transfer function between the VNA source and the VNA receiver becomes to

$$h_{IF\_Cir} = \frac{V_{sink}}{V_{source}} = \frac{1}{2} * S_{21,Amplifier} * (S_{21,Atten.} * S_{21,Phaseshifter} + S_{21,Cable\#2}^2 * \Gamma_{DUT}),$$

(Eq. 3-8)

under the above mentioned assumptions and that the phase shifting cable #2 is reciprocal. The transmission coefficient of the connection cable is square in the calculation and thus shows its overall influence to the setup.

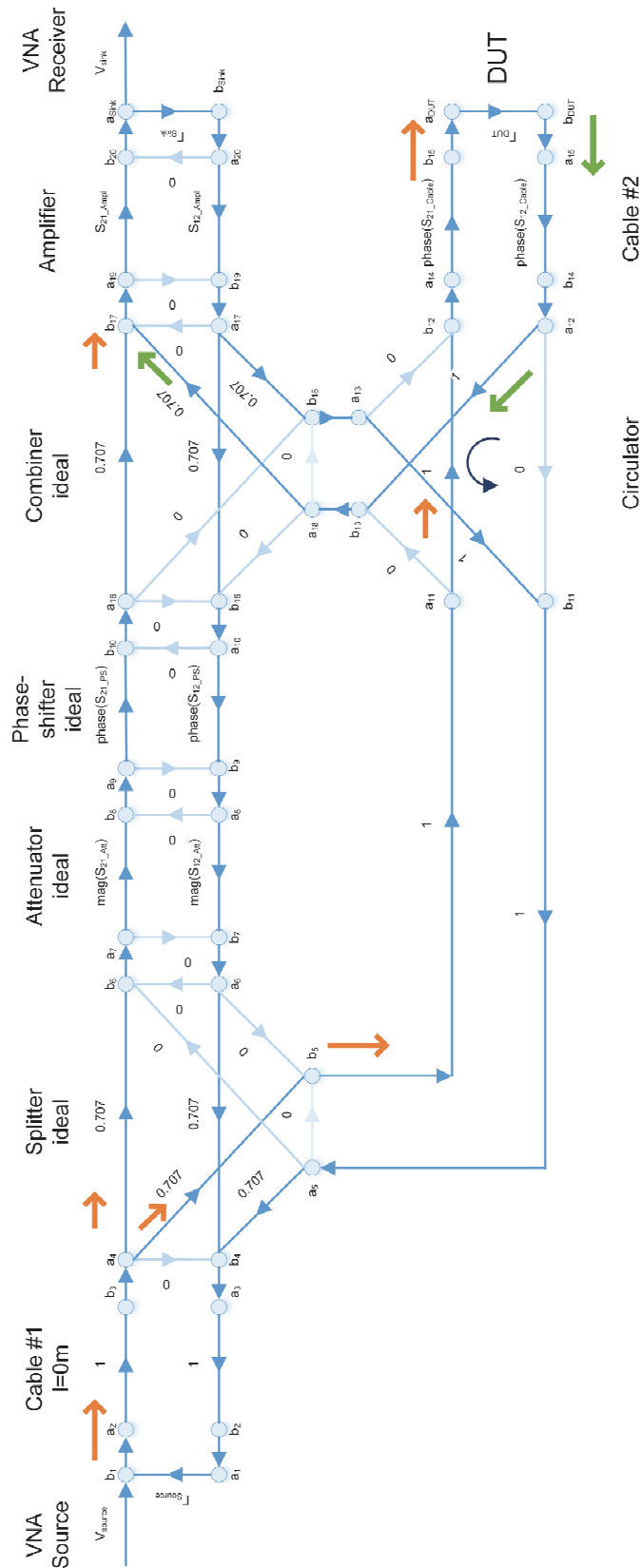


Figure 3-7 Signal flow graph of circulator version of high-impedance microwave interferometer. The red arrows representing the incident signal, whereas the green arrows represents the reflected signal from the device-under-test.

In order to demonstrate the advantage of this variant of an interferometer in SMM compared to known approaches, simulations by an electronic design automation software (Advanced Design System®/ Keysight EEs of EDA Corp.) based on the schematic shown in Figure 3-8. Subsequent comparative measurements were carried out. The DUT in the simulations was a capacitive load of 1 fF, while in the measurements it was an “Open” at the end of the cable.

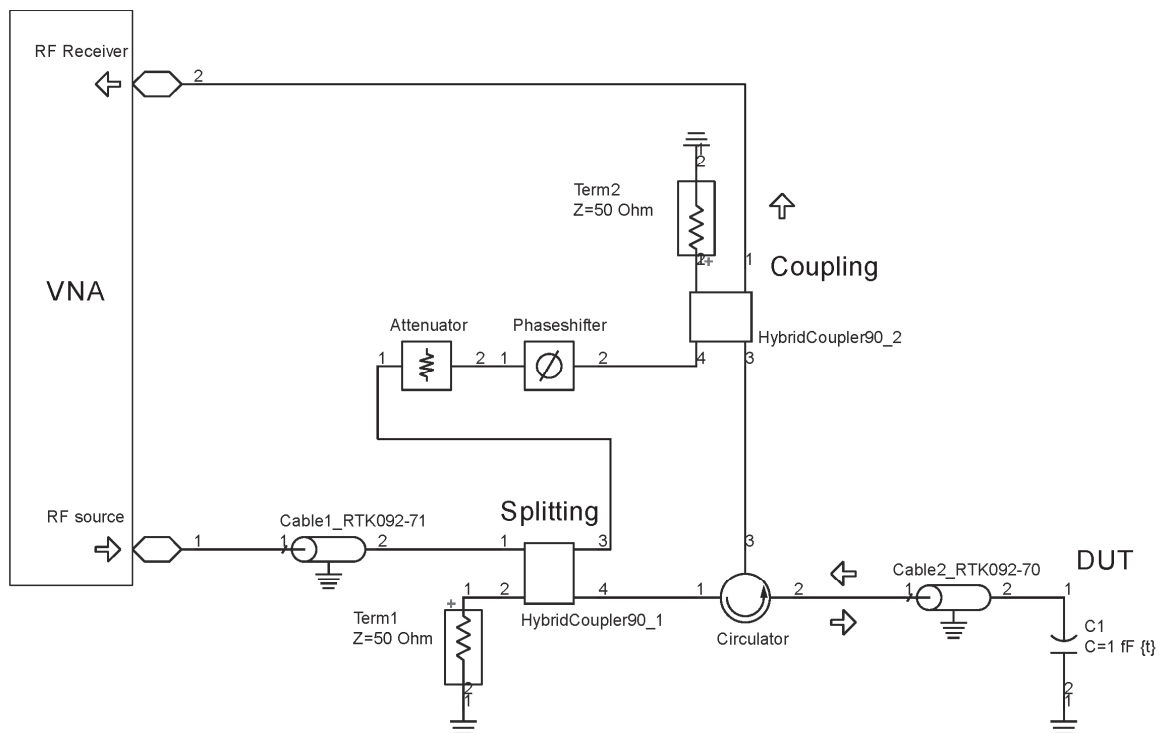


Figure 3-8 Schematic of High-impedance microwave interferometer

In the following comparison, three different wave splitting elements have been used: (i) Directional coupler (Dargent et al. 2013) (DirCoup. in the measurements: Type R433523 / Radiall Corp.) , (ii) 3 dB 90 deg Hybrid coupler (Randus, Hoffmann 2008; Haddadi, Lasri 2012) (in the measurements: Type R432431/ Radiall Corp.) and (iii) Circulator (in the measurements: Type D183 / MTC Corp.). Interferences have been adjusted in a range of  $f_{interference} = 1.5$  to 1.6 GHz, in the operating range of the used microwave devices, but no active

amplification was incorporated. To allow the three types to be compared, the simulation (dotted lines) and measurement results were normalized to the respective frequency of resonance or better: interference. The results of the simulation, with ideal elements, and the measurement, with all its imperfect devices and no amplifier involved, show similar signal characteristics. It is thus possible to make a preliminary estimation using the ADS® models in the design of such microwave interferometers for future applications. While the notch depths of interference are the same for all three and go down to -80 dB and better, the measurements show differences in the signal strength outside the interference and in the bandwidth of the interference. The hybrid coupler variant shows itself as an equal candidate in simulation. In the measurements with real components, at 0.95 or 1.05 of the normalized interference frequency, these signal differences can be observed and therefore the hybrid is between the circulator and the directional coupler version.

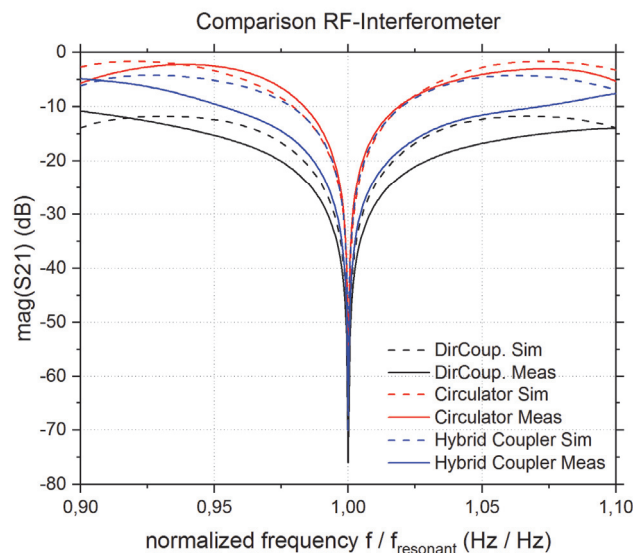


Figure 3-9 Comparison of three types of microwave interferometer in simulation (dashed lines) and testing. All graphs are normalized to their respective interference frequency, in the range 1.5 to 1.6 GHz, to allow for comparison in logarithmic scale.

The circulator version presented here, features up to 14 dB more signal and a narrower interference bandwidth against the directional coupler version, with its 10 dB coupling.

### 3.4 Summary

Due to the issues arising by measuring impedances on the nanoscale, an increased effort on the apparatus side has to be considered. One method is the implementation of an interferometric approach as demonstrated. In all three variants, it turned out that the connection cable in the direction of DUT or SUT has a quadratic and thus unfavourable influence on the measurement result and increased attention has to be paid to this point. The presented High-impedance Microwave Interferometer shows higher signals outside the interference than those published in that area. However, there is still a great potential for optimization to further increase the measurement resolution by using electrical interferometry.

This page left intentionally blank.

## 4 MULTIMODAL SCANNING ELECTRON, FORCE, AND NEAR-FIELD MICROWAVE MICROSCOPY

Performing analyses and modifications of nanoscale samples by using Scanning or Atomic Force Microscopy (SFM or AFM) and Scanning Electron Microscopy (SEM) is common practice as outlined in the previous chapter. Combining these modalities plus microwave microscopy in one workspace, merging it with robotic methodologies and integrating it by open-source software control into one hybrid technology has many advantages. Such a technology will make it possible to acquire a multi-layered, comprehensive view of the sample by enabling the following processes and strategies.

- **Multidimensional Investigation Methods**

- Multiple physical data, such as dimensional and electromagnetic, reduces the uncertainty of characterization by considering different aspects and thus it forms an over-all picture. About the power of Correlative Microscopy, see (Caplan et al. 2011).
- Spectroscopic information, contains data that originates from a single pixel position and thus from a very closely located sample volume. These can be, for example, I-V characteristic curves that are derived from biasing or variation of the current.
- Probe tip integrity inspection, within the SEM work area without disassembly, facilitates the identification of measurement ambiguities by blunted tips. A study on the influence of wear caused by oxidation on AFM silicon tips can be found in (Chung et al. 2005).

- Reduction of the AFM tip water meniscus by the vacuum environment, enhances the spatial resolution. The fundamental work on the influence of the water meniscus is by (Rozhok et al. 2004). A study by Wang et al. at IEMN examines this problem in the context of microwave microscopy. The resolution of the image quality of 100 nm nanodots is improved compared to an uncoated tip by means of a hydrophobic AFM tip (Wang et al. 2014).
- Mechanical in situ force measurements, provides an additional spectroscopic view of the sample as a future demonstrator option. Nanorobotic force measurement in the SEM were conducted in the works of Zimmermann et al. in which they automated an indentation process of 2D materials at the University of Oldenburg (Zimmermann et al. 2013).
- **Multi-modal Calibration Processes**
  - Dimensional and rotational image calibration
  - Cross correlation calibration, connects topography with microwave microscopy image information. Calibration of several optical imaging modalities is performed by introducing registration algorithms to automate the process (Tsai et al. 2008).
  - Scattering parameter calibration, permits quantitative measurements.
  - Cantilever spring constant respectively resonance frequency calibration, allows for (i) force-displacement studies, (ii) tapping mode AFM/SMM, (iii) cantilever comparisons and (iv) *in situ* detection of contaminated cantilevers.
  - Automation of calibration methods

- **Vision-based robotic techniques**
  - Localization of features by image processing, recognition and feature matching
  - Navigation of sample stage, probe tip and nano manipulators, by employing robust methods to perform image-based wafer mapping, such as so-called “geometric hashing” (Lifshits et al. 2004).
  - Live observation of probe landing and scanning process
  - Automation of robotic processes
- **Robotic manipulation strategies (in future)**
  - Blunted probe tips repair by Focused Ion Beam milling in a future integration of the setup in FIB-SEM (Zadrazil et al. 2012).
  - Modification and tuning (DC/RF) of samples and objects by nano-manipulators in-situ in an open-source nanorobotics environment. The first reported work on controlled placement of a carbon nanotube by an AFM-in-SEM system, see (Williams et al. 2002).
  - Nanohandling of samples by gripping and fixating them onto test structures / substrates. An assembly of a carbon nanofiber to the tip of a scanning probe microscope cantilever by using a microgripper in a SEM is reported by Carlson et al. (Carlson et al. 2007).
  - Automation of manipulation processes as described in reference (Zimmermann et al. 2015).

This multimodal sensing and imaging technology is targeted at measuring, transporting and manipulating samples or objects without leaving the working environment in the vacuum chamber of a scanning electron microscope. This possesses trade-offs. On one hand, it offers the possibility to enhance the lateral resolution and to reduce the parasitic capacitive effects,

both caused through the water meniscus around the probe tip. Water has a large dielectric constant of 80 at room temperature. On the other hand, a setup based on vacuum-tight components and the operation inside an electron microscope reduces flexibility for the application, because not every object is suitable for use in vacuum or electron microscopy. The first part of this chapter explains the system architecture of a demonstrator. The above-mentioned methods and processes are either implemented or will be available at a later stage due to the open software and hardware environment created at the University of Oldenburg as a modular system as a future technology option.

The second part of this chapter discusses, with the introduction of a multimodal test standard, the calibration of such a technology. The described test standard contains special features for microscopy, such as light, electron, force and microwave microscopy as well as image-processing nanorobotics.

## 4.1 System Architecture

The technology demonstrator, the Scanning Electron, Force and Microwave Microscope (SEM<sup>2</sup>), shows the feasibility of the proposed multimodal imaging technology and is composed of

- Scanning Electron Microscope (SEM, commercial),
- Scanning / Atomic Force Microscope (AFM, self-designed/-built),
- Scanning Microwave Microscope (SMM, self-designed/-built) including a Vector Network Analyzer (commercial) ,
- Sample stage, fine and coarse positioning (self-designed)
- Controller (self-built) for AFM and SMM,
- Control software with Graphical User Interface (GUI, self-designed/-built, based on open-source nanorobotic software framework OAF of the University of Oldenburg),
- Test sample (self-designed).

The vacuum-compatible multimodal system SEM<sup>2</sup> based on several hardware and software building blocks. Figure 4-1 shows the block diagram of this hybrid microscope with the functionality of probing the sample with low power electro-magnetic high-frequency evanescent waves, electron beams and atomic forces. The compact and exchangeable setup works in a Zeiss LEO 1450 tungsten SEM, equipped with a secondary electron detector and three cameras (Figure 4-1 grey). An USB3.0 sideview infrared camera records the tip-sample approach. To measure the cantilever deflection an optical interferometric approach was deployed (Figure 4-1 red). This information is fed to an AFM/SMM-controller which closes the loop by steering the piezodriven AFM-Scanner (PicoCube® / Physik Instrumente Corp.),

while this is coarse positioned by a second piezodriven stage (SLC Series / SmarAct Corp.) (Figure 4-1 green). A VNA (ZVA24® / Rhode and Schwarz, Figure 4-1 blue) is connected to the conductive tip and generates and detects the microwave signals. The software control and scan-image acquisition of the instrument is adopted to an open source software framework, called OAF, tailored for nanorobotics (Diederichs et al. 2013). More details on this see chapter 4.2.

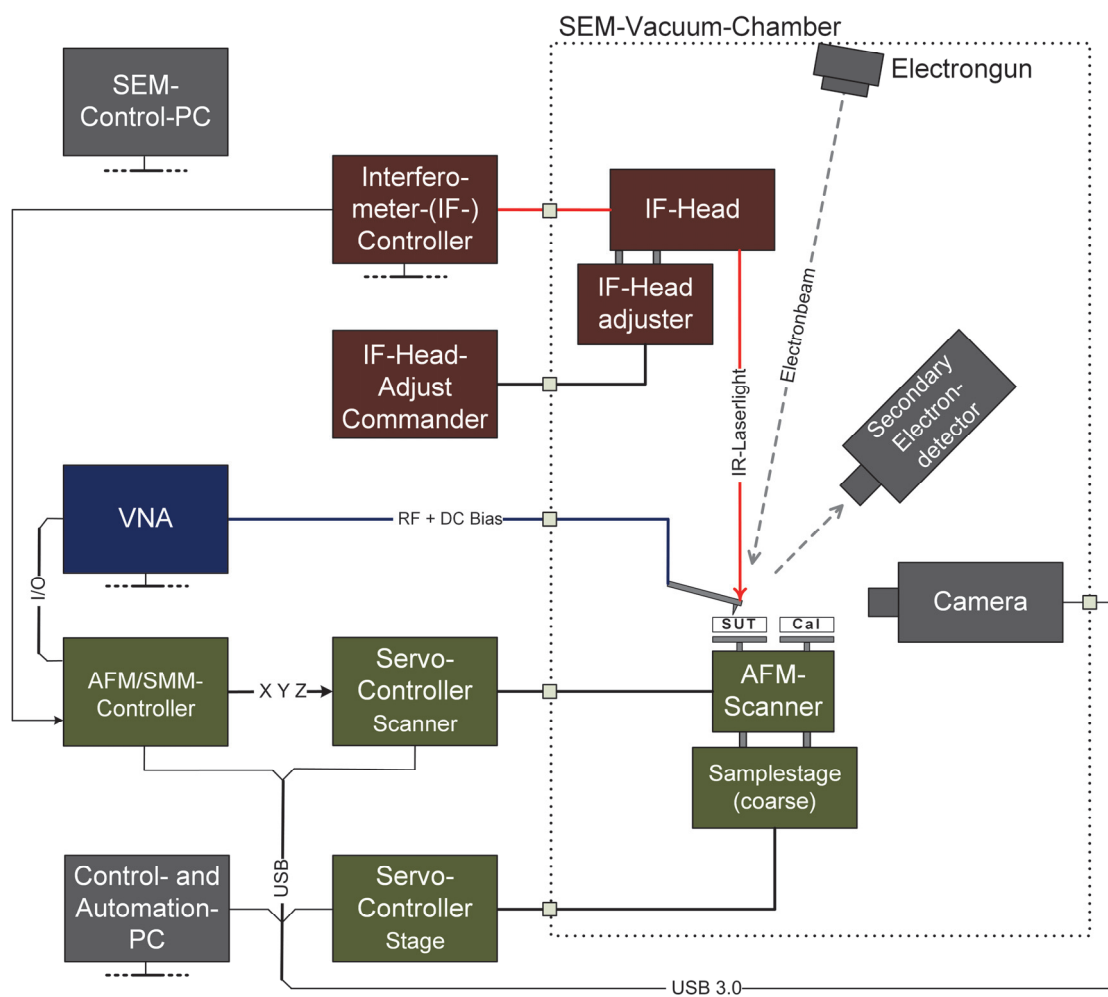


Figure 4-1 Schematic of the Scanning Electron, Force and Microwave Microscope (SEM<sup>2</sup>) with (i) Optoelectronic parts of the laser interferometer AFM (red blocks), the AFM/SMM-Scanner-Control and the sample stage (green blocks), (ii) the microwave signal detection by a VNA (blue block) and (iii) image live acquisition (grey parts) by SEM and optical camera. The dotted line illustrates the vacuum chamber of the SEM.

Any obstacle in the path between the sample surface and the secondary electron (Everhart-Thornley) detector influences strongly the signal-to-noise ratio of SEM images. To ensure a free view of the secondary electron detector to the probe tip and electron interacting sample surface, the setup has to position accordingly. A base plate holding the scanning parts mounts on a Zeiss dovetail stage-adaptor for fast setup exchange, situated on top of the SEM-Stage (Figure 4-2).

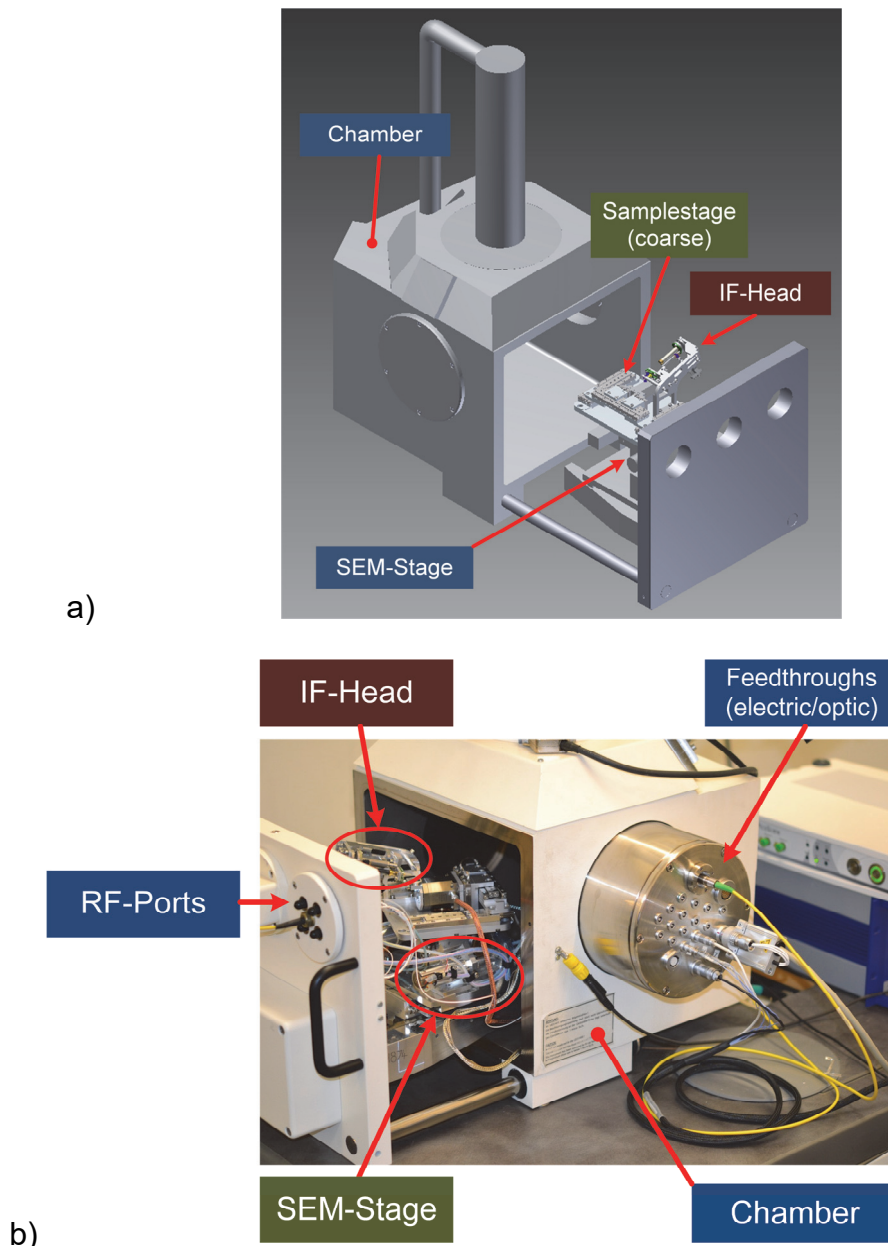


Figure 4-2 Integration into the vacuum chamber of the Zeiss LEO 1450 SEM: a) CAD view and b) photograph.

The photograph in Figure 4-2 b) on the right side reveals the control electronics of the laser interferometer AFM-in-SEM. A coaxial feed-through connects the VNA with the near-field microwave probe and additionally, a complete calibration kit, consisting of a  $50\ \Omega$ , Short and Open, is mounted in the chamber door on the left. All moving and scanning parts of the demonstrating instrumental setup attached to a base plate shows Figure 4-3. The interferometer probing head incorporated in the IF-Head adjuster tube, the AFM/SMM-Scanner and the coarse positioning sample stage illustrates the photograph including connecting fiber and cables (Figure 4-3).

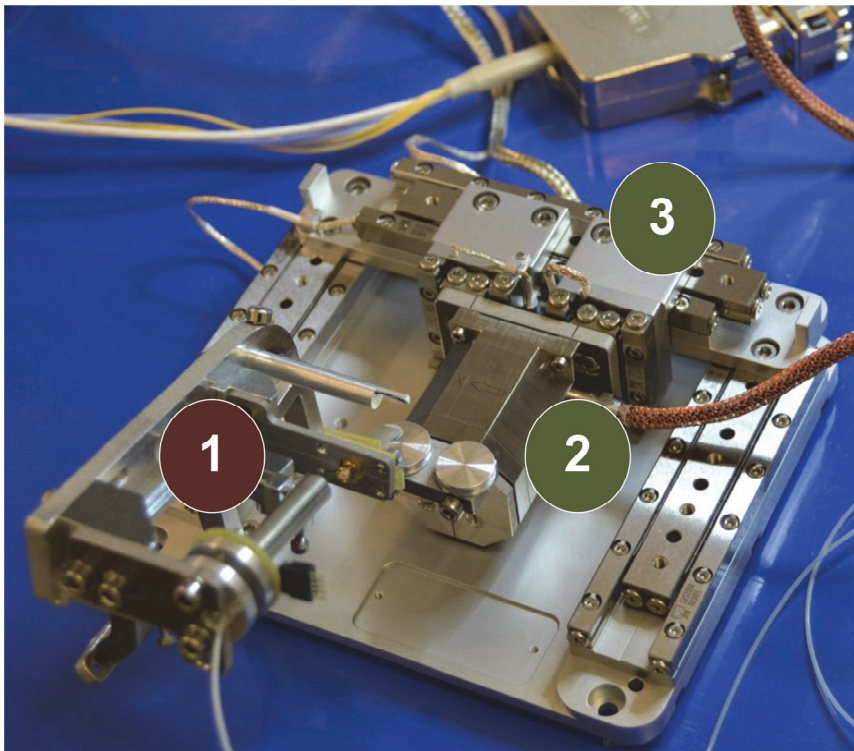


Figure 4-3 Photograph of the probing head (1), AFM-scanner (2) and sample stage (3).

## 4.2 System Control

Scanning Probe and Electron Microscopy system providers, deliver proprietary software that do not allow any modification and improvement of the equipment especially the automation and synchronization of different control processes. Equipment manufacturer are realizing this deficit, but most vendors are not willing to change. As a positive example, SPM systems offered by Park Systems Corp. recently introduced script-level control through external programs. The University of Oldenburg issued a software framework as open-source especially tailored for automation of nanorobotic processes, like characterization and assembly, also in the vacuum chamber of scanning electron microscopes. The software-framework has a modular design, enables scripted automation of various sensor and actuator components and open for integrating new equipment of various vendors, like Rhode & Schwarz, Keysight, Keithley, Zeiss, Tescan, SmarAct, Aerotech, Imaging Source and others. One central component of this framework are software tools for visual process control, object recognition and tracking. This image processing components are specifically optimized for processing noisy image data as they are common by SEM. Each subsystem can be extended with self-generated plug-ins based on software templates and defined interfaces. The development has to be done with C++ and the library Qt® (Qt Company 2017). This means that any hardware can be integrated as long as it offers a C++-compatible interface. By means of this framework, the OFFIS Automation Framework (OAF) has accomplished complete nanotechnologic characterization and assembly sequences and proofed its feasibility as a technology gateway by connecting research and industry in this niche area. For example, the implementation of fully automated selecting and mounting of exchangeable and customizable scanning probe tips onto standard AFM cantilevers during the EU-funded project “NanoBits” (Bartenwerfer et al. 2011).

Scanning microwave microscopes made by Keysight Corp. and Parks Systems Corp. provides rudimentary probe guidance by image control. Mainly, sample positioning by manual movement of the stage with camera feedback and predefinition of region-of-interests as scanning areas. In the case of multi modal imaging, using information streams originating from SEM and camera for robotic processes, such as sample or probe navigation, feature localization, live observation of probe integrity, an open and connecting system architecture is mandatory. Since the proposed technology is unique in that sense, because SMM manufacturer don't offer SEM integration in hard- and software, embedding of the SEM<sup>2</sup> system into the software framework is required.

The software control structure is made up of three main parts and depicted in Figure 4-4.

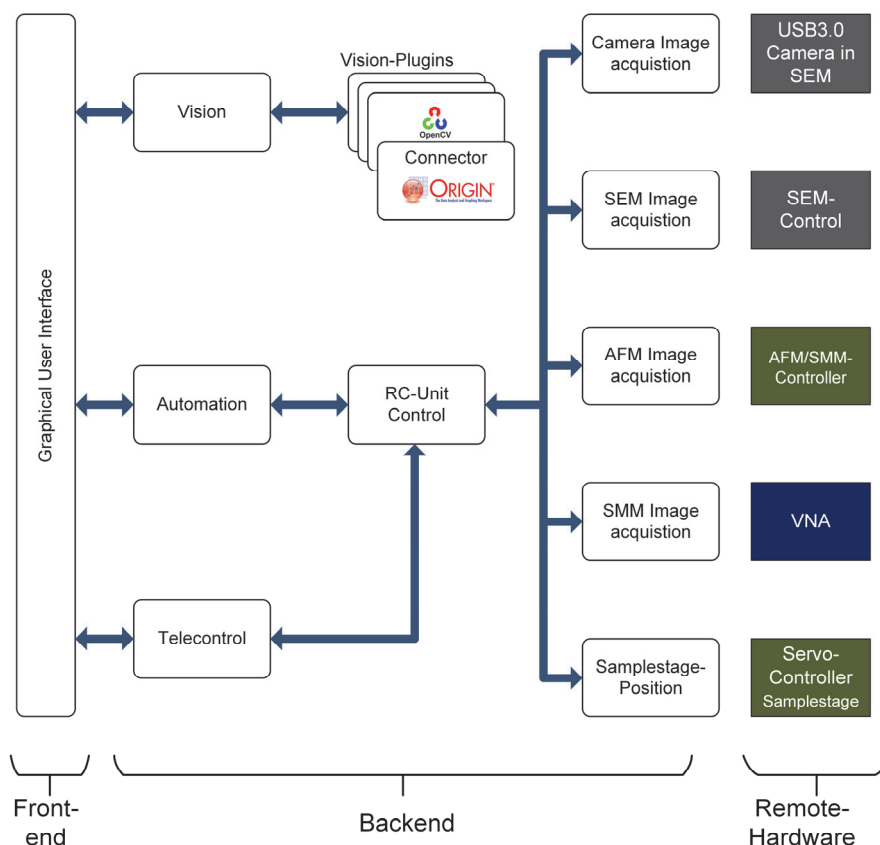


Figure 4-4 Software control architecture of SEM<sup>2</sup> by Offis Automation Framework. The three subcomponents Telecontrol, Automation and Vision are the heart and backend, of the system control and are connected by software (blue lines). The Graphical User Interface allows the user to access the system. External equipment is designated as Remote-Hardware. Scheme based partly on reference (Haenssler, Fatikow 2015).

The Frontend (“Graphical User Interface”) acts as the interface to the user. Via the GUI, the user controls the processes, as an example, by entering scan-specific data and starting it. In parallel, the acquired data of the different devices, such as cameras, AFM/SMM-Controller, VNA, or log files are visualized here. The Backend splits into the three subcomponents “Telecontrol”, “Automation” and “Vision”. The “Telecontrol” and “Automation” modules accesses the respective remote hardware via the so-called “Remote Control (RC-) Unit Control” with its device-specific command sets. Manual and semi-manual robotic controls are realized with the “Telecontrol” component. Automated processes are implemented with the scripting language Python® in the "Automation" module. In the independent parallel running module “Vision” several vision plugins, on the basis of the open-source library “Open CV”, are integrated. They enable image-based control processes, such as object recognition and image filtering, to name but a few. In the framework of this work, an active data link to the commercial data analysis and graphing software Origin® (by OriginLab Corp.) was built in.

Data acquisition and control of the scanning process synchronously in time and space is the role of the AFM/SMM-controller. The self-built AFM/SMM-controller (Figure 4-5) incorporates an FPGA (Zynq® 7020 / Xilinx Corp.) for such software control requirements and

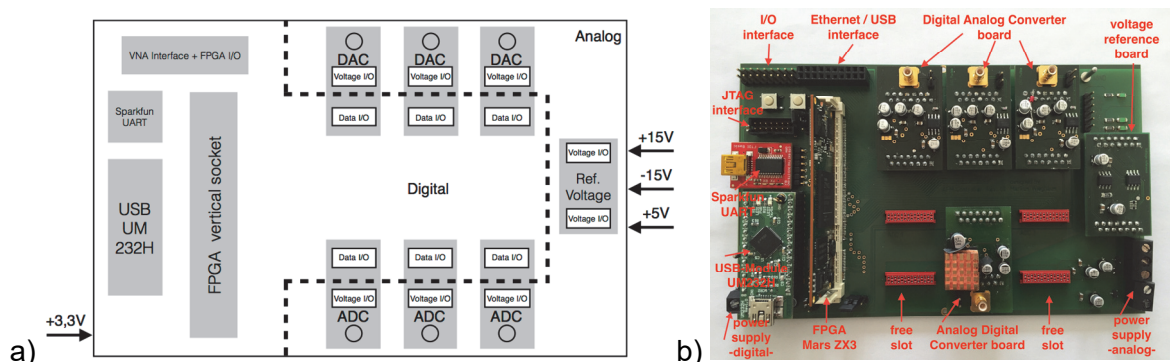


Figure 4-5 AFM/SMM-Controller a) Overview with FPGA, digital and analog parts. Fitted with three DA- and AD-Converter. b) Photograph: Left side: FPGA with USB-Interfaces. Middle: One ADC and three DAC. Right side: Reference voltage source for DAC and ADC. Images adapted from reference (Wieghaus et al. 2016).

is capable of controlling two microscopy modalities, atomic force and near-field microscopy (Wieghaus et al. 2016) .

The acquired data streams into the aforementioned OAF software framework, such as live camera frames. An overview of the controller features lists Table 4-1 below.

*Table 4-1 Datasheet AFM/SMM-Controller*

<i>Controller-Features</i>	<i>Details</i>
FPGA	Enclustra© Mars ZX3: Zynq® 7020 incl. ARM® Dual-core Cortex® A9 667 MHz and Xilinx Artix® 7; 512 MB DDR3 RAM, 64 MB Flash
Interfaces, digital	Gigabit Ethernet; 108 User I/Os; USB 2.0 Hi-Speed (480Mb/s) and USB-to-Serial
Interfaces, mixed signal	Up to 6 piggy-backs connections with digital I/O and analog supply voltages
I/O Piggy-backs	<ul style="list-style-type: none"> <li>• ADC: Linear Technology LTC2338-18, 18 Bit, 1 Msps, <math>\pm 10.24</math> V True Bipolar input, max INL <math>\pm 4</math> LSB</li> <li>• DAC: Analog Devices AD5760, 16 Bit, 2.5 <math>\mu</math>s output voltage settling time, 0V - 10V output Voltage, max INL <math>\pm 0.5</math> LSB</li> <li>• Reference voltage source: Analog Devices ADR4550, 5V DC, Initial output voltage error: <math>\pm 0.02\%</math> maximum, Output noise (0.1-10 Hz) <math>&lt; 2.5 \mu</math>V<sub>p-p</sub></li> </ul>
Others	<p>Integrated in OAF as an Remote Control Unit;  Supports daisy chaining of multiple controller via Ethernet,  GP I/O or USB and Linux® BSP OS on on-board ARM® core</p> <p>Raster scan or arbitrary scan trajectories</p>

Its free programmability offers interesting new options. Even in SPM systems of Park Systems Corp., a leading and innovative equipment manufacturer, raster trajectories are still line-by-line, with the ability of scanning starting at multiple positions. As it was mentioned in the introduction, non-raster capabilities will enable extraction of data from non-orthogonal axes to speed up the imaging process through spiral, cycloid or Lissajous trajectories. This is one

included feature, which is beyond state of the art in Scanning Microwave Microscopy and included in the graphical user interface.

To demonstrate the open technology approach with other scanning techniques an additional FPGA frontend was designed. For the above mentioned EU-funded project “NanoBits” a quad high-resolution 20 Bit Digital-to-Analog-Converter connects to FPGA Xilinx© hardware offering sidewall scanning trajectories to monitor the quality of Bosch DRIE processes in MEMS based structures (Figure 4-6). It is integrated into a commercial AFM (NanoWizard® / JPK Corp.) and controlled through OAF (Krohs et al. 2014).

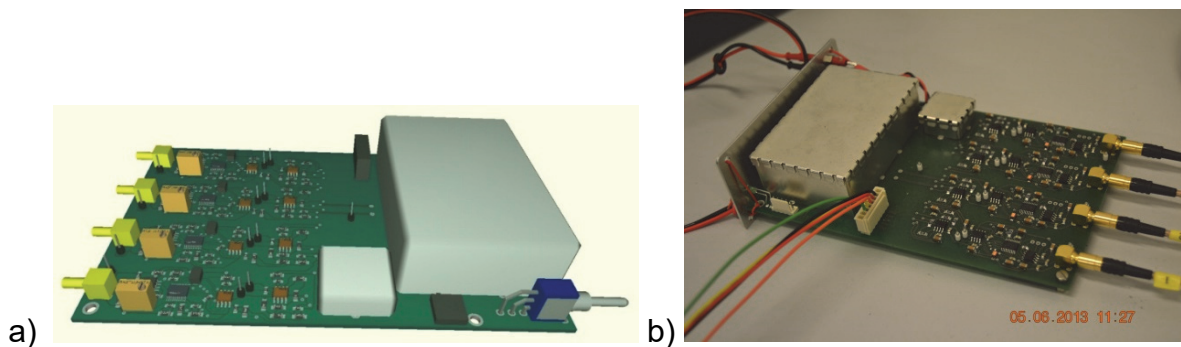


Figure 4-6 AFM-DAC-Highend frontend 4x20 Bit. a) CAD view b) Photograph with the connections to JPK NanoWizard.

### 4.3 System Test

After the various elements of the technology were explained in detail and then merged to form a technology demonstrator, the final part of this work is its validation. Prior to demonstrating a complete multimodal measurement of the test standard, tests to the overall control of the Scanning Electron, Force, and Microwave Microscope are included.

Testing and verifying the functionality of the system architecture and AFM/SMM-Controller with defined microwave signals, but without conducting real scans with the cantilever probe, is an efficient real-time software verification method. A specific designed hardware-in-the-loop (HIL) simulator, emulating repetitive varying microwave properties of a sample displays Figure 4-7.

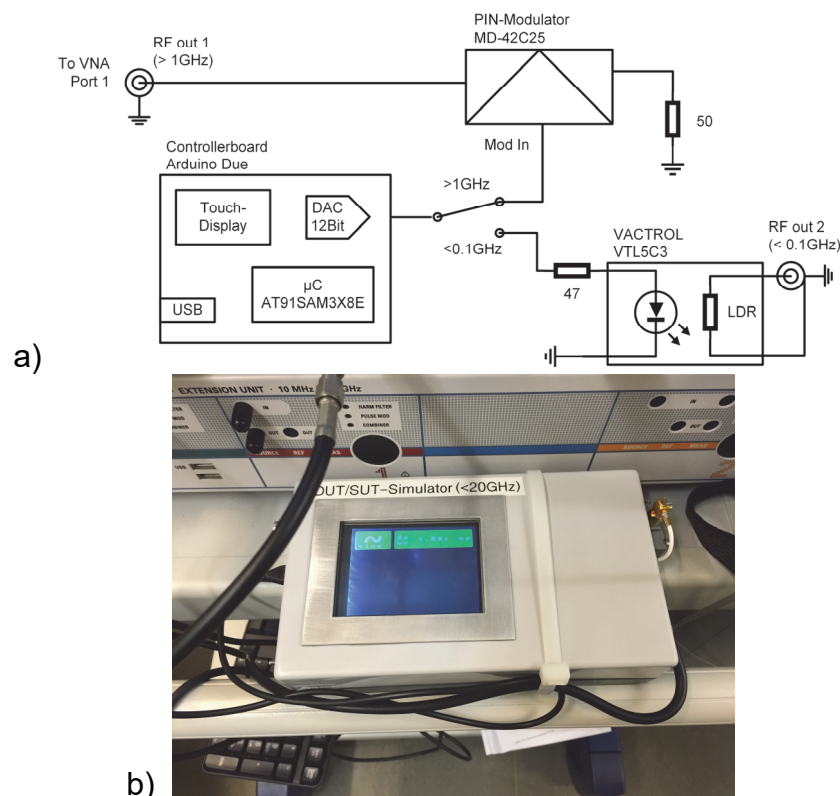


Figure 4-7 Simulation hardware to emulate varying  $S_{11}$ -Parameter. a) Schematic with micro-controller and RF-Modulator b) Photograph: DUT-Simulator connected to VNA. Figure a) adapted from reference (Wieghaus et al. 2016).

A port of the VNA is connected to this DUT-Simulator, which is based on a microcontroller (Arduino Due® / Atmel Corp.). It generates a voltage signal with user-defined shape, like sine, sawtooth, DC, or triangle. The repetition respectively line scan frequencies are in the range of max. 2 Hz. This emulates the change of complex reflection coefficient  $S_{11}$  of a scanning SMM cantilever in the microwave region of the spectrum (1 GHz to 14 GHz). The main component is a biased PIN-Modulator (MD-42C25), driven by the internal 12-Bit-DAC of the AT91SAM3X8E. Additionally, a switchable second mode emulates the same behavior in frequency regions below 100 MHz. In this mode, a galvanic isolating Vactrol® (VTCL5C3 / Excelitas Corp.) emulates the change of impedance. The modulated impedance shift results in a variation of the complex S-Parameter  $S_{11}$ , Figure 4-8 displays such an HIL simulation in which the incident wave from the VNA is sinusoidal modulated with 0.5 Hz during forward and backward scanning with 1 Hz. A function generator emulates in this case the output of the topography sensor by a 10 Hz sinusoidal waveform.

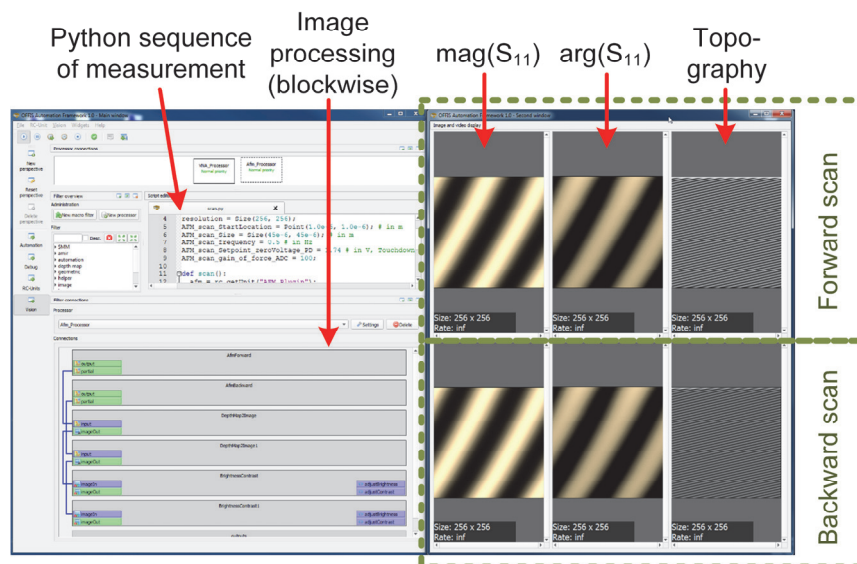


Figure 4-8 Hardware-in-the-loop emulation of microwave properties. The Graphical User Interface of the SEM<sup>2</sup>-Control-Software shows on the left the vision plug-in Control and on the right scan images. The upper part on the right relates to the forward scan and the lower part to the backward scan. The DUT-Simulator emulates the magnitude and phase of the complex  $S_{11}$ -Parameter in the RF region and an external function generator emulates the topography. The DUT-Simulator modulates sinusoidal the incident wave from the VNA. Other modulation waveforms are integrated. The Figure was published in reference (Haenssler, Fatikow 2015).

As shown, the results of scanned images are displayed in the right part of the Graphical User Interface, while the control blocks and scripts of the vision plugin are displayed on the left. The data presentation takes place directly, so that the respective images for the forward and backward scans are built up live. One of the OAF's features is to display other sensors, such as cameras. However, this is not the case in the shown picture. Due to the constant and daily expanding development of this open source software at the University of Oldenburg, only a snapshot can be shown here.

## 4.4 Multimodal Calibration and Test

While in micro- and nanorobotic processes microscopes are the main sensing tools one question rises up: How to connect the various imaging data sources to gain a big picture of the Sample-Under-Test and then to conduct robotic navigation and in future automated manipulation with sufficient precision? A well-defined multimodal test standard consisting of features linking all of the microscopes, used in this thesis, in the 2D space, is one step to solve this.

Diverse calibration routines for different kinds of microscopes to obtain the magnification and to remove spatial (static) and drift (time varying) distortions are known. For five decades the Correlated Light Microscopy and Electron Microscopy (CLEM) is bridging two modalities (Boer et al. 2015) and has been implemented in commercial available products (Zonneville et al. 2013). It marks the beginning of correlated microscopy with its application in cell biology.

Due to inaccuracies of the objective lenses and variations in the setup of the beam system itself, the estimation of observed object sizes and positions in the Field-of-View (FOV) are erroneous.

In Light Microscopy (LM) calibrated micrometer scales or test specimens, like grids and crossed hairs, are used to calibrate the image and its positioning sample stage. These objects are placed in the focal plane and a conversion factor is calculated.

In Scanning Electron Microscopy (SEM), which is the major instrument to image, measure and even to manipulate in the micro- and nanometer range, the correct estimation of the magnification is more difficult. The error in magnification can be between 5% and 10% and changes naturally with the working distance and scan rate. The astigmatism, an inherent error in SEM, has to be reduced as well, through imposing a compensating field generated by the stigmator. In the working range down to magnification of 1000x, traceable standards to calibrate both LM (reflected light) and SEM are available and composed of crossed scales and

hairs to ease navigation. One common SEM test specimen in R&D is the “Geller MRS-6 standard” (SPI Supplies, West Chester, PA, USA). It covers the calibration of magnification for LM, SEM (Electron sources: tungsten, LaB6 and field-emission) and AFM. Pitch and bar patterns (similar to so called “USAF 1953”) ranging from 80 nm to 3  $\mu\text{m}$  are shaped by 15 nm thick Chromium deposits on a Silicon die. This calibration standard features the richest variety of test structures for various types of microscopes, but not for microwave microscopy.

By using SMM calibration samples and procedures complex impedance measurements and quantified measurements of dielectric constants and loss tangents over a broad range of frequencies up to 20 GHz (Gramse et al. 2014; Dargent et al. 2013; C. Gao and X.-D. Xiang 1998; H. P. Huber et al. 2010) and up to 70 GHz (Farina et al. 2011b) are enabled. Material properties are derived by measuring the complex scattering parameter with a VNA and converting it into e.g. impedance. Two commercial available products of SMM calibration test specimens are known (MC2 Technologies; IMEC). A compilation of known standards featuring structures for several microscope modalities and for SMM lists Table 4-2. It should be noted that in microwave microscopy, either calibrated capacitances or differently doped layers of semiconductors are mainly used.

*Table 4-2 Multimodal microscopy test standards*

<i>Modality</i>	<i>Type of standard</i>
LM, SEM, AFM, STM	MRS-6 Reference Standard (Geller Corp.): Resolution testing: 3 bar targets 80 nm – 3 $\mu\text{m}$ ; Stigmation testing: Six squares 80 nm – 2 $\mu\text{m}$ pitch; Pattern height 15 nm (SPI Supplies, West Chester, PA, USA)
	Nanoscale Linewidth/Pitch Standard (Supracon Corp.): Gratings (circular/square) with pitches 160 nm - 4 $\mu\text{m}$ ; 10 bar targets: 80 nm - 2 $\mu\text{m}$ ; Chessboard: 4 $\mu\text{m}$ pitch (Huebner et al. 2007)

SMM	Staircase of microcapacitors (MC2 Technologies):
Capacitance	4 x 50 nm height steps of SiO <sub>2</sub> on top of highly-doped silicon are covered with circular Au-on-Ti pads of diameters ranging from 1 μm to 10 μm and 4 x 144 1 μm to 4 μm resulting in capacitors between 0.1 fF to 22 fF (Hoffmann et al. 2012; H. P. Huber et al. 2010)
	Grid of microcapacitors:
	7 x 7 square Au on Ti pads 3x3 μm <sup>2</sup> on top of SiO <sub>2</sub> resulting in 11 fF (Karbassi et al. 2008)
SMM	Doped stripes (IMEC):
Doping	Several layers with different doping intensities and staircase thicknesses (5x10 <sup>19</sup> , 5x10 <sup>18</sup> , 1x10 <sup>18</sup> , 7x10 <sup>16</sup> and 1x10 <sup>16</sup> atoms/cm <sup>3</sup> ) n- or p-type doped (Schweinböck, Hommel 2014)
	Dopant stripes (Infineon Corp.):
	One stripe with striped dopant concentrations of n-type increasing from 4 x 10 <sup>15</sup> to 1 x 10 <sup>20</sup> cm <sup>-3</sup> and than p-type decreasing from 1 x 10 <sup>20</sup> to 4 x 10 <sup>15</sup> cm <sup>-3</sup> and cross-shaped stripes forming p-n-junctions (Schweinböck, Hommel 2014)
SMM	Staircase dielectrics:
Dielectrics	Four staircase lines width = 10 μm with 26, 38, 48 and 63 nm height, resulting in dielectric constants of 3.9±0.2, 4.3±0.4, 6.6±0.9 and 4.7±0.4 (Gramse et al. 2014)

By performing measurements of different microcapacitor values with the conductive cantilever in contact mode, it is possible to extract the parasitic capacitances of the probe-tip system (Wallis et al.). The lowest value of the standard capacitor limits these quantified measurements down to 0.1 fF, but recent developments are going into attofarad sensitivity (Dargent et al. 2013).

For profiling dopant intensities of semiconductors the “doped layer” type of test standard is mainly used for applications in semiconductor R&D.

For force spectroscopic measurements, the knowledge of the spring constant is of fundamental importance for estimating the forces acting on the specimen. High forces can alter soft materials of the samples to such an extent, that these falsify the topography measurements. Another point is, that the cantilevers used for such measurements must be comparable. However, since the thicknesses can vary around factor three to five, a comparison of the spring constant is advisable and good practice. In the literature there are different approaches to calculate these from AFM measurements. One elegant method of calculating the spring constant without touching the cantilever or bringing it into contact with a surface is by detecting the thermal noise. Since the cantilever is in thermal equilibrium with its environment, it possesses an intrinsic energy that is determined by the ambient temperature. This results in an energy equilibrium between kinetic (thermal) and potential (mechanical) energy. With a knowledge of the deflection and the resonance frequency, induced by the thermal noise, it is possible to determine the spring constant (Sader et al. 1999; Gates, Pratt 2012).

#### 4.4.1 Multimodal Test Standard

A combination of some of the above mentioned calibration structures on one substrate to establish a multimodal calibration standard, is designed: Pitch and bar pattern for image, resolution and height testing of LM, SEM and AFM and arrays of microcapacitors for SMM. These lateral test features for hybrid microscopy are horizontally and vertically connected to enable visual-servoing in robotic micromanipulation processes by these finding structure (Shi et al. 2016; Banerjee, Gupta 2013). The test standard aims to connect three microscopy modalities, LM, SEM, and SMM.

#### Design and Fabrication

The fabricated test structures contains patterns for the alignment in SEM as well as patterns for the SMM measurements. The alignment marks consists of Geller standard structures, mentioned above, whereas the SMM patterns consists of circular dots having diameters of 1  $\mu\text{m}$ , 2  $\mu\text{m}$  and 4  $\mu\text{m}$ . Since standard photolithographic techniques were intended to be used for the fabrication of the structures, a 4" \* 4" mask was designed having square periods with dimensions 10 mm \* 10 mm each (see Figure 4-9).

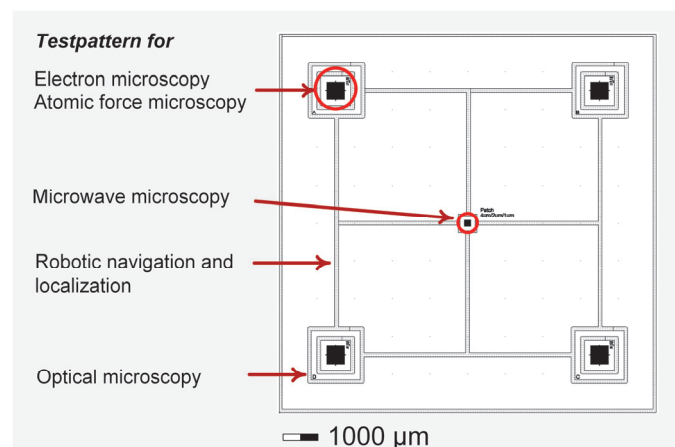
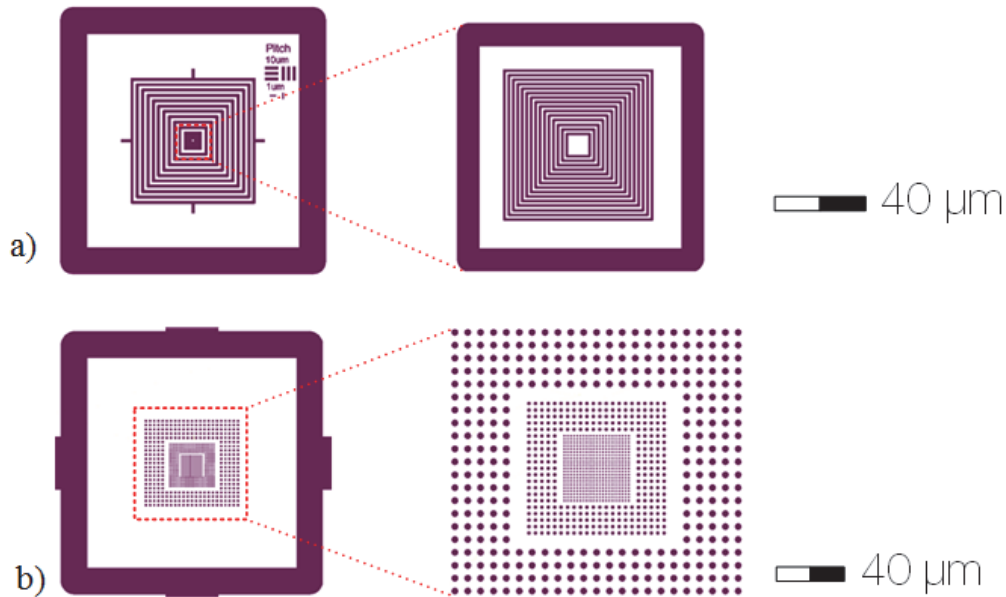


Figure 4-9 Layout of the multimodal test standard. Scheme based on reference (Haenssler et al. 2017).

The geometries at the four corners of the produced test sample are indented for SEM calibration [ b) and zoomed image c) in Figure 4-10] whereas the SMM microcapacitor patterns situated in the center are shown in Figure 4-10 b).



*Figure 4-10 Detailed zoomed images of the multimodal test standard. a) At each four corners: rectangle finding structures for light microscopy and inside these corner features for resolution and astigmatism testing in SEM. b) In the center: microcapacitors for SMM. Scale bars are valid for the parts on the right. Figure was published in reference (Haenssler et al. 2017).*

Optical lithography was used at FORTH, Greece, for fabricating the test structures employing the AZ2020 photoresist. The patterns on top were formed by depositing on both Si and SiO<sub>2</sub>/Si substrates 120 nm thick Au by e-gun evaporation. The Si used was single polished, highly conductive ( $\sim 10^{-3} \Omega\text{cm}$ ), n-type (111) wafer, and the SiO<sub>2</sub> was formed by thermal oxidation having a thickness of 250 nm. Aluminum was evaporated at the back of the substrates to form the back contact for grounding the sample to avoid charging effects in SEM.

Typical SEM images of the geometries of the fabricated structures are shown in the Figure 4-11 below. Astigmatism calibration of an SEM can be conducted with the parallel rectangular structure a) with a pitch of 2 μm. On the upper right corner (not shown here) additional etched

vertical and horizontal bars allows for SEM resolution calibration. For the high-frequency calibration of an SMM three different values of capacitances are shown in Figure 4-11 b).

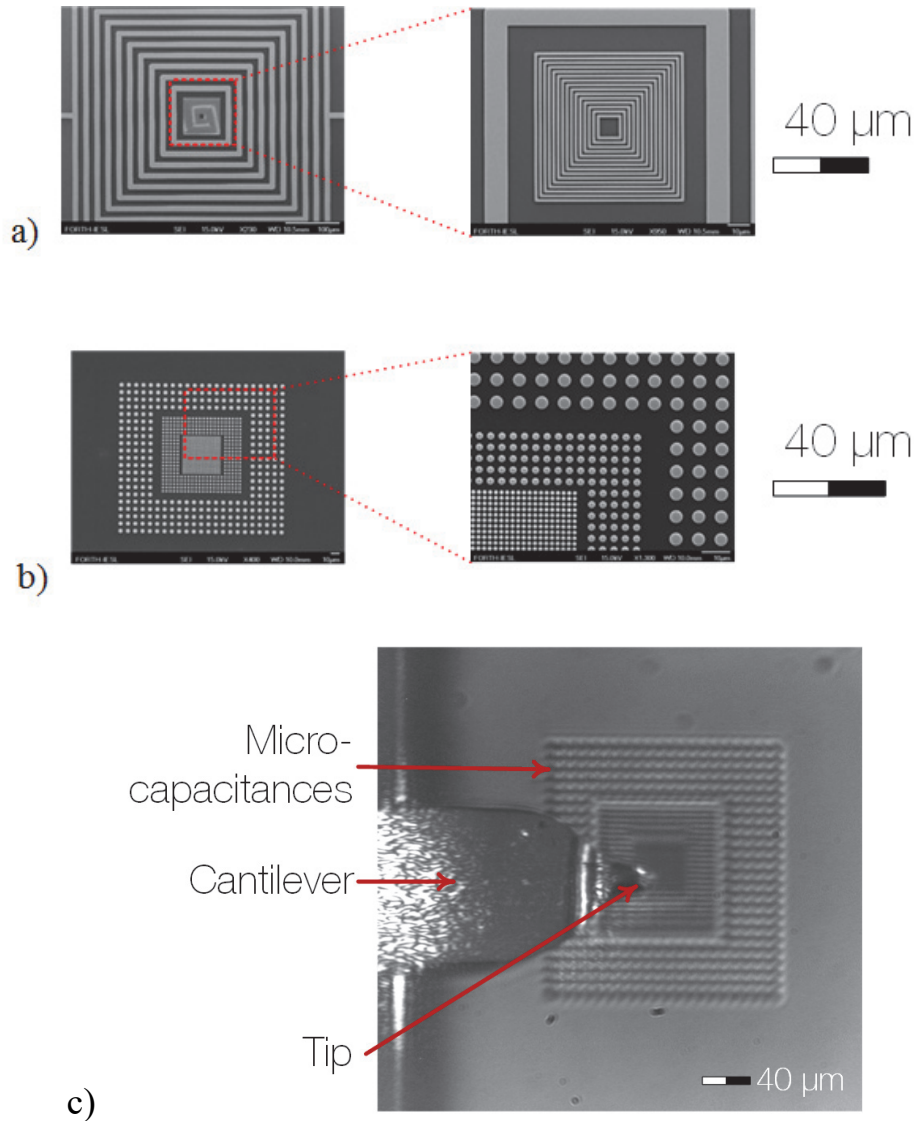


Figure 4-11 a) Electron micrographs of the finding structures for light microscopy and SEM, b) Electron micrograph of the capacitors for SMM and c) Top view micrograph of the cantilever and SMM capacitors while scanning. Scale bars are valid for the parts on the right. Figures were published in reference (Haenssler et al. 2017).

## Micro-scale Capacitors

Arrays of Metal-Oxide-Semiconductor (MOS) capacitors validates the proof-of-concept of the imaging technology. Due to the geometric aspect ratios in such scales, the fringing fields, originating from the sidewall edges and the top of the upper plate of microscale capacitors, has to be taken into consideration (Love 1924) when calculating the total capacitance  $C_{\text{Micro Cap}}$ .

$$C_{\text{Micro Cap}} = C_{\text{Parallel-Plate}} + C_{\text{Fringing}}$$

(Eq. 4-1)

A sketch of the photolithographically fabricated capacitors with the field lines for illustration is shown in Figure 4-12.

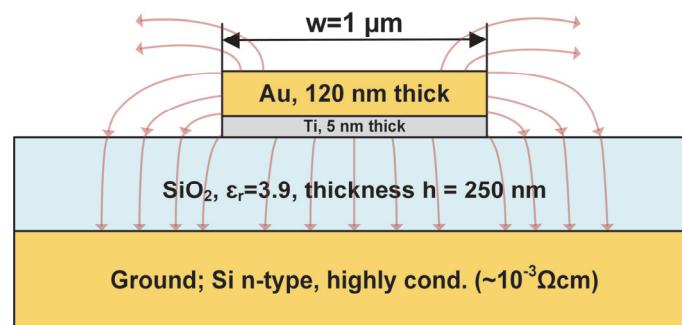


Figure 4-12 Cross-sectional view of the investigated microcapacitor with electric field lines illustrating the fringing effect.

Several approaches to determine the value of microscaled MOS capacitors has led to numerous approximation formulae (Elmasry 1982; Yuan, Trick 1982; Sakurai, Tamaru 1983; van der Meijs, Fokkema 1984; Ruehli, Brennan 1975; Batra et al. 2006; Barke 1988; Chuang et al. 2012). The reference used in all studies to calculate the total capacitance, used a complex approximation conformal mapping technique based on the Schwarz-Christoffel transformation (Chang 1976). A simplified formula (Eq. 4-2) of capacitance over unit length  $c$  was introduced

by Chuang et al (Chuang et al. 2012). It took into account the sidewall and top-surface fringing field effects for rectangular microbeam structures.

$$c = \varepsilon * \left[ \left( \frac{w}{h} \right) - 1.06 + 3.31 \left( \frac{t}{h} \right)^{0.23} + 0.73 \left( \frac{w}{t} \right)^{0.23} \right],$$

(Eq. 4-2)

$w$  is the width of the top plate,  $h$  is the height distance between the top and the lower ground plate forming the capacitor,  $t$  is the total thickness of the top plate and  $\varepsilon$  is the permittivity of the dielectric. The geometrical range of validity is given to  $w/h > 0.1$  and  $0.1 < t/h < 10$ . Using finite element electromagnetic simulation, the theoretical values of the used capacitances were derived. Based on (Eq. 4-2) the following approximation for the round microscaled capacitors in the used geometrical range was found (Eq. 4-3). The first term describes the parallel plate contribution, follows compensation term, sidewall and top plate fringe portions.

$$C_{Micro\ cap} = \varepsilon * w * \left\{ \left( \frac{w}{h} \right) + 2 * \left[ 1.65 + 0.01 \left( \frac{t}{h} \right)^{0.23} + 0.01 \left( \frac{w}{t} \right)^{0.23} \right] \right\} * \pi/4 \begin{cases} \frac{w}{h} > 0.1 \\ 0.1 < \frac{t}{h} < 10 \end{cases}.$$

(Eq. 4-3)

The results of a correlation of known approaches, simulation analysis and the approximation for the structures used in this study are shown in Figure 4-13. The values of the rectangular parallel plate capacitor without fringing effect indicates the black line.

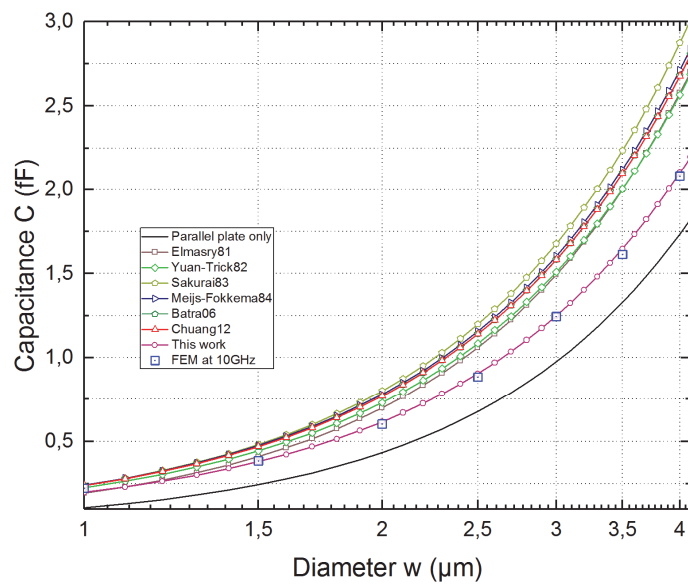


Figure 4-13 Comparison: Capacitance vs diameter of metal dots. Different electrostatic field approximation formulas are compared to a FEM analysis at 10 GHz and (Eq. 4-3).

Round capacitor arrays of three diameters ( $w = 1.5 \mu\text{m}$ ,  $2 \mu\text{m}$  and  $4 \mu\text{m}$ ) with the same  $\text{SiO}_2$  dielectric height ( $h = 250 \text{ nm}$ ), top plate thickness ( $t = 125 \text{ nm}$ ) were used for imaging. Their calculated correspondent values become 380 aF, 615 aF and 2.10 fF. By using the approximation (Elmasry 1982), differences to the results by (Eq. 4-3) is found to be 5%, 7% and 10% respectively for the given capacitor values. Table 4-3 summarizes the test features.

Table 4-3 Datasheet Multimodal test standard

Modality	Details
LM, SEM, AFM, STM	Resolution testing: 2 bar targets $1 \mu\text{m} - 10 \mu\text{m}$ ; Stigmation testing: Two nested squares $1 \mu\text{m}$ and $10 \mu\text{m}$ pitch; Height testing: Au pattern height 120 nm
SMM Capacitance	Dielectric $\text{SiO}_2$ with round pads diameter 1,2 and $4 \mu\text{m}$ , thickness 250 nm resulting in 340 aF to 2 fF capacitance

#### 4.4.2 Robotic Calibration Procedure

The components described above are used in a system that operates within a robotic software framework. By the various implemented microscopy modalities it is possible to obtain multiple information about the SUT from different viewing angles. In the OAF, a wide variety of imaging devices such as SEM and optical cameras are integrated as independent sensors and can be accessed in live operation. Through the integrated open-source Computer Vision Library Open CV (Bradski 2000) it is possible to apply image, filter and object recognition algorithms to the sensor data generated by the imaging sensors. The results can then be transferred to other processes.

The possibilities that can result from such system, are described on the basis of a calibration procedure with micro-scale capacitors in the following Figure 4-14. Sensor and actuator processes, like image acquisition or stage movements, are represented in the diagram by solid lines, while data processing operations are represented by dashed lines. The individual processing blocks are self-explanatory and show in their entirety a possible sequence of a SEM driven calibration process, in which micro-scale capacitors, as part of a sample-under-test, are used as calibration capacitors. At the end there are calibration datasets available for further use.

After the SEM has been initialized and a survey of the whole sample has been recorded, alignment masks are detected, localized and compiled in a map (step #5). The SUT moves to the reference position using the sample stage. A comparison with the known CAD layout of the sample-under-test is performed to determine whether all calibration capacitors have survived the production process (step #7 to #10). In the next step, the capacitance values are pre-calculated on the basis of the procedure described in the previous chapter, after various image processing algorithms have been carried out (step #11 to #15). After the initialization of AFM and SMM, the individual micro capacitors are measured in topography and scattering

parameters and after various calculations, the capacitance value is stored in the form of a map (step #16 to #22). A comparison between the values generated from the SEM and the values created from the microwave microscope is stored in an error map. The capacitor values are now available for use in further measurement processes.

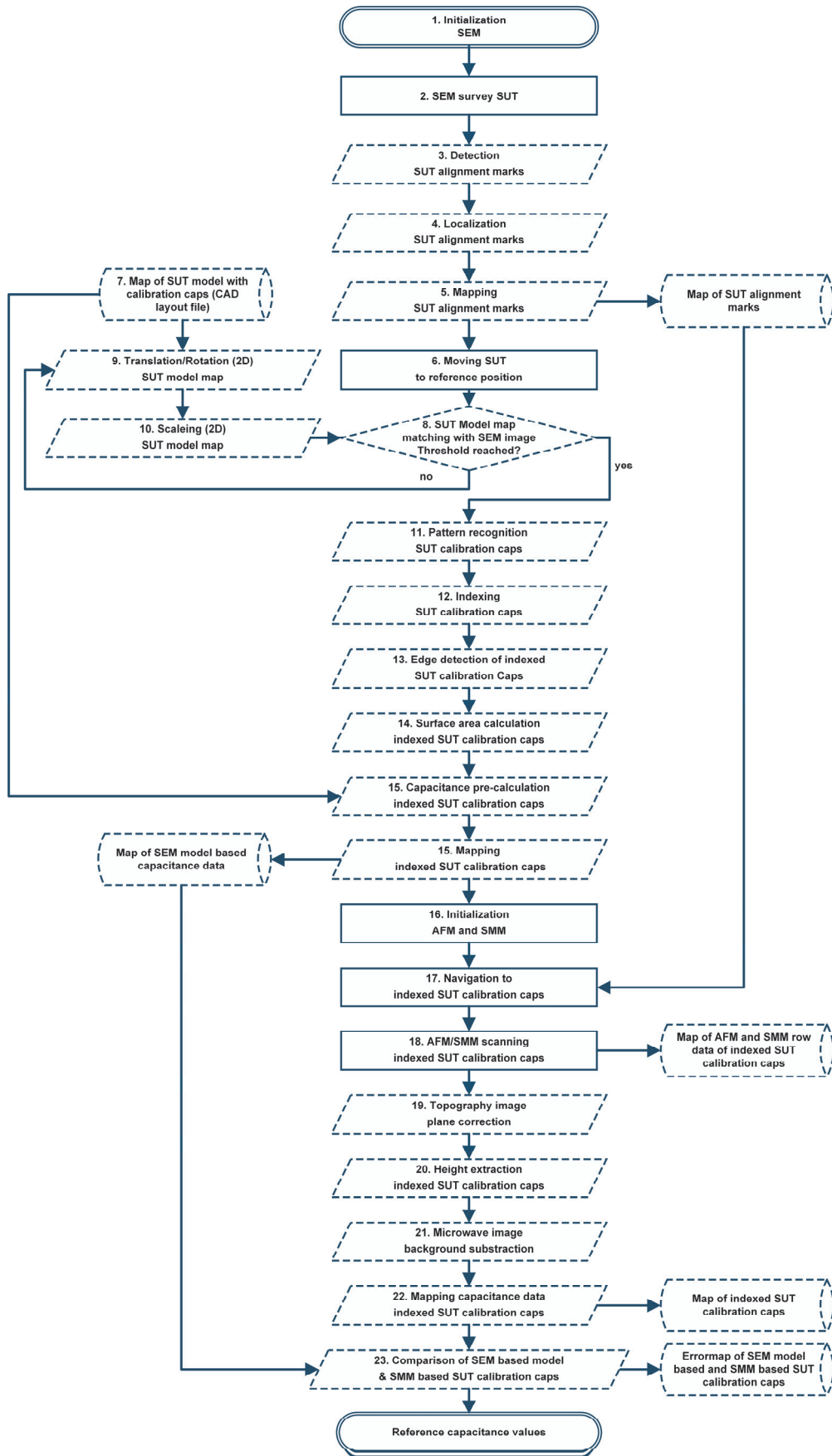


Figure 4-14 Flowchart of a vision-based robotic SMM calibration routine of micro-scale capacitors.

## 4.5 System Validation

The validation of the demonstrator in its entirety was carried out on the basis of various samples, which can be found in the following sections.

### 4.5.1 Multimodal Test Standard

In order to validate the full functionality with all microscope modalities of the technology demonstrator SEM<sup>2</sup>, a multimodal test standard was designed (see 4.4.1), which has been measured in the following. The standard incorporated, in addition to the microscale capacitors in the center for the SMM study, alignment and finding structures for light and electron microscopy and for image-based robotic navigation (Haenssler et al. 2017).

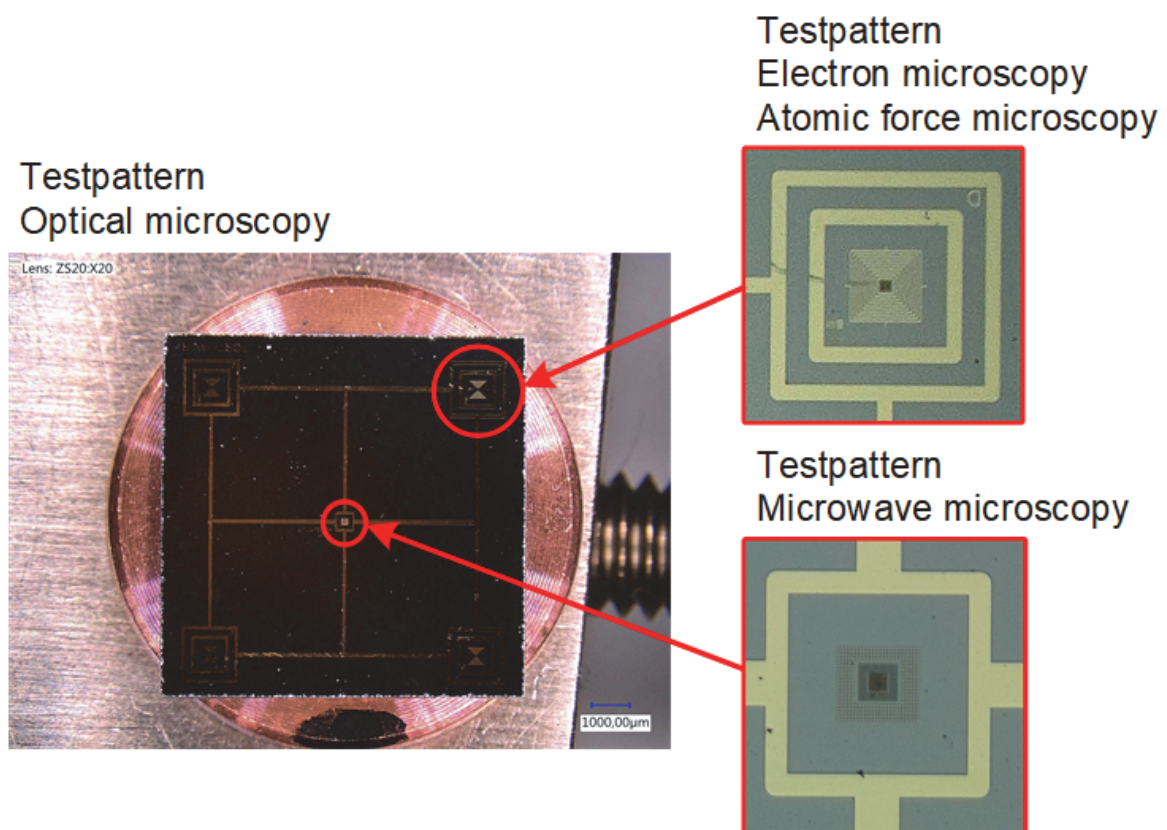


Figure 4-15 Microphotograph of fabricated Multimodal Test Standard mounted on an SEM stub. Right: Zoomed images of features for electron, atomic force and microwave microscopy.

By using this multimodal test sample, one may assist in electron microscopy mode the adjustment of the magnification, which has typical errors in the range of 5% to 10%, and the astigmatism. The demonstrator operated in contact mode under high vacuum conditions ( $7 \times 10^{-6}$  mbar). Due to the limitation of the AFM-Scanner stage of  $5 \mu\text{m} \times 5 \mu\text{m} \times 5 \mu\text{m}$  in 3D space, the maximum area of measurement is restricted. The following electron microscope image shows the capacitor structures for SMM of the test standard, while it is scanned with the probe to be seen at lower left. A close-up of one  $4 \mu\text{m}$  capacitor on the right-hand side of Figure 4-16 shows a slight surface roughness, which will be explored in more detail later. Scanning

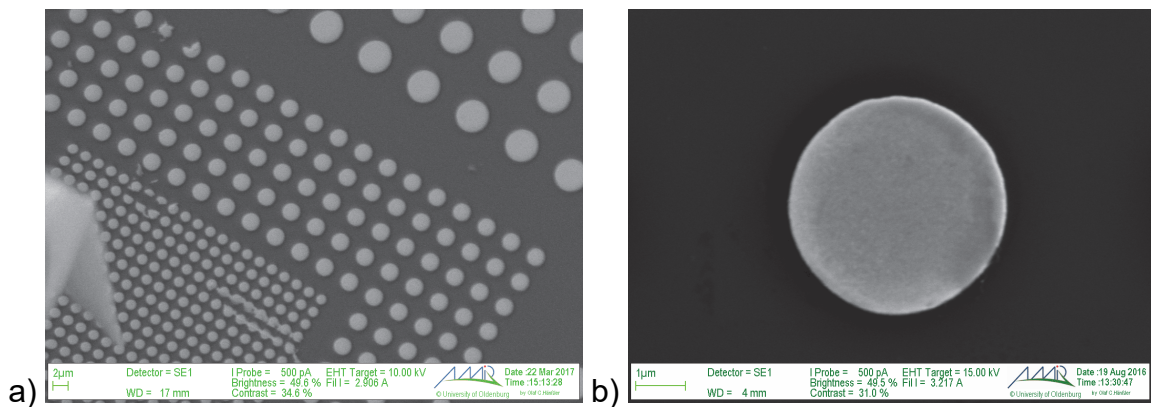


Figure 4-16 SEM micrograph of a) cantilever with the SMM test features while scanning and b) micro-scaled capacitor. Scale bar on the left  $2 \mu\text{m}$  and on the right  $1 \mu\text{m}$ .

was done by 1 line/s at a resolution of  $128 \times 128$  pixel and an intermediate frequency bandwidth of 1 kHz. The smallest fabricated capacitors (target diameter  $1.5 \mu\text{m}$ ) are showing topography differences in diameter and top flatness. As a reference, the capacitors were studied with a commercial JPK NanoWizard® AFM (Figure 4-17 (b)). It works under ambient condition and probes with a different cantilever (Tap300 / Budget Sensors®), having doubled high-spring constant of 40 N/m in regards to the near-field microwave probe cantilever with 18 N/m.

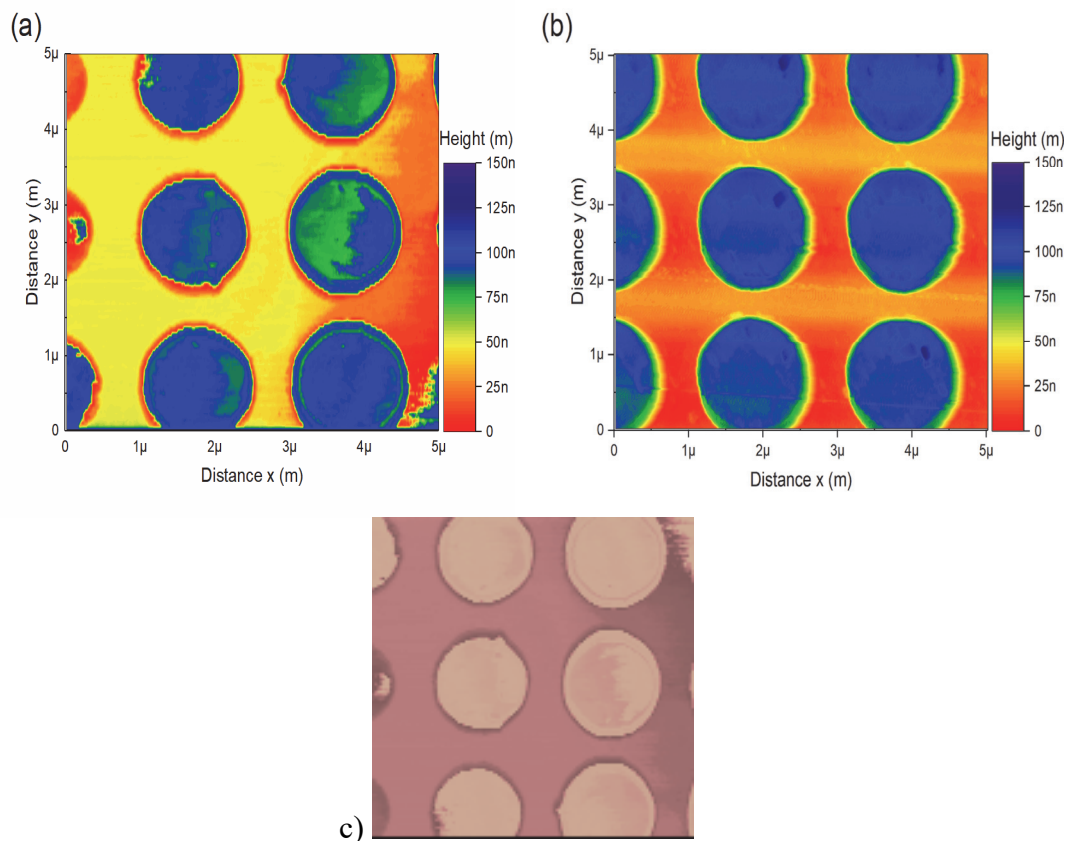


Figure 4-17 Spatial distribution of topography by (a) SEM<sup>2</sup> and (b) JPK NanoWizard AFM. Data manipulation by Gwyddion: Mean plane subtraction and line-by-line matching of height median. c) Live OAF vision output.

The figure shows the spatial distribution of topography of two different areas of a total array of 21 \* 21 capacitors with 1.5 μm diameter. Topography line profiles of two capacitors (Figure 4-17: both lower right capacitors) yields to physical dimensions between 1.5 μm to 1.7 μm in diameter and 125 nm in height. Due to differences in height, the results of the SEM<sup>2</sup> are corrected by a factor of 1.3, matching the height of 125 nm given by the commercial AFM measurement as a reference height. The top plateau swale varies up to 40 nm (Figure 4-18) for different capacitors and this cannot be determined directly in SEM. For this purpose, the SEM would have to be equipped with a focused ion beam unit, and then it is possible to conduct a destructive section through the capacitor using ion etching.

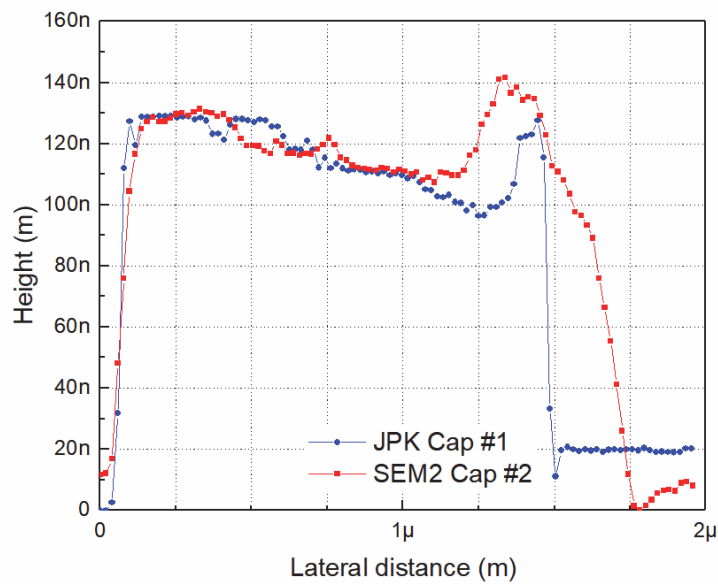


Figure 4-18 Topography line scan of two different microcapacitors with SEM<sup>2</sup> (red) and JPK NanoWizard (blue). Variations in diameter and top plate roughness are observable.

In the microwave regime, changes in complex impedance on the top were detected, by measuring the reflection coefficient with the near-field microwave probe and the VNA (Figure 4-19). The power output of the VNA leveled to 0 dBm at all measurements. An electric interferometric approach, by using an optional feature in the VNA of differential signaling, resulted in sensitivity enhancement at a limited number of single interference frequencies. The separation of these repeating interferences are 72.6 MHz. The measurement path to the probe is one part of the internal differential signal and unchanged. The second differential signal part represent the reference path of the interferometer. This signal is internally attenuated by 1.84 dB and shifted in phase, quantified by the VNA software to an virtual electrical length of 37  $\mu\text{m}$ , in order to obtain a sharp minimum, while being at 1  $\mu\text{m}$  height above the sample surface. Scanning over the 1.5  $\mu\text{m}$  capacitors at 4.769 GHz reveals a downshift of the interference frequency of 315 kHz. This leads on the other hand, to an increase of 12 dB magnitude of  $S_{11}$  at the fixed measurement frequency during the scan. At 9.996 GHz it was

found at the same capacitor area a shift of 866 kHz, but the magnitude  $S_{11}$  increased only up to 2 dB of the interference minimum of -42 dB. As mentioned before by simulation, the maximum working frequency of the near-field probe is 7 GHz therefore the sensitivity is reduced.

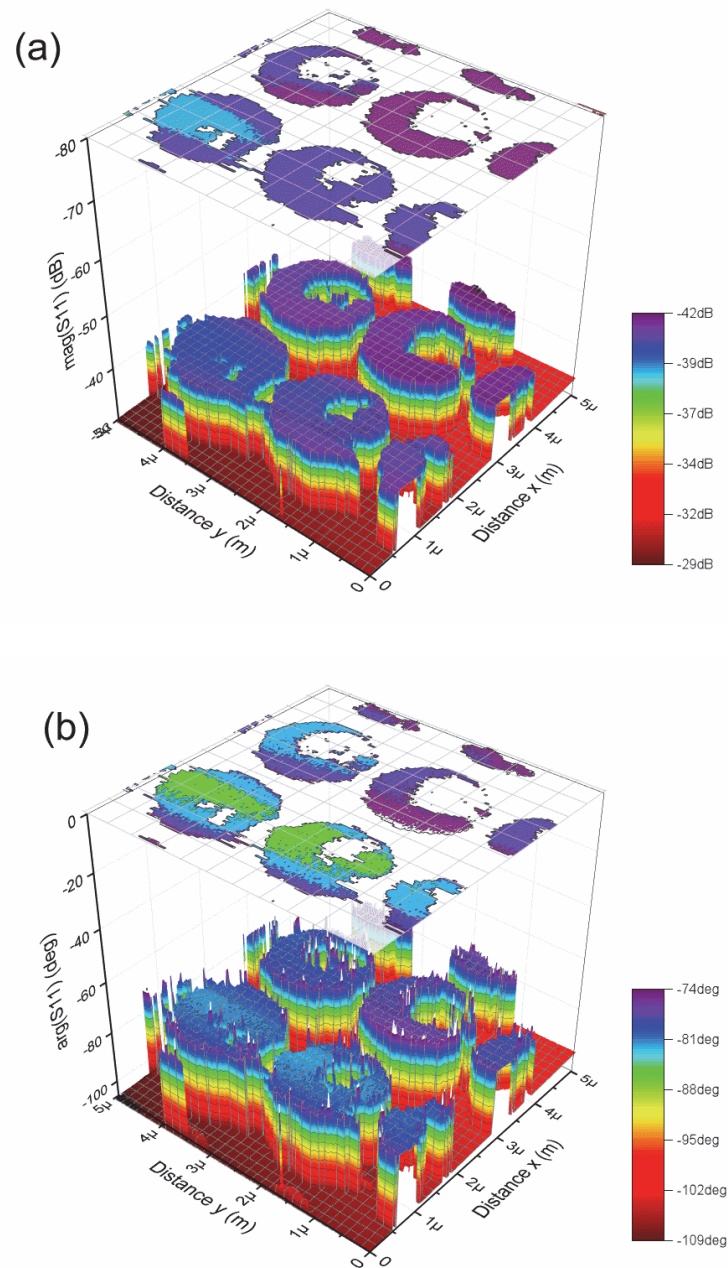


Figure 4-19 3D color and top projection contour map of (a) magnitude and (b) phase of reflection coefficient  $S_{11}$  measured by SEM<sup>2</sup> at 4.8 GHz of an area with 1.5  $\mu$ m capacitors. Data manipulation: Mean plane subtraction.

In two microscope modalities, AFM topography and electromagnetic microwave properties, it can be seen that the top plate part of the fabricated capacitors features strong imperfections in terms of roughness. Exemplarily measured at one capacitor, the depression on top found to be in magnitude( $S_{11}$ )  $\approx 0.5$  dB and phase  $\arg(S_{11}) \approx 4$  deg at 4.8 GHz (Figure 4-20). The electrical roughness can be separated in two parts: (i) the contribution of the topography roughness, that may change the parasitic stray capacitance between the probe and ground and (ii) for the same height, the different contributions of the stray capacitance originating from the top electrode and from the rest of the sample. While moving the probe over the top plate in contact, the

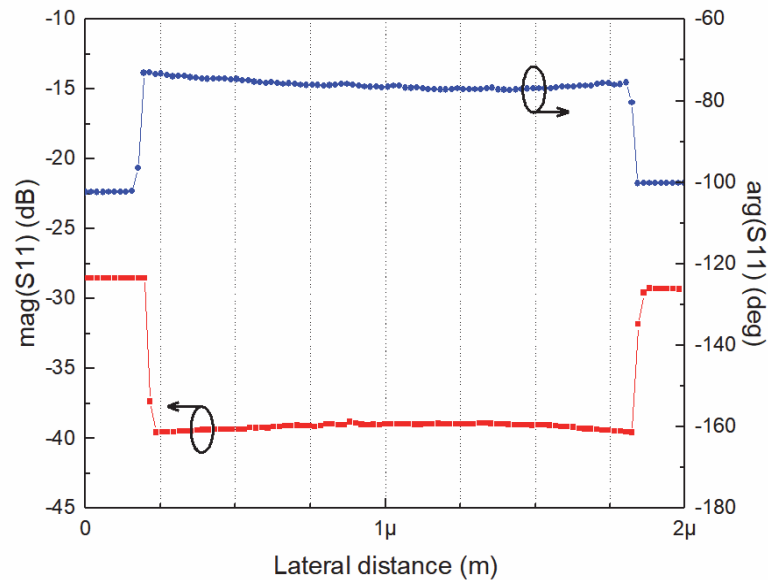


Figure 4-20 Microwave sectional profile measured by  $SEM^2$  at 4.8 GHz of one microcapacitor. Magnitude and phase of S-Parameter  $S_{11}$ .

parasitic capacitance between top electrode and ground decreases. The electric field is partially screened by the top plate electrode and while scanning, this screening effect is at maximum, near the center of the not perfect round top electrode.

### 4.5.2 Memristor

Memristors are innovative memory devices that belong to the family of Resistive Random Access Memory (RRAM) with switching dynamics in the GHz range and are seen as a future alternative to current technologies such as flash memory or DRAMs (Torrezan et al. 2011). In the framework of the French-German project VACSMM, such a device based on  $\text{TiO}_2$  was designed (Sassine et al. 2016). For the SEM<sup>2</sup> setup, a modified smaller version of this sample was produced and includes additional 2 \* 3 MOS capacitors for on-wafer calibration (see Figure 4-21).

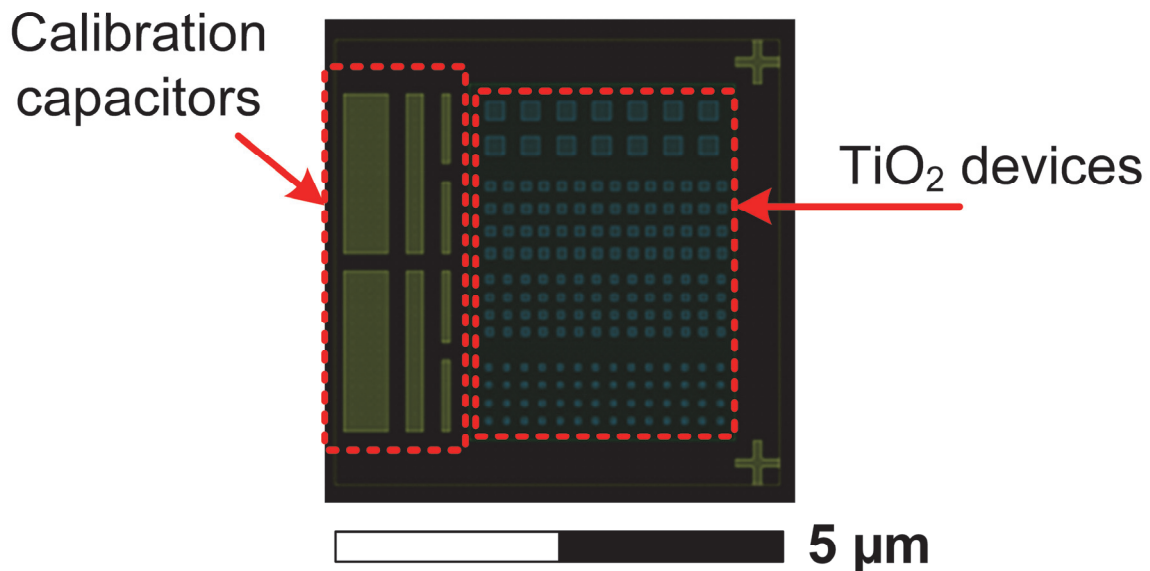


Figure 4-21 CAD Sketch of a Memristor sample fabricated by IEMN for the SEM<sup>2</sup> setup.

The elements to be investigated consist of Ti (thickness  $t=5$  nm)/Pt ( $t=30$  nm)/ $\text{TiO}_{2-x}$ /TiO<sub>2</sub>- $x$ /TiO<sub>2</sub>/Pt ( $t=15$  nm)/Au ( $t=20$  nm) from bottom to top deposited on a p-type silicon substrate of 1-3  $\Omega\text{cm}$  resistivity. The edge lengths of the rectangular memory components are designed with 200 nm, 100 nm, 80 nm and 60 nm. The scanning resolution was 512 points over 5  $\mu\text{m}$  by 5  $\mu\text{m}$  range. The microwave source was set to 3 dBm power and the measurement frequency

to 4.82336 GHz, with an intermediate bandwidth of 1 kHz of the VNA receiver. The reflection coefficient  $S_{11}$  measurement was undertaken in a direct manner without interferometry.

The AFM scan image shows a weak contrast of the calibration capacitor bars or their gold layer, which shows a thickness of about 7 nm (blue area in Figure 4-22). The 200 nm large Memristors are barely discernible in the light red area. Their heights are around 5 nm. The smaller components (100 nm, 80 nm and 60 nm) are not identifiable in the topography. In the scan image of the reflection coefficient, on the other hand, the calibration capacitors, the 100 nm and 80 nm structures and partly also some single 60 nm components can be recognized. The  $S_{11}$  magnitude values range between 0.1 dB for the 200 nm and 0.01 dB for the 60 nm Memristors. It is assumed that problems occurred during the production process. Further tests will be conducted.

The validation of the functionality of this sample as a memory device was not in the foreground, but it is demonstrated that, through the use of microwave microscopy another option besides AFM and SEM for identification and subsequent characterization exists.

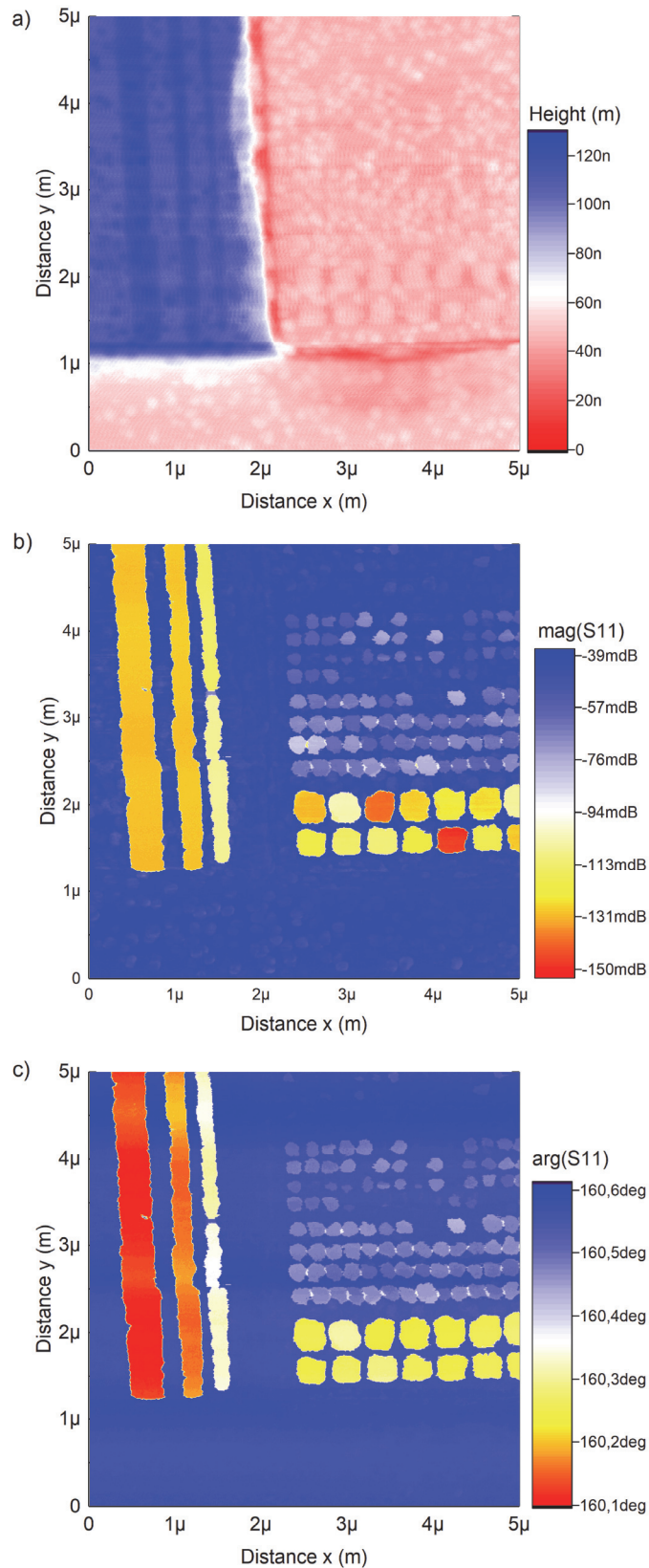
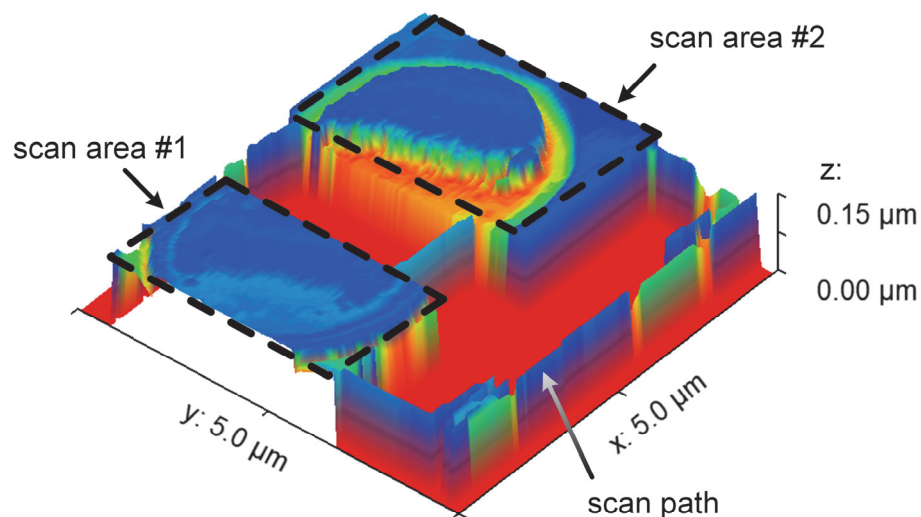


Figure 4-22 2D maps of (a) topography, (b) magnitude and (c) phase of reflection coefficient  $S_{11}$  of memristor devices measured by  $SEM^2$  at 4.8 GHz. Data manipulation: Plane level and 3-point fitting, Align rows median.

### 4.5.3 Non-raster Trajectory Scanning

A non-raster scanning technique enhances the imaging speed of SPM. Trajectories such as Archimedean spirals (Mahmood, Moheimani 2009; Mahmood et al. 2011), cycloids (Yong et al. 2010) or Lissajous-like patterns (Bazaei et al. 2012) has been proposed and compared with sawtooth-/staircase-like raster scanning. In 2005 the author of this thesis was granted a European patent for detecting contact forces with its application as a piezo-touchdown sensor on the microscale based on cycloid scanning (Haenssler et al. 2005).

An opening of the multimodal imaging technology to high-speed scanning force microscopy is a one aspect of this work. A software implementation of such an approach in the AFM/SMM-Controller has been undertaken (contribution of M. Wieghaus). The following Figure 4-23 depicts one scan composing of a mixture of two rectangular scan areas over two microcapacitors as region-of-interests with connecting scan paths as a proof-of-concept.



*Figure 4-23 3D view of a topography scan of two micro-scaled capacitors based on non-raster scan option of the AFM/SMM-Controller. Two rectangular region-of-interests #1 and #2 and arbitrary lines as scan trajectories.*

It should be noted, that non-raster trajectories, whose waveforms haven't such high-order spectral harmonics as sawtooth or triangle scan signals, allows for faster scanning than the latter mentioned exciting waveforms, because the mechanical cut-off frequency of the positioning stage is limiting the performance. Existing SPM instrumental setups are easily modifiable with such technique.

## 4.6 Summary

A hybrid technology integrating several microscopy modalities gaining multiple information of sample surfaces by detection of light, electron, atomic force and microwave interaction is proposed. A study of microscale capacitors evaluated an instrumental platform, showing the potential of this multimodal technology.

A multimodal test standard consisting of various features for the different microscopy techniques used here has been introduced. Microwave microscopy uses calibration standards consisting of microscale capacitors. An analysis and a new approximation formula for round MOS capacitors was introduced, which now also takes the fringing effect into account. Capacitance values in the calculated area of 380 aF, showed strong contrast proofing the concept. Smaller scaled features weren't available at the time of preparation. Future work will focus on quantified SMM measurements by utilizing a modeling and de-embedding process (Michalas et al. 2015) and using calibration methods with known capacitor values (Karbassi et al. 2008; Wu, Yu 2010) or different heights respectively (Fabiani et al. 2011). The above-mentioned considerations focuses on a single microcapacitor. If dense arrays of nanoscale capacitors such as the so-called nanodots are investigated, inter-resistive and inter-capacitive links are built between. A reference to this can be found in the reference (Basu et al. 2004), in which an analytical model is developed.

Robotics and automation make it possible to combine such complex individual system components into innovative systems. Through open system architectures, the problems that exist in semiconductor research, material and biological science in characterizing and optimizing complex conductivity of hetero structure materials, electron-charge- and electron-spin-based devices, bioinspired objects, magneto-resistive functionalized items, and superconductor-based devices amongst other areas of applications, can be better tackled rather

than through closed proprietary technology approaches. By using this open-source approach, the research community will be able to share additional instruments, drivers and software algorithms for free access. For example, the Tampere University of Technology utilizes this software framework OAF for the mechanical analysis of fibrous materials. A coupling of the microscope technology presented here, with a test setup for the mechanical characterization of cellulosic material in the SEM, can be realized in such a robotic environment, despite a wide variety of equipment hardware such as a nanopositioned micro actuator, micro force sensor, SMM, electrical 4-point probe measurements by an semiconductor device analyzer. This moves in the direction of a technology which, with multimodal or correlative microscopy and nano-fabrication and -modification techniques, will be a tool for semiconductors research and materials science.

## 5 CONCLUSION AND FUTURE DIRECTIONS

The hybrid technology, devised herein has successfully demonstrated that it can extract multiple complex information of nanoscale samples. This was achieved by integrating and fusing different microscopic modalities, such as infrared light, electron, atomic force and near-field microwave.

By introducing an electron microscope into microwave microscopy it has been shown that it is possible to perform the positioning of the probe tip and the navigation of the sample-under-test in live operation. The resolution limit of optical microscopes which are used for SMM and are typically in the range of 1.5  $\mu\text{m}$  to 2.5  $\mu\text{m}$ , commonly used for this purpose, has been overcome by the introduction of electron microscopy. The SEM, used in this work, has a resolution of 100 nm due to the setup construction and the resulting large working distance of approx. 18 mm between the electron gun and the sample. With the presented setup it is possible to analyze inorganic samples. A small-size interferometer based AFM, which supplies the height information as a control parameter for steering the SMM scan, is purely optical and does not introduce any electromagnetic disturbing radiation into the area of measurement. The infrared light ray that is directed and reflected onto the cantilever, must be narrowly focused so as not to influence by a light spill-over, optically sensitive objects. Ultimately, every light illuminating a p-n junction produces a photocurrent and changes the measurement result in the microwave microscopic modality. The laser spot size of the AFM is 50  $\mu\text{m}$  and adapted to the RMN cantilever, which has a width of 110  $\mu\text{m}$ . The SEM<sup>2</sup> probe head can be later positioned in the vacuum chamber by means of a piezo system if the initial position settings have changed. This system, can also be installed in SEM's other manufacturers after slight modifications.

In order to be ready for future expansions in the direction of frequencies of 100 GHz, two models of sample probe heads are available. Full-wave 3D electro-magnetic FEM analyses, which now cover not only the cantilever-tip-sample system (Oladipo et al. 2013), but also the path via the cantilever substrate until the connector, can now contribute to the understanding of parasitic effects respectively to the reduction of them. These have an enormous influence on the measurements in SMM. The models can be utilized for other cantilever and SMM implementations by modifications.

The research on the measurement of tiny impedance changes on the nanoscale is still in its beginning. An improved type of an electrical interferometer with a higher signal-to-noise ratio respectively a quality of factor two, can have a decisive influence on the result in some situations. Here too, the Friis noise formula applies that measurement should take place as close to the object as possible, and if this is not practicable, an amplifier should overcome the necessary sensitivity hurdle. Future measurement tasks will benefit considerably if an integrated solution, i.e. a fully integrated sensing head with probe, on-board self-/remote controlled interferometer with amplifier, is available.

At present, a wide use of microwave microscopy is restricted by the fact that, among other things, it is quite complex and therefore expensive in terms of equipment. However, in order to disseminate the technology, smaller measuring units are necessary which makes it possible to operate without the use of scanning electron microscopy, of course to the disadvantage of limited functionality. One step in this direction is to use commercial conductive self-sensing AFM probes which have to be optimized for microwave transmission [see Figure 5-1 a)]. This and MEMS-based SMM solutions have in common the need of a coarse positioning unit to move the sample, an imaging system for observation of the scanning process and a vector network analyzer or six-port reflectometer. Figure 5-1 b) shows a prototype of a Miniature

Microwave Materials Analyzer for future research and industry-related applications. Also an operation in a low vacuum SEM is an option for the future for studies on biological samples without charging effects.

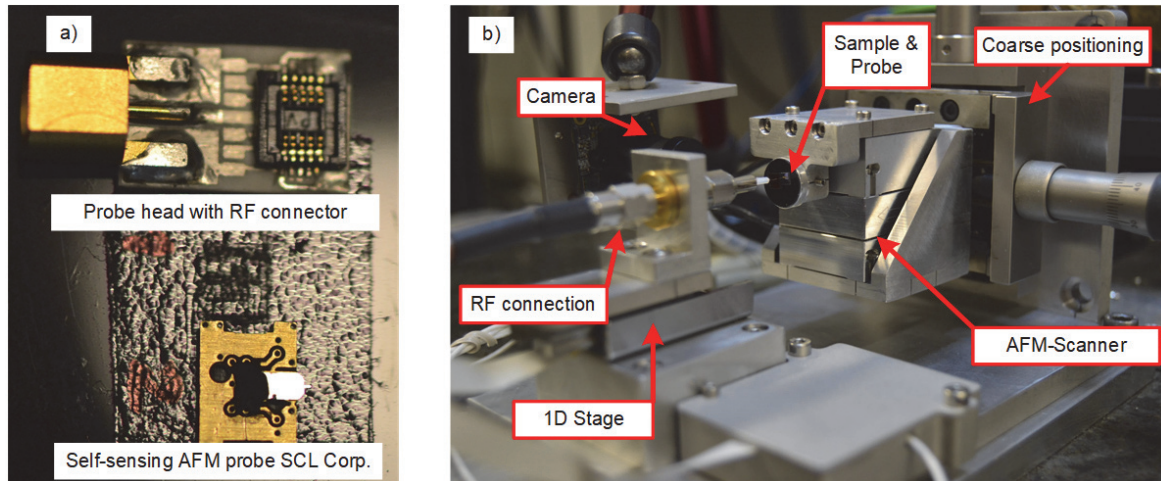


*Figure 5-1 Photographs of prototypes: a) Self-sensing near-field probe consisting of the probe and the probe head PCB. b) Miniature Microwave Materials Analyzer showing a scanning stage.*

For technologies that gather cross-dimensional information on the one hand and extract data from the same sample volume using different modalities on the other, comprehensive calibration is required. Joint analysis of multidimensional microscopic data sets is mandatory to enhance the calibration quality to obtain quantified data, not only in near-field microwave probing. A step towards a test standard linking the “classic” microscopy modii with microwave and nanorobotics as used in this research is initiated. On this way, a new approximation formula for micro-scaled round capacitors and their fringing fields is developed. The addition of calibration structures with dopant steps, in conjunction with the increase in resolution and accuracy, is one of the short-term implementation requirements in the development of a new multimodal test standard. A look into the future of this technology and SPM technology in general promises, that multidimensionality does widen the knowledge about materials, but this leads on the other hand to Big-Data challenges (Kalinin et al. 2016). These can be solved by employing Machine Learning (ML) methods.

Vision-based open-source robotics and automation on the nanoscale, enables future additional methods to extend the knowledge of samples and materials, to tool SPM probes and to manipulate nanoobjects. Arbitrary scanning trajectories, free programmable with the own-designed AFM/SMM-controller, will result in localized sample-specific dynamic data densities from the region-of-interest. Spectroscopic imaging, using voltage or frequency as two examples, with the support of adaptive image processing methods, will allow for extracting in deep the properties of novel materials. The technology platform "Scanning electron, force and microwave microscope", which is embedded in an open-source robotics software framework, provides a basis for all these above mentioned methods and applications. It aims to provide a tool for the community in the fields of semiconductors, materials science and life sciences.

## 6 PUBLICATION BIBLIOGRAPHY

Anderson, G. (2013): Scanning Microwave Microscopy for Nanoscale Electrical Characterization. In *Micros. Today* 21 (06), pp. 32–36. DOI: 10.1017/S1551929513000965.

Angelov, T.; Ahmad, A.; Guliyev, E.; Reum, A.; Atanasov, I.; Ivanov, T. et al. (2016): Six-axis AFM in SEM with self-sensing and self-transduced cantilever for high speed analysis and nanolithography. In *Journal of Vacuum Science & Technology B, Nanotechnology and Microelectronics: Materials, Processing, Measurement, and Phenomena* 34 (6), 06KB01. DOI: 10.1116/1.4964290.

Anlage, S. M.; Steinhauer, D. E.; Feenstra, B. J.; Vlahacos, C. P.; Wellstood, F. C. (2001): Near-Field Microwave Microscopy of Materials Properties. In Harold Weinstock, Martin Nisenoff (Eds.): *Microwave Superconductivity*. Dordrecht: Springer Netherlands, pp. 239–269.

Ash, E. A.; Nicholls, G. (1972): Super-resolution Aperture Scanning Microscope. In *Nature* 237 (5357), pp. 510–512. DOI: 10.1038/237510a0.

Attocube Corp.: attoAFM I. low temperature atomic force microscope, cantilever based. Available online at <http://www.attocube.com/!trash/attoafmiold/>, checked on 10/28/2017.

Azizi, M.; Sarkar, N.; Mansour, R. R. (2013): Single-Chip CMOS-MEMS Dual Mode Scanning Microwave Microscope. In *IEEE Trans. Microwave Theory Techn.* 61 (12), pp. 4621–4629. DOI: 10.1109/TMTT.2013.2288222.

Banerjee, A. G.; Gupta, S. K. (2013): Research in Automated Planning and Control for Micromanipulation. In *IEEE Trans. Automat. Sci. Eng.* 10 (3), pp. 485–495. DOI: 10.1109/TASE.2013.2260539.

Barke, E. (1988): Line-to-ground capacitance calculation for VLSI. A comparison. In *IEEE Trans. Comput.-Aided Des. Integr. Circuits Syst.* 7 (2), pp. 295–298. DOI: 10.1109/43.3160.

Bartenwerfer, M.; Eichhorn, V.; Jasper, D.; Fatikow, S.; Savenko, A.; Petersen, D. H. et al. (2011): Automated handling and assembly of customizable AFM-tips. In : Proc. of 2011 IEEE Int. Symp. on Assembly and Manufacturing (ISAM). Tampere, Finland, 25.05.-27.05. IEEE. Piscataway, NJ: IEEE, pp. 1–6.

Basu, A.; Lin, Sheng-Chih; Wasshuber, C.; Ionescu, A. M.; Banedee, K. (2004): A comprehensive analytical capacitance model of a two dimensional nanodot array [cellular neural net application]. In : Proc. of 5th Int. Symp. on Quality Electronic Design, 2004. San Jose, CA, USA, 22-24 March 2004. Los Alamitos, Calif.: IEEE Computer Society, pp. 259–264.

Batra, R. C.; Porfiri, M.; Spinello, D. (2006): Electromechanical Model of Electrically Actuated Narrow Microbeams. In *J. Microelectromech. Syst.* 15 (5), pp. 1175–1189. DOI: 10.1109/JMEMS.2006.880204.

Bazaei, A.; Yong, Yuen K.; Moheimani, S. O. Reza (2012): High-speed Lissajous-scan atomic force microscopy: scan pattern planning and control design issues. In *Rev Sci Instrum* 83 (6), p. 63701. DOI: 10.1063/1.4725525.

Berweger, S.; Blanchard, P. T.; Brubaker, M. D.; Coakley, K. J.; Sanford, N. A.; Wallis, T. M. et al. (2016): Near-field control and imaging of free charge carrier variations in GaN nanowires. In *Appl. Phys. Lett.* 108 (7), p. 73101. DOI: 10.1063/1.4942107.

Berweger, S.; Weber, J. C.; John, J.; Velazquez, J. M.; Pieterick, A.; Sanford, N. A. et al. (2015): Microwave near-field imaging of two-dimensional semiconductors. In *Nano letters* 15 (2), pp. 1122–1127. DOI: 10.1021/nl504960u.

- Biagi, M. C.; Fabregas, R.; Gramse, G.; van der Hofstadt, M.; Juárez, A.; Kienberger, F. et al. (2016): Nanoscale Electric Permittivity of Single Bacterial Cells at Gigahertz Frequencies by Scanning Microwave Microscopy. In *ACS Nano* 10 (1), pp. 280–288. DOI: 10.1021/acsnano.5b04279.
- Black, R. C.; Wellstood, F. C.; Dantsker, E.; Miklich, A. H.; Nemeth, D. T.; Koelle, D. et al. (1995): Microwave microscopy using a superconducting quantum interference device. In *Appl. Phys. Lett.* 66 (1), pp. 99–101. DOI: 10.1063/1.114159.
- Boer, P. de; Hoogenboom, J. P.; Giepmans, B. N. G. (2015): Correlated light and electron microscopy: ultrastructure lights up! In *Nature methods* 12 (6), pp. 503–513. DOI: 10.1038/nmeth.3400.
- Bolorizadeh, M.; Panteleit, F.; Hitzel, F. (2013): New Revolutionary Hybrid SEM by Carl Zeiss. In *Microsc Microanal* 19 (S2), pp. 1300–1301. DOI: 10.1017/S1431927613008490.
- Bradski, G. (2000): The OpenCV Library. In *Dr. Dobb's Journal: Software Tools for the Professional Programmer* 25 (11), pp. 120–123.
- Brinciotti, E.; Campagnaro, G.; Badino, G.; Kasper, M.; Gramse, G.; Tuca, S. S. et al. (2016): Frequency Analysis of Dopant Profiling and Capacitance Spectroscopy using Scanning Microwave Microscopy. In *IEEE Trans. Nanotechnology*, p. 1. DOI: 10.1109/TNANO.2016.2628206.
- Burke, P. J. (2002): Luttinger liquid theory as a model of the gigahertz electrical properties of carbon nanotubes. In *IEEE Trans. Nanotechnology* 1 (3), pp. 129–144. DOI: 10.1109/TNANO.2002.806823.
- C. Gao and X.-D. Xiang (1998): Quantitative microwave near-field microscopy of dielectric properties. In *Rev. Sci. Instrum.* 69 (11), pp. 3846–3851. DOI: 10.1063/1.1149189.

Caplan, J.; Niethammer, M.; Taylor, R. M.; Czymmek, K. J. (2011): The power of correlative microscopy: multi-modal, multi-scale, multi-dimensional. In *Current opinion in structural biology* 21 (5), pp. 686–693. DOI: 10.1016/j.sbi.2011.06.010.

Carlson, K.; Andersen, K. N.; Eichorn, V.; Petersen, D. H.; Mølhave, K.; Bu, I. Y. Y. et al. (2007): A carbon nanofibre scanning probe assembled using an electrothermal microgripper. In *Nanotechnology* 18 (34), p. 345501. DOI: 10.1088/0957-4484/18/34/345501.

Carpick, R. W.; Salmeron, M. (1997): Scratching the Surface. Fundamental Investigations of Tribology with Atomic Force Microscopy. In *Chem. Rev.* 97 (4), pp. 1163–1194. DOI: 10.1021/cr960068q.

Chang, W. H. (1976): Analytical IC Metal-Line Capacitance Formulas (Short Papers). In *IEEE Trans. Microwave Theory Techn.* 24 (9), pp. 608–611. DOI: 10.1109/TMTT.1976.1128917.

Cho, Y.; Kirihara, A.; Saeki, T. (1996): Scanning nonlinear dielectric microscope. In *Rev. Sci. Instrum.* 67 (6), pp. 2297–2303. DOI: 10.1063/1.1146936.

Chuang, W.-C.; Wang, C.-W.; Chu, W.-C.; Chang, P.-Z.; Hu, Y.-C. (2012): The fringe capacitance formula of microstructures. In *J. Micromech. Microeng.* 22 (2), p. 25015. DOI: 10.1088/0960-1317/22/2/025015.

Chung, K.-H.; Lee, Y.-H.; Kim, D.-E. (2005): Characteristics of fracture during the approach process and wear mechanism of a silicon AFM tip. In *Ultramicroscopy* 102 (2), pp. 161–171. DOI: 10.1016/j.ultramic.2004.09.009.

Chusseau, L.; Payet, P.; Raoult, J. (2016): Millimeter wave near-field imagery with micrometer spatial resolution. In : 2016 41st Int. Conf. on Infrared, Millimeter, and Terahertz Waves (IRMMW-THz). 25-30 Sept. 2016. 2016 41st Int. Conf. on Infrared, Millimeter, and Terahertz waves (IRMMW-THz). Copenhagen, Denmark. Piscataway, NJ: IEEE, pp. 1–2.

Cocker, T. L.; Jelic, V.; Gupta, M.; Molesky, S. J.; Burgess, J. A. J.; Reyes, G. D.L. et al. (2013): An ultrafast terahertz scanning tunnelling microscope. In *Nature Photon* 7 (8), pp. 620–625. DOI: 10.1038/nphoton.2013.151.

Dargent, T.; Haddadi, K.; Lasri, T.; Clément, N.; Ducatteau, D.; Legrand, B. et al. (2013): An interferometric scanning microwave microscope and calibration method for sub-fF microwave measurements. In *Rev Sci Instrum* 84 (12), p. 123705. DOI: 10.1063/1.4848995.

Diederichs, C.; Bartenwerfer, M.; Mikczinski, M.; Zimmermann, S.; Tiemerding, T.; Geldmann, C. et al. (2013): A rapid automation framework for applications on the micro-and nanoscale. In : Australasian Conference on Robotics and Automation (ACRA). University of New South Wales, Sydney, December. Australian Robotics and Automation Association, p. 8.

Elmasry, M. I. (1982): Capacitance calculations in MOSFET VLSI. In *IEEE Electron Device Lett.* 3 (1), pp. 6–7. DOI: 10.1109/EDL.1982.25454.

Erlandsson, R. (1988): Atomic force microscopy using optical interferometry. In *J. Vac. Sci. Technol. A* 6 (2), p. 266. DOI: 10.1116/1.575440.

Ermakov, A. V.; Garfunkel, E. L. (1994): A novel AFM/STM/SEM system. In *Rev. Sci. Instrum.* 65 (9), p. 2853. DOI: 10.1063/1.1144627.

Estep, N. A.; Sounas, D. L.; Soric, J.; Alù, A. (2014): Magnetic-free non-reciprocity and isolation based on parametrically modulated coupled-resonator loops. In *Nat Phys* 10 (12), pp. 923–927. DOI: 10.1038/nphys3134.

EU FP7 ICT NANO-TEC (2013): Recommendations for the Technology-Design. Ecosystem for Nanoelectronics. With assistance of J. Ahopelto, A. Cappy, G. Fagas, P. Grabić, M. Graef, G. Larrieu et al. Edited by C.M. Sotomayor Torres. Nano-Tec. Barcelona, Spain. Available online at <https://www.fp7-nanotec.eu/content/now-online-recommendations-technology-design-ecosystem-nanoelectronics>, checked on 9/25/2017.

Fabiani, S.; Mencarelli, D.; Di Donato, A.; Monti, T.; Venanzoni, G.; Morini, A. et al. (2011): Broadband Scanning Microwave Microscopy investigation of graphene. In : 2011 IEEE/MTT-S International Microwave Symposium - MTT 2011. Baltimore, MD, USA, pp. 1–4.

Farina, M.; Di Donato, A.; Monti, T.; Pietrangelo, T.; Da Ros, T.; Turco, A. et al. (2012): Tomographic effects of near-field microwave microscopy in the investigation of muscle cells interacting with multi-walled carbon nanotubes. In *Appl. Phys. Lett.* 101 (20), p. 203101. DOI: 10.1063/1.4767518.

Farina, M.; Lucesoli, A.; Pietrangelo, T.; Di Donato, A.; Fabiani, S.; Venanzoni, G. et al. (2011a): Disentangling time in a near-field approach to scanning probe microscopy. In *Nanoscale* 3 (9), pp. 3589–3593. DOI: 10.1039/C1NR10491H.

Farina, M.; Mencarelli, D.; Di Donato, A.; Venanzoni, G.; Morini, A. (2011b): Calibration Protocol for Broadband Near-Field Microwave Microscopy. In *IEEE Trans. Microwave Theory Techn.* 59 (10), pp. 2769–2776. DOI: 10.1109/TMTT.2011.2161328.

Ferrier, G. A.; Romanuik, S. F.; Thomson, D. J.; Bridges, G. E.; Freeman, M. R. (2009): A microwave interferometric system for simultaneous actuation and detection of single biological cells. In *Lab on a chip* 9 (23), pp. 3406–3412. DOI: 10.1039/b908974h.

Fukushima, K.; Saya, D.; Kawakatsu, H. (2000): Development of a Versatile Atomic Force Microscope within a Scanning Electron Microscope. In *Jpn. J. Appl. Phys.* 39 (Part 1, No. 6B), pp. 3747–3749. DOI: 10.1143/JJAP.39.3747.

Gao, C.; Wei, T.; Duewer, F.; Lu, Y.; Xiang, X.-D. (1997): High spatial resolution quantitative microwave impedance microscopy by a scanning tip microwave near-field microscope. In *Appl. Phys. Lett.* 71 (13), pp. 1872–1874. DOI: 10.1063/1.120444.

Gates, R. S.; Pratt, J. R. (2012): Accurate and precise calibration of AFM cantilever spring constants using laser Doppler vibrometry. In *Nanotechnology* 23 (37), p. 375702. DOI: 10.1088/0957-4484/23/37/375702.

Golosovsky, M.; Galkin, A.; Davidov, D. (1996): High-spatial resolution resistivity mapping of large-area YBCO films by a near-field millimeter-wave microscope. In *IEEE Trans. Microwave Theory Techn.* 44 (7), pp. 1390–1392. DOI: 10.1109/22.508246.

Golosovsky, M.; Maniv, E.; Davidov, D.; Frenkel, A. (2002): Near-field of a scanning aperture microwave probe: a 3-D finite element analysis. In *IEEE Trans. Instrum. Meas.* 51 (5), pp. 1090–1096. DOI: 10.1109/TIM.2002.806006.

Gramse, G.; Kasper, M.; Fumagalli, L.; Gomila, G.; Hinterdorfer, P.; Kienberger, F. (2014): Calibrated complex impedance and permittivity measurements with scanning microwave microscopy. In *Nanotechnology* 25 (14), p. 145703. DOI: 10.1088/0957-4484/25/14/145703.

Gramse, G.; Kölker, A.; Lim, T.; Stock, T. J. Z.; Solanki, H.; Schofield, S. R. et al. (2017): Nondestructive imaging of atomically thin nanostructures buried in silicon. In *Science advances* 3 (6), e1602586. DOI: 10.1126/sciadv.1602586.

Gregory, A. P.; Blackburn, J. F.; Lees, K.; Clarke, R. N.; Hodgetts, T. E.; Hanham, S. M.; Klein, N. (2016): Measurement of the permittivity and loss of high-loss materials using a Near-Field Scanning Microwave Microscope. In *Ultramicroscopy* 161, pp. 137–145. DOI: 10.1016/j.ultramic.2015.11.015.

H. P. Huber; M. Moertelmaier; T. M. Wallis; C. J. Chiang; M. Hochleitner; A. Imtiaz et al. (2010): Calibrated nanoscale capacitance measurements using a scanning microwave microscope. In *Rev. Sci. Instrum.* 81 (11), p. 113701. DOI: 10.1063/1.3491926.

Haddadi, K.; Haenssler, O. C.; Boyaval, C.; Dambrine, G.; Theron, T. (2017): Near-Field Scanning Millimeter-wave Microscope Combined with a Scanning Electron Microscope. In

IEEE MTT-S (Ed.): 2017 IEEE/MTT-S International Microwave Symposium. Honolulu, HI, USA, 4-9 June: IEEE.

Haddadi, K.; Lasri, T. (2012): Interferometric technique for microwave measurement of high impedances. In : 2012 IEEE/MTT-S International Microwave Symposium - MTT 2012, vol. 2012. Montreal, QC, Canada, pp. 1–3.

Haenssler, O. C. (2014): Integration of a Scanning Microwave Microscope and a Scanning Electron Microscope. Towards a new instrument to imaging, characterizing and manipulating at the nanoscale. In Pasi Kallio (Ed.): Proc. of 2014 Int. Conf. on Manipulation, Manufacturing and Measurement on the Nanoscale (3M-NANO). Taipei, Taiwan, 27.10.-31.10. Piscataway, NJ: IEEE, pp. 39–43.

Haenssler, O. C.; Fatikow, S. (2015): Manipulating and characterizing with nanorobotics. In-situ SEM technique for centimeter and millimeter waves. In : 2015 40th Int. Conf. on Infrared, Millimeter, and Terahertz Waves (IRMMW-THz). Hong Kong, 23.08.-28.08. IEEE. Piscataway, NJ: IEEE, pp. 1–2.

Haenssler, O. C.; Kamenik, J.; Wich, T. (2005): Device for moving the end effector of a measuring or manipulating arrangement and method for determining the contact force or the position of an end effector. Applied for by Carl von Ossietzky Universität Oldenburg on 11/14/2005. Patent no. EP1792693 A3.

Haenssler, O. C.; Kostopoulos, A.; Doundoulakis, G.; Aperathitis, E.; Fatikow, S.; Kiriakidis, G. (2017): Test standard for light, electron and microwave microscopy to enable robotic processes. In Sinan Haliyo (Ed.): MARSS 2017. 2017 Int. Conf. on Manipulation, Automation and Robotics at Small Scales (MARSS). Montreal, QC, Canada. Piscataway, NJ: IEEE, pp. 1–5.

Hang, F.; Lu, D.; Barber, A. H. (2009): Combined AFM-SEM for mechanical testing of fibrous biological materials. In *MRS Proc.* 1187. DOI: 10.1557/PROC-1187-KK06-06.

Happy, H.; Haddadi, K.; Theron, D.; Lasri, T.; Dambrine, G. (2014): Measurement Techniques for RF Nanoelectronic Devices. New Equipment to Overcome the Problems of Impedance and Scale Mismatch. In *IEEE Microwave Magazine* 15 (1), pp. 30–39. DOI: 10.1109/MMM.2013.2288710.

Hoffmann, J.; Wollensack, M.; Zeier, M.; Niegemann, J.; Huber, H.; Kienberger, F. (2012): A calibration algorithm for nearfield scanning microwave microscopes. In : Nanotechnology (IEEE-NANO), 2012 12th IEEE Conference on. Birmingham, UK, pp. 1–4.

Huebner, U.; Morgenroth, W.; Boucher, R.; Meyer, M.; Mirand, W.; Buhr, E. et al. (2007): A nanoscale linewidth/pitch standard for high-resolution optical microscopy and other microscopic techniques. In *Meas. Sci. Technol.* 18 (2), pp. 422–429. DOI: 10.1088/0957-0233/18/2/S14.

Hunton, J. K. (1960): Analysis of Microwave Measurement Techniques by Means of Signal Flow Graphs. In *IEEE Trans. Microwave Theory Techn.* 8 (2), pp. 206–212. DOI: 10.1109/TMTT.1960.1124724.

Ibach, Harald; Lüth, Hans (2003): Solid-State Physics. An Introduction to Principles of Materials Science. Third Extensively Updated and Enlarged Edition. Berlin, Heidelberg: Springer (Advanced Texts in Physics). Available online at <http://dx.doi.org/10.1007/978-3-662-05342-3>.

IMEC: Calibration standards and test samples. Leuven, Belgium. Available online at [www2.imec.be/be\\_en/services-and-solutions/cams/products/calibration-standards-and-test-s](http://www2.imec.be/be_en/services-and-solutions/cams/products/calibration-standards-and-test-s), checked on 03 02 2017.

Imtiaz, A.; Anlage, S. M. (2003): A novel STM-assisted microwave microscope with capacitance and loss imaging capability. In *Ultramicroscopy* 94 (3-4), pp. 209–216. DOI: 10.1016/S0304-3991(02)00291-7.

Imtiaz, A.; Anlage, S. M.; Barry, J. D.; Melngailis, J. (2007): Nanometer-scale material contrast imaging with a near-field microwave microscope. In *Appl. Phys. Lett.* 90 (14), p. 143106. DOI: 10.1063/1.2719164.

Imtiaz, A.; Wallis, T. M.; Kabos, P. (2014a): Near-Field Scanning Microwave Microscopy: An Emerging Research Tool for Nanoscale Metrology. In *IEEE Microwave* 15 (1), pp. 52–64. DOI: 10.1109/MMM.2013.2288711.

Imtiaz, A.; Wallis, T. M.; Lim, S.-H.; Tanbakuchi, H.; Huber, H.-P.; Hornung, A. et al. (2012): Frequency-selective contrast on variably doped p-type silicon with a scanning microwave microscope. In *J. Appl. Phys.* 111 (9), p. 93727. DOI: 10.1063/1.4716026.

Imtiaz, Atif; Wallis, Thomas Mitchell; Kabos, Pavel (2014b): Near-Field Scanning Microwave Microscopy. An Emerging Research Tool for Nanoscale Metrology. In *IEEE Microwave* 15 (1), pp. 52–64. DOI: 10.1109/MMM.2013.2288711.

IRDS (2016a): Whitepaper Beyond CMOS (Emerging Research Devices, ERD). Edited by International Roadmap for Devices and Systems Initiative. IEEE. Available online at [https://irds.ieee.org/images/files/pdf/2016\\_BC.pdf](https://irds.ieee.org/images/files/pdf/2016_BC.pdf), checked on 11/25/2017.

IRDS (2016b): Whitepaper Metrology. Edited by International Roadmap for Devices and Systems Initiative. IEEE. Available online at [https://irds.ieee.org/images/files/pdf/2016\\_MET.pdf](https://irds.ieee.org/images/files/pdf/2016_MET.pdf), checked on 11/25/2017.

IRDS (2016c): Whitepaper More Moore. Edited by International Roadmap for Devices and Systems Initiative. IEEE. Available online at [https://irds.ieee.org/images/files/pdf/2016\\_MM.pdf](https://irds.ieee.org/images/files/pdf/2016_MM.pdf), checked on 11/24/2017.

Joachimsthaler, I.; Heiderhoff, R.; Balk, L. J. (2003): A universal scanning-probe-microscope-based hybrid system. In *Meas. Sci. Technol.* 14 (1), pp. 87–96. DOI: 10.1088/0957-0233/14/1/313.

Joseph, C. H.; Sardi, G. M.; Tuca, S. S.; Gramse, G.; Lucibello, A.; Proietti, E. et al. (2016): Scanning microwave microscopy technique for nanoscale characterization of magnetic materials. In *Journal of Magnetism and Magnetic Materials* 420, pp. 62–69. DOI: 10.1016/j.jmmm.2016.06.053.

Kalinin, S. V.; Gruverman, A. (2007): Scanning probe microscopy. Electrical and electromechanical phenomena at the nanoscale. New York: Springer.

Kalinin, S. V.; Strelcov, E.; Belianinov, A.; Somnath, S.; Vasudevan, R. K.; Lingerfelt, E. J. et al. (2016): Big, Deep, and Smart Data in Scanning Probe Microscopy. In *ACS Nano*. DOI: 10.1021/acsnano.6b04212.

Karbassi, A.; Ruf, D.; Bettermann, A. D.; Paulson, C. A.; van der Weide, Daniel W.; Tanbakuchi, H.; Stancliff, R. (2008): Quantitative scanning near-field microwave microscopy for thin film dielectric constant measurement. In *Rev. Sci. Instrum.* 79 (9), p. 94706. DOI: 10.1063/1.2953095.

Keysight Corp. (2014): Scanning Microwave Microscope - Application Note 5989-8818EN. Edited by Keysight Corp. Available online at <http://www.keysight.com/main/redirector.jsp?action=ref&cname=EDITORIAL&ckey=1450757&lc=ger&cc=DE&nfr=-11143.0.00>, checked on 10/15/2017.

Kim, J.; Lee, K.; Friedman, B.; Cha, D. (2003): Near-field scanning microwave microscope using a dielectric resonator. In *Appl. Phys. Lett.* 83 (5), p. 1032. DOI: 10.1063/1.1597984.

Kleismit, R. A.; Kazimierczuk, M. K.; Kozlowski, G. (2006): Sensitivity and resolution of evanescent microwave microscope. In *IEEE Trans. Microwave Theory Techn.* 54 (2), pp. 639–647. DOI: 10.1109/TMTT.2005.862668.

Kong, J.; Yenilmez, E.; Tomblor, T. W.; Kim, W.; Dai, H.; Laughlin, R. B. et al. (2001): Quantum interference and ballistic transmission in nanotube electron waveguides. In *Physical review letters* 87 (10), p. 106801. DOI: 10.1103/PhysRevLett.87.106801.

Kracke, B.; Damaschke, B. (1996): Ultrahigh vacuum scanning force microscope with fiber-optic deflection sensor. In *Rev. Sci. Instrum.* 67 (8), p. 2957. DOI: 10.1063/1.1147079.

Kreith, J.; Strunz, T.; Fantner, E. J.; Fantner, G. E.; Cordill, M. J. (2017): A versatile atomic force microscope integrated with a scanning electron microscope. In *Rev. Sci. Instrum.* 88 (5), p. 53704. DOI: 10.1063/1.4983317.

Krohs, F.; Haenssler, O. C.; Bartenwerfer, M.; Fatikow, S. (2014): Atomic force microscopy for high resolution sidewall scans. In Pasi Kallio (Ed.): Proc. of 2014 Int. Conf. on Manipulation, Manufacturing and Measurement on the Nanoscale (3M-NANO). Taipei, Taiwan, 27.10.-31.10. Piscataway, NJ: IEEE, pp. 276–279.

Lai, K.; Ji, M. B.; Leindecker, N.; Kelly, M.A.; Shen, Z.X. (2007): Atomic-force-microscope-compatible near-field scanning microwave microscope with separated excitation and sensing probes. In *Rev. Sci. Instrum.* 78 (063702). DOI: 10.1063/1.2746768.

Lai, K.; Kundhikanjana, W.; Kelly, M.; Shen, Z. X. (2008): Modeling and characterization of a cantilever-based near-field scanning microwave impedance microscope. In *Rev. Sci. Instrum.* 79 (6), p. 63703. DOI: 10.1063/1.2949109.

Lai, K.; Kundhikanjana, W.; Peng, H.; Cui, Y.; Kelly, M. A.; Shen, Z. X. (2009): Tapping mode microwave impedance microscopy. In *Rev. Sci. Instrum.* 80 (4), p. 43707. DOI: 10.1063/1.3123406.

Lee, Sheng-Chiang; Vlahacos, C. P.; Feenstra, B. J.; Schwartz, Andrew; Steinhauer, D. E.; Wellstood, F. C.; Anlage, Steven M. (2000): Magnetic permeability imaging of metals with a scanning near-field microwave microscope. In *Appl. Phys. Lett.* 77 (26), pp. 4404–4406. DOI: 10.1063/1.1332978.

Lengyel, B. A. (1949): A Michelson-Type Interferometer for Microwave Measurements. In *Proc. IRE* 37 (11), pp. 1242–1244. DOI: 10.1109/JRPROC.1949.234601.

Lewandowski, A.; LeGolvan, D.; Ginley, R. A.; Wallis, T. M.; Imtiaz, A.; Kabos, P. (2008): Wideband measurement of extreme impedances with a multistate reflectometer. In : 2008 72nd ARFTG Microwave Measurement Symposium. 2008 72nd ARFTG Microwave Measurement Symposium. Portland, OR, USA, 9/12/2008 - 12/12/2008: IEEE, pp. 45–49.

Lewis, A.; Komissar, A.; Ignatov, A.; Fedoroyov, O.; Maayan, E.; Yablon, D. (2014): AFM Integrated with SEM/FIB for Complete 3D Metrology Measurements. In *Microsc Microanal* 20 (S3), pp. 1112–1113. DOI: 10.1017/S1431927614007296.

Liang, W.; Bockrath, M.; Bozovic, D.; Hafner, J. H.; Tinkham, M.; Park, H. (2001): Fabry - Perot interference in a nanotube electron waveguide. In *Nature* 411 (6838), pp. 665–669. DOI: 10.1038/35079517.

Lifshits, M.; Goldenberg, R.; Rivlin, E.; Rudzsky, M.; Adel, M. (2004): Image-Based Wafer Navigation. In *IEEE Trans. Semicond. Manufact.* 17 (3), pp. 432–443. DOI: 10.1109/TSM.2004.831939.

Lim, J.H.; Kwon, D.H.; Rieh, J.-S.; Kim, S.-W.; Hwang, S.W. (2005): RF characterization and modeling of various wire bond transitions. In *IEEE Trans. Adv. Packag.* 28 (4), pp. 772–778. DOI: 10.1109/TADV.2005.853554.

Love, A. E. H. (1924): Some Electrostatic Distributions in two Dimensions. In *Proceedings of the London Mathematical Society* s2-22 (1), pp. 337–369. DOI: 10.1112/plms/s2-22.1.337.

Mahmood, I. A.; Moheimani, S. O. R.; Bhikkaji, B. (2011): A New Scanning Method for Fast Atomic Force Microscopy. In *IEEE Trans. Nanotechnology* 10 (2), pp. 203–216. DOI: 10.1109/TNANO.2009.2036844.

Mahmood, I. A.; Moheimani, S. O. Reza (2009): Fast spiral-scan atomic force microscopy. In *Nanotechnology* 20 (36), p. 365503. DOI: 10.1088/0957-4484/20/36/365503.

Marks, Roger B.; Williams, Dylan F. (1992): A General Waveguide Circuit Theory. In *Journal of research of the National Institute of Standards and Technology* 97 (5), pp. 533–562. DOI: 10.6028/jres.097.024.

Mason, S. (1956): Feedback Theory-Further Properties of Signal Flow Graphs. In *Proc. IRE* 44 (7), pp. 920–926. DOI: 10.1109/JRPROC.1956.275147.

MC2 Technologies: SMM Calibration kit. Sainghin en Mélançois, France. Available online at <http://www.mc2-technologies.com/smm-calibration-kit/>, checked on 2/3/2017.

Michalas, L.; Wang, F.; Brillard, C.; Chevalier, N.; Hartmann, J. M.; Marcelli, R.; Theron, D. (2015): Modeling and de-embedding the interferometric scanning microwave microscopy by means of dopant profile calibration. In *Appl. Phys. Lett.* 107 (22), p. 223102. DOI: 10.1063/1.4936761.

Michel, B.; Mizutani, W.; Schierle, R.; Jarosch, A.; Knop, W.; Benedickter, H. et al. (1992): Scanning surface harmonic microscopy: Scanning probe microscopy based on microwave field-induced harmonic generation. In *Rev. Sci. Instrum.* 63 (9), p. 4080. DOI: 10.1063/1.1143215.

Monti, T.; Tselev, A.; Udoudo, O.; Ivanov, I. N.; Dodds, C.; Kingman, S. W. (2016): High-resolution dielectric characterization of minerals. A step towards understanding the basic interactions between microwaves and rocks. In *Int. J. of Mineral Processing* 151, pp. 8–21. DOI: 10.1016/j.minpro.2016.04.003.

- Oh, Y. J.; Huber, H.-P.; Hochleitner, M.; Duman, M.; Bozna, B.; Kastner, M. et al. (2011): High-frequency electromagnetic dynamics properties of THP1 cells using scanning microwave microscopy. In *Ultramicroscopy* 111 (11), pp. 1625–1629. DOI: 10.1016/j.ultramic.2011.09.005.
- Oladipo, A. O.; Kasper, M.; Lavdas, S.; Gramse, G.; Kienberger, F.; Panoiu, N. C. (2013): Three-dimensional finite-element simulations of a scanning microwave microscope cantilever for imaging at the nanoscale. In *Appl. Phys. Lett.* 103 (21), p. 213106. DOI: 10.1063/1.4832456.
- Oldfield, L. C.; Ide, J. P.; Griffin, E. J. (1985): A Multistate Reflectometer. In *IEEE Trans. Instrum. Meas.* IM-34 (2), pp. 198–201. DOI: 10.1109/TIM.1985.4315301.
- Park, J.; Hyun, S.; Kim, A.; Kim, T.; Char, K. (2005): Observation of biological samples using a scanning microwave microscope. In *Ultramicroscopy* 102 (2), pp. 101–106. DOI: 10.1016/j.ultramic.2004.09.007.
- Plassard, C.; Bourillot, E.; Rossignol, J.; Lacroute, Y.; Lepleux, E.; Pacheco, L.; Lesniewska, E. (2011): Detection of defects buried in metallic samples by scanning microwave microscopy. In *Phys. Rev. B* 83 (12). DOI: 10.1103/PhysRevB.83.121409.
- Pozar, D. M. (2012): Microwave engineering. 4. ed. Hoboken NJ: Wiley.
- Qt Company (2017): What is Qt? Available online at <https://www.qt.io/what-is-qt/>.
- Raicu, V.; Feldman, Y. (Eds.) (2015): Dielectric relaxation in biological sSystems. Physical principles, methods, and applications. Oxford: Oxford Univ. Press.
- Randus, M.; Hoffmann, K. (2008): A simple method for extreme impedances measurement - experimental testing. In : ARFTG 2008. 2008 72nd ARFTG Microwave Measurement Symposium. Portland, OR, USA, 9/12/2008 - 12/12/2008: IEEE, pp. 40–44.

Rozhok, S.; Sun, P.; Piner, R.; Lieberman, M.; Mirkin, C. A. (2004): AFM Study of Water Meniscus Formation between an AFM Tip and NaCl Substrate. In *J. Phys. Chem. B* 108 (23), pp. 7814–7819. DOI: 10.1021/jp0401269.

Ruehli, A. E.; Brennan, P. A. (1975): Capacitance models for integrated circuit metallization wires. In *IEEE J. Solid-State Circuits* 10 (6), pp. 530–536. DOI: 10.1109/JSSC.1975.1050654.

Rutherglen, C.; Burke, P. (2009): Nanoelectromagnetics: circuit and electromagnetic properties of carbon nanotubes. In *Small (Weinheim an der Bergstrasse, Germany)* 5 (8), pp. 884–906. DOI: 10.1002/sml.200800527.

Sader, J. E.; Chon, J. W. M.; Mulvaney, P. (1999): Calibration of rectangular atomic force microscope cantilevers. In *Rev. Sci. Instrum.* 70 (10), pp. 3967–3969. DOI: 10.1063/1.1150021.

Sakurai, T.; Tamaru, K. (1983): Simple formulas for two- and three-dimensional capacitances. In *IEEE Trans. Electron Devices* 30 (2), pp. 183–185. DOI: 10.1109/T-ED.1983.21093.

Sann, K. H. (1968): The Measurement of Near-Carrier Noise in Microwave Amplifiers. In *IEEE Trans. Microwave Theory Techn.* 16 (9), pp. 761–766. DOI: 10.1109/TMTT.1968.1126783.

Sassine, Gilbert; La Barbera, Selina; Najjari, Nabil; Minvielle, Marie; Dubourdieu, Catherine; Alibart, Fabien (2016): Interfacial versus filamentary resistive switching in TiO<sub>2</sub> and HfO<sub>2</sub> devices. In *Journal of Vacuum Science & Technology B, Nanotechnology and Microelectronics: Materials, Processing, Measurement, and Phenomena* 34 (1), p. 12202. DOI: 10.1116/1.4940129.

Schumacher, H. W.; Keyser, U. F.; Zeitler, U.; Haug, R. J.; Eberl, K. (1999): Nanomachining of mesoscopic electronic devices using an atomic force microscope. In *Appl. Phys. Lett.* 75 (8), pp. 1107–1109. DOI: 10.1063/1.124611.

Schweinböck, T.; Hommel, S. (2014): Quantitative Scanning Microwave Microscopy: A calibration flow. In *Microelectronics Reliability* 54 (9-10), pp. 2070–2074. DOI: 10.1016/j.microrel.2014.07.024.

Sematech (2015): International Technology Roadmap for Semiconductors 2.0. Executive report 2015. Semiconductor Industry Association (SIA). Available online at [http://www.semiconductors.org/main/2015\\_international\\_technology\\_roadmap\\_for\\_semiconductors\\_itr/](http://www.semiconductors.org/main/2015_international_technology_roadmap_for_semiconductors_itr/), checked on 20171107.

Shi, C.; Luu, D. K.; Yang, Q.; Liu, J.; Chen, J.; Ru, C. et al. (2016): Recent advances in nanorobotic manipulation inside scanning electron microscopes. In *Microsyst. Nanoeng.* 2, p. 16024. DOI: 10.1038/micronano.2016.24.

SmarAct GmbH (2016): PicoScale User Manual. Oldenburg, Germany.

Smoliner, J.; Huber, H. P.; Hochleitner, M.; Moertelmaier, M.; Kienberger, F. (2010): Scanning microwave microscopy/spectroscopy on metal-oxide-semiconductor systems. In *J. Appl. Phys.* 108 (6), p. 64315. DOI: 10.1063/1.3482065.

SPI Supplies, West Chester, PA, USA: MRS-6 Geller Magnification Reference Standard. Available online at <http://www.2spi.com/item/z02782/geller-mrs-6>, checked on 8/28/2017.

Stahl, U.; Yuan, C. W.; de Lozanne, A. L.; Tortonesi, M. (1994): Atomic force microscope using piezoresistive cantilevers and combined with a scanning electron microscope. In *Appl. Phys. Lett.* 65 (22), p. 2878. DOI: 10.1063/1.113030.

Steinhauer, D. E.; Vlahacos, C. P.; Dutta, S. K.; Wellstood, F. C.; Anlage, Steven M. (1997): Surface resistance imaging with a scanning near-field microwave microscope. In *Appl. Phys. Lett.* 71 (12), p. 1736. DOI: 10.1063/1.120020.

Stowe, T. D.; Yasumura, K.; Kenny, T. W.; Botkin, D.; Wago, K.; Rugar, D. (1997): Attonewton force detection using ultrathin silicon cantilevers. In *Appl. Phys. Lett.* 71 (2), p. 288. DOI: 10.1063/1.119522.

Sutono, A.; Cafaro, N. G.; Laskar, J.; Tentzeris, M. M. (2001): Experimental modeling, repeatability investigation and optimization of microwave bond wire interconnects. In *IEEE Trans. Adv. Packag.* 24 (2), pp. 595–603. DOI: 10.1109/6040.982850.

Synge, E. (1928): A suggested Method for extending Microscopic Resolution into the Ultra-Microscopic Region. In *Phil. Mag.* 6, pp. 356–362.

Tabib-Azar, M.; Wang, Y. (2004): Design and Fabrication of Scanning Near-Field Microwave Probes Compatible With Atomic Force Microscopy to Image Embedded Nanostructures. In *IEEE Trans. Microwave Theory Techn.* 52 (3), pp. 971–979. DOI: 10.1109/TMTT.2004.823596.

Tai, T.; Ghamsari, B. G.; Anlage, S. M. (2013): Nanoscale Electrodynamic Response of Nb Superconductors. In *IEEE Trans. Appl. Supercond.* 23 (3), p. 7100104. DOI: 10.1109/TASC.2012.2227651.

Talanov, V. V.; Scherz, A.; Moreland, R. L.; Schwartz, A. R. (2006): A near-field scanned microwave probe for spatially localized electrical metrology. In *Appl. Phys. Lett.* 88 (13), p. 134106. DOI: 10.1063/1.2189147.

Talanov, V. V.; Schwartz, A. R. (2009): Near-Field Scanning Microwave Microscope for Interline Capacitance Characterization of Nanoelectronics Interconnect. In *IEEE Trans. Microwave Theory Techn.* 57 (5), pp. 1224–1229. DOI: 10.1109/TMTT.2009.2017352.

Théron, Didier: Note on analytical modelling of MEMS resonators to Olaf C. Haenssler. personal communication 14.03.2018.

Torigoe, K.; Arita, M.; Motooka, T. (2012): Sensitivity analysis of scanning microwave microscopy for nano-scale dopant measurements in Si. In *J. Appl. Phys.* 112 (10), p. 104325.

DOI: 10.1063/1.4765730.

Torrezan, Antonio C.; Strachan, John Paul; Medeiros-Ribeiro, Gilberto; Williams, R. Stanley (2011): Sub-nanosecond switching of a tantalum oxide memristor. In *Nanotechnology* 22 (48), p. 485203. DOI: 10.1088/0957-4484/22/48/485203.

Troyon, M.; Lei, H.N.; Wang, Z.; Shang, G. (1997): A Scanning Force Microscope Combined with a Scanning Electron Microscope for Multidimensional Data Analysis. In *Microsc. Microanal. Microstruct.* 8 (6), pp. 393–402. DOI: 10.1051/mmm:1997130.

Tsai, C-L; Warger, W. C.; Laevsky, G. S.; Dimarzio, C. A. (2008): Alignment with sub-pixel accuracy for images of multi-modality microscopes using automatic calibration. In *Journal of microscopy* 232 (1), pp. 164–176. DOI: 10.1111/j.1365-2818.2008.02076.x.

Tselev, A.; Ivanov, I. N.; Lavrik, N. V.; Belianinov, A.; Jesse, S.; Mathews, J. P. et al. (2014): Mapping internal structure of coal by confocal micro-Raman spectroscopy and scanning microwave microscopy. In *Fuel* 126, pp. 32–37. DOI: 10.1016/j.fuel.2014.02.029.

Tselev, A.; Lavrik, N. V.; Kolmakov, A.; Kalinin, S. V. (2013): Scanning Near-Field Microwave Microscopy of VO<sub>2</sub> and Chemical Vapor Deposition Graphene. In *Adv. Funct. Mater.* 23 (20), pp. 2635–2645. DOI: 10.1002/adfm.201203435.

Tselev, A.; Lavrik, N. V.; Vlassiuk, I.; Briggs, D. P.; Rutgers, M.; Proksch, R.; Kalinin, S. V. (2012): Near-field microwave scanning probe imaging of conductivity inhomogeneities in CVD graphene. In *Nanotechnology* 23 (38), p. 385706. DOI: 10.1088/0957-4484/23/38/385706.

Tselev, A.; Velmurugan, J.; Ievlev, A. V.; Kalinin, S. V.; Kolmakov, A. (2016): Seeing through Walls at the Nanoscale: Microwave Microscopy of Enclosed Objects and Processes in Liquids. In *ACS Nano* 10 (3), pp. 3562–3570. DOI: 10.1021/acsnano.5b07919.

van der Meijs, N. P.; Fokkema, J. T. (1984): VLSI circuit reconstruction from mask topology. In *Integration, the VLSI Journal* 2 (2), pp. 85–119. DOI: 10.1016/0167-9260(84)90016-6.

van der Weide, D. W. (1997): Localized picosecond resolution with a near-field microwave/scanning-force microscope. In *Appl. Phys. Lett.* 70 (6), p. 677. DOI: 10.1063/1.118272.

Wallis, T. M.; Imtiaz, A.; Curtin, A. E.; Kabos, P.; Kopanski, J. J.; Huber, H.-P.; Kienberger, F.: Calibration techniques for scanning microwave microscopy. In : 2012 Conference on Precision Electromagnetic Measurements (CPEM 2012). Washington, DC, USA, pp. 528–529.

Wang, F.; Clément, N.; Ducatteau, D.; Troadec, D.; Tanbakuchi, H.; Legrand, B. et al. (2014): Quantitative impedance characterization of sub-10 nm scale capacitors and tunnel junctions with an interferometric scanning microwave microscope. In *Nanotechnology* 25 (40), p. 405703. DOI: 10.1088/0957-4484/25/40/405703.

Wessel, J.; Schmalz, K.; Scheytt, J. C.; Kissinger, D. (2017): A 120-GHz Electrical Interferometer for Contactless Permittivity Measurements With Direct Digital Read-Out. In *IEEE Microw. Wireless Compon. Lett.* 27 (2), pp. 198–200. DOI: 10.1109/LMWC.2017.2649384.

Whalley, E.; Schneider, W. G. (1952): The Lennard-Jones 12:6 Potential and the Viscosity of Gases. In *The Journal of Chemical Physics* 20 (4), p. 657. DOI: 10.1063/1.1700510.

Whitwell, A. L.; Williams, N. (1959): A new microwave technique for determining noise spectra at frequencies close to the carrier. In *Microwave Journal* (2), pp. 27–32.

- Wieghaus, M. F.; Tiemerding, T.; Haenssler, O. C.; Fatikow, S. (2016): Modularized SPM-controller based on an FPGA for combined AFM and SMM measurements. In Sinan Haliyo (Ed.): MARSS 2016, Paris. 2016 Int. Conf. on Manipulation, Automation and Robotics at Small Scales (MARSS). Paris, France. Piscataway, NJ: IEEE, pp. 1–6.
- Williams, P. A.; Papadakis, S. J.; Falvo, M. R.; Patel, A. M.; Sinclair, M.; Seeger, A. et al. (2002): Controlled placement of an individual carbon nanotube onto a microelectromechanical structure. In *Appl. Phys. Lett.* 80 (14), p. 2574. DOI: 10.1063/1.1467701.
- Wu, S.; Yu, J.-J. (2010): Attofarad capacitance measurement corresponding to single-molecular level structural variations of self-assembled monolayers using scanning microwave microscopy. In *Appl. Phys. Lett.* 97 (20), p. 202902. DOI: 10.1063/1.3514625.
- Wu, X.; Petralanda, U.; Zheng, L.; Ren, Y.; Hu, R.; Cheong, S.-W. et al. (2017): Low-energy structural dynamics of ferroelectric domain walls in hexagonal rare-earth manganites. In *Science advances* 3 (5), e1602371. DOI: 10.1126/sciadv.1602371.
- Xing, Y.; Myers, J.; Obi, O.; Sun, N. X.; Zhuang, Y. (2012): Scanning Microwave Microscopy Characterization of Spin-Spray-Deposited Ferrite/Nonmagnetic Films. In *Journal of Elec Materi* 41 (3), pp. 530–534. DOI: 10.1007/s11664-011-1874-8.
- Yang, Y.; Lai, K.; Tang, Q.; Kundhikanjana, W.; Kelly, Mi. A.; Zhang, K. et al. (2012): Batch-fabricated cantilever probes with electrical shielding for nanoscale dielectric and conductivity imaging. In *J. Micromech. Microeng.* 22 (11), p. 115040. DOI: 10.1088/0960-1317/22/11/115040.
- Yong, Y. K.; Moheimani, S. O. R.; Petersen, I. R. (2010): High-speed cycloid-scan atomic force microscopy. In *Nanotechnology* 21 (36), p. 365503. DOI: 10.1088/0957-4484/21/36/365503.

Yuan, C. P.; Trick, T. N. (1982): A simple formula for the estimation of the capacitance of two-dimensional interconnects in VLSI circuits. In *IEEE Electron Device Lett.* 3 (12), pp. 391–393.

DOI: 10.1109/EDL.1982.25610.

Zadrazil, M.; Jiruse, J.; Lencova, B.; Dluhos, J.; Hrncir, T.; Rudolf, M. et al. (2012): The step towards an ultimate multifunctional tool for nanotechnology. In : 2012 Int. Conf. on Manipulation, Manufacturing and Measurement on the Nanoscale (3M-NANO). Xi'an, China, 29.08.-01.09. Piscataway, NJ: IEEE, pp. 175–179.

Zeiss Corp. (2015): MultiSEM 505/506. Edited by Zeiss Corp. Available online at <https://www.zeiss.com/microscopy/int/products/scanning-electron-microscopes/multisem.html>, checked on 11/10/2017.

Zhou, Z.; Melde, K. L. (2008): Development of a Broadband Coplanar Waveguide-to-Microstrip Transition With Vias. In *IEEE Trans. Adv. Packag.* 31 (4), pp. 861–872. DOI: 10.1109/TADVP.2008.924254.

Zimmermann, S. (2017): Dedicated Robotic Handling and Processing at the Submicrometer Scale: Feasibility Studies. Doctoral thesis. University of Oldenburg, Oldenburg. School of Computing Science, Business Administration, Economics, and Law.

Zimmermann, S.; Tiemerding, T.; Haenssler, O. C.; Fatikow, S. (2015): Automated robotic manipulation of individual sub-micro particles using a dual probe setup inside the scanning electron microscope. In : 2015 IEEE Int. Conf. on Robotics and Automation (ICRA 2015). Seattle, USA, 26.05.-30.05. IEEE. Piscataway, NJ: IEEE, pp. 950–955.

Zimmermann, S.; Tiemerding, T.; Li, T.; Wang, W.; Wang, Y.; Fatikow, S. (2013): Automated Mechanical Characterization of 2-D Materials using SEM based Visual Servoing. In *International Journal of Optomechatronics* 7 (4), pp. 283–295. DOI: 10.1080/15599612.2013.879501.

---

Zonnevylle, A. C.; van Tol, R. F. C.; Liv, N.; Narvaez, A. C.; Effting, A. P. J.; Kruit, P.; Hoogenboom, J. P. (2013): Integration of a high-NA light microscope in a scanning electron microscope. In *Journal of microscopy* 252 (1), pp. 58–70. DOI: 10.1111/jmi.12071.

This page left intentionally blank.

## ACRONYMS AND ABBREVIATIONS

2D	Two-dimensional
3D	Three-dimensional
AFM	Atomic Force Microscopy
AMiR	Abteilung Mikrorobotik und Regelungstechnik
CMOS	Complementary Metal Oxide Semiconductor
CSV	Comma-separated values
DUT	Device-under-Test
EBiD	Electron beam-induced deposition
FEM	Finite Element Analysis
FIB	Focused ion beam
FinFET	Fin Field Effect Transistor
FPGA	Field-Programmable Gate Array
HIL	Hardware-in-the-loop
IEMN	Institut d'Électronique de Microélectronique et de Nanotechnologie
IF	Interferometer
IR	Infra-red
IRDS	International Roadmap for Devices and Systems
ITRS	International Technology Roadmap for Semiconductors
LM	Light Microscopy
mmW	Millimeter Wave
OAF	Offis Automation Framework
PCB	Printed Circuit Board

---

RC	Remote-controlled
RF	Radio Frequency
SEM	Scanning Electron Microscopy
SFM	Scanning Force Microscopy
STED	Stimulated Emission Depletion Microscopy
STM	Scanning Tunnel Microscopy
SUT	Sample-under-Test
VCO	Voltage controlled oscillator
VNA	Vector Network Analyzer

## **ACKNOWLEDGEMENTS**

The presented work has been carried out at both, the Division Microrobotics and Control Engineering (AMiR) at the University of Oldenburg, Germany, headed by Prof. Dr.-Ing. Sergej Fatikow, and at the Institut d'Électronique de Microélectronique et de Nanotechnologie (IEMN CNRS UMR 8520), Villeneuve d'Ascq, France, headed by Dr. habil. Lionel Buchaillet and vice-headed by Prof. Dr. Gilles Dambrine.

I would like to express my sincere gratitude to Prof. Fatikow and to Dr. habil. Didier Theron for supervising my thesis. This is thanks, on the one hand, to the excellent laboratory equipment of the department and the institute as well as to the confidence in my work. I highly appreciate the freedom I had, during the time of my doctorate at both research locations.

All of my colleagues at AMiR, I would like to thank for the excellent teamwork. I especially thank Markus Wieghaus for steadily doing the development of the system control.

Moreover, I would also like to thank my colleagues at IEMN NAM6 Group and ExCELSiOR Characterization Center for the valuable collaboration and fruitful discussions. Especially I would like to mention here: Prof. Dr. Gilles Dambrine, Dr. Kamel Haddadi, Dr. Jaouad Marzouk (now with University of Waterloo) and Dr. Sijia Gu (now with Rhode & Schwarz Corp.).

I would like to thank my children, Rachel and Carlotta, for their constant support. Finally and most importantly, I would like to thank my beloved wife Sabine for her moral and non-stop support over the years.

This page left intentionally blank.

# DECLARATION OF ORIGINAL WORK

I, Olaf C. Hänßler, hereby declare to have written this thesis only based on the sources listed and without the help of others. I have not submitted or prepared the submission of this or any other doctoral thesis at the Carl von Ossietzky University Oldenburg, Université de Lille 1 or any other university.

I have honored the German Research Foundation, the Carl von Ossietzky University Oldenburg and the Université de Lille 1 guidelines for safeguarding good scientific practice in the completion of this work.

Hiermit erkläre ich, Olaf C. Hänßler, diese Arbeit ohne fremde Hilfe und nur unter Verwendung der angegebenen Quellen verfaßt zu haben. Ich habe bis dato weder an der Carl von Ossietzky Universität Oldenburg, der Universität Lille 1, noch an einer anderen Universität die Eröffnung eines Promotionsverfahrens beantragt oder anderweitig eine Promotion vorbereitet.

Ich habe die Regeln guter wissenschaftlicher Praxis entsprechend der Richtlinien der Deutschen Forschungsgemeinschaft, der Carl von Ossietzky Universität Oldenburg und der Universität Lille 1 eingehalten.

---

(Olaf Christian Hänßler)